EFFECTS OF INTERCALATION AND DEINTERCALATION IN LAYERED MATERIALS: FROM TOPOLOGICAL INSULATORS TO BATTERY CATHODES

by

Uma Garg

A Dissertation Submitted in

Partial Fulfillment of the

Requirements for the Degree of

Doctor of Philosophy

in Physics

at

University of Wisconsin-Milwaukee

December 2020

.

ABSTRACT

EFFECTS OF INTERCALATION AND DEINTERCALATION IN LAYERED MATERIALS: FROM TOPOLOGICAL INSULATORS TO BATTERY CATHODES

by

Uma Garg

The University of Wisconsin-Milwaukee, 2020
Under the Supervision of Professor Prasenjit Guptasarma

Topological insulators are quantum materials which have insulating bulk and conducting surface. The surface states in these materials is protected by time reversal symmetry and spin-orbit coupling. The fascinating quantum properties of these materials could lead to high speed electronics and quantum computing. To explore the transport properties of these systems, I synthesized single crystals of SnTe and Sb_2Se_3 which are potential topological insulators. SnTe is a topological crystalline insulator in which topological surface states are protected by time reversal symmetry and crystal symmetry, in particular mirror symmetry. My Shubnikov-de Haas (SdH) oscillation study on the (001) surface of SnTe under low temperatures up to 0.35 K and at high magnetic fields up to 18T indicates the presence of cylindrical Fermi surface and topological states on (001) surface of SnTe. My results confirm the theoretical prediction of topological states on {100} surface of SnTe by previous authors. In addition, I also studied the transport properties of antimony selenide (Sb_2Se_3), a band insulator with a 1 eV bandgap under ambient conditions which is metallic above 3 GPa, and superconducting above 10 GPa. Our single crystals are orthorhombic, unlike rhombohedral Bi_2Se_3 and Sb_2Te_3. Following up on our previous collaborative studies of Raman spectroscopy and first-principles density functional theory (DFT), which revealed an

.

electronic topological transition (ETT) with pressure, we performed non-contact conductivity measurements using a tunnel diode oscillator (TDO) circuit under high pressure in a diamond anvil cell. A Fermi Surface (FS) is found to appear at 6.4 GPa indicating a possible insulator to metallic transition. We also find evidence for a Berry phase (β) of value π indicating possible non-trivial topologies.

In addition, I also synthesized high energy density layered sodium-ion cathode materials and studied the effects of intercalation and de-intercalation of sodium ions on crystal structure of pristine material. P2-type $Na_{0.67}Mn_{0.65}Fe_{0.35}O_2$ (NMFO) displays high reversible capacity (185 $mAhg^{-1}$) and undergoes structural transitions between $P6_3/mmc$, $P6_3$ (OP4) and orthorhombic *Cmcm* space groups during charge-discharge cycling between 1.5 and 4.3 V. My study shows that the substitution of Jahn-Teller active Fe with nickel and cobalt suppresses structural transition in P2-type $Na_{0.67}Mn_{0.625}Fe_{0.25}Ni_{0.125}O_2$ (NMFNO) and P2-type $Na_{0.67}Mn_{0.625}Fe_{0.25}Co_{0.125}O_2$ (NMFCO). The discharge capacity and specific energy of NMFNO and NMFCO are higher than that of NMFO up to 100 cycles in the 1.5–4.0 V range, and to at least 200 cycles for 2.0–4.0 V range. I further studied morphology changes of cycled cathodes and performed impedance measurements. I observed the formation of cracks and SEI layer on the surface of the cycled cathodes. The total impedance of NMFNO and NMFCO between 1000 kHz and 0.1 Hz is significantly lower than NMFO after 200 cycles.

.

.

TABLE OF CONTENTS

.

.

LIST OF FIGURES

.

.

.

LIST OF TABLES

LIST OF ABBREVIATIONS

SEM	Scanning electron microscopy
XRD	X-ray diffraction
LK	Lifshits-Kosevich
SdH	Shubnikov-de Haas
MR	Magnetoresistance
E_F	Fermi energy
v_F	Fermi velocity
k_F	Fermi momentum
TDO	Tunnel diode oscillator
SEM	Scanning electron microscopy
SIB	Sodium ion battery
LIB	Lithium ion battery
SEI	Solid electrolyte interface
NMP	N-methyl-2-pyrrolidinone
NMFO	$Na_{0.67}Mn_{0.65}Fe_{0.35}O_2$
NMFNO	$Na_{0.67}Mn_{0.625}Fe_{0.25}Ni_{0.125}O_2$
NMFCO	$Na_{0.67}Mn_{0.625}Fe_{0.25}Co_{0.125}O_2$
EC	Ethylene carbonate
PVDF	Polyvinylidene fluoride
EDS	Energy dispersive X-ray spectroscopy
DEC	Diethylcarbonate

.

DAC	Diamond anvil cell
DMC	Dimethyl carbonate
OCV	Open circuit voltage
NHMFL	National High Magnetic Field Laboratory
PPMS	Physical property measurement system
SOC	Spin orbit coupling
QSH	Quantum Spin Hall
TCI	Topological crystalline insulator
TI	Topological insulator
CPE	Constant phase element
ARPES	Angle resolved photoemission spectroscopy
dHvA	de Haas–van Alphen effect

.

ACKNOWLEDGEMENTS

I would like to thank my advisor Professor Prasenjit Guptasarma for all guidance, motivation, advice, and giving me an opportunity to learn throughout my doctoral studies. He has inspired me to become an independent researcher and helped me realize the power of critical thinking and reasoning. Besides my advisor, my sincere thanks to the members of my dissertation committee: Prof. Daniel Agterberg, Prof. Michael Weinert, Prof. Paul Lyman, and Prof. Carol Hirschmugl for their encouragement, insightful comments, and suggestions in general. Special thanks to Dr. Nathaniel Smith who trained me in performing measurements using Physical Property Measurement system (PPMS), materials growth, and in other materials characterization techniques. I am thankful to William Rexhausen and Christian Parsons for their excellent support and collaborations in my sodium-ion battery projects. I am deeply thankful to Prof. Philip Chang for mentoring me in astrophysics project. I am deeply thankful to everybody I met UWM, all the professors from the Physics Department and graduate students, from whom I have learnt so much.

I am very thankful to the Graduate School at the University of Wisconsin- Milwaukee for supporting me through Graduate Chancellor's, Research Excellence, Litchman Prize for the Best Experimentalist Graduate Student, and Distinguished Dissertation Fellowship awards. I am thankful to the Department of Physics at UWM for providing me with teaching assistantship (TA) to support my PhD program. I am especially thankful to the Lichtman family for providing me with fellowships, and the 2017 Lichtman Prize for the best experimentalist student at UWM Physics.

I am very grateful to Dr. Stan Tozer, Dr. Audrey Grockowiak, and Dr. William Coniglio at National High Magnetic Field Laboratory (NHMFL) for their assistance in the high-pressure

.

experiments performed at NHMFL and their guidance. A special thanks to Dr. Audrey Grockowiak for designing and fabricating diamond anvil cells for the high-pressure work. I would also like to thank Dr. William Coniglio for his assistance in contactless resistivity measurements performed using Tunnel Diode Oscillator. I am very thankful to Dr. Alexey Suslov at NHMFL for his kind assistance and support in the transport measurements performed at NHMFL.

A special thanks to Professor Qu at Mechanical Engineering Department, University of Wisconsin-Milwaukee, for giving me an opportunity to work in his lab. I am also thankful to Dr. Joshua Harris for helping me in starting the sodium ion battery research work in Professor Qu's lab.

Finally, I am very grateful to all my past and present teachers and friends in India for their guidance and support. I am deeply grateful to my parents and siblings who supported and inspired me in completing my dissertation. I dedicate this dissertation to my parents and my siblings.

.

1. Introduction

Consumer demand for bigger, better and faster electronic devices, coupled with increasing needs for energy generation and energy storage, has been growing at unprecedented rates over the past fifty years. “Quantum computers” are next-generation candidates to replace our silicon-based computers, with extended capabilities in parallel computing, encryption technology, and other challenging areas such as in modern data science, “big” data, and weather prediction. However, there remain several challenges in the implementation of quantum computers due to their sensitivity to interaction with the environment. Information and processing in quantum computers envisioned so far employs the concept of qubits. A quantum qubit is a unit of quantum information. In classical silicon-based systems, typical of computers developed over the past six decades or so, information is stored in a bit in the form of a 0 or a 1. Both states cannot exist simultaneously. However, quantum mechanics allows a qubit to be the superposition of the two states at the same time. Mathematically, a qubit can be written as a linear combination of the |0> and |1> states:$|\varphi> = \alpha|1> + \beta|2>$. Various types of qubits have been envisioned and implemented in Quantum Information Systems (QIS), but the ideal one has yet to emerge. The main challenge that needs to be overcome is to construct a qubit that is isolated from the environment, but at the same time couples to the outside world to enable measurement. Any interaction with the environment leads to the collapse of the state function. This phenomenon is called the decoherence. Topological Insulators (TI) are being studied by many groups around the world as potential candidates which might solve the problem of decoherence. As described later in this dissertation, a topological insulator is a crystal that possesses an insulating bulk and topologically protected conducting surface states with a single Dirac cone at the Γ point. Since these materials are topologically

.

protected, they are robust against local sources of decoherence such as exchange of energy with the environment by stimulated emission or absorption, impurities and the local defects present inside the material. Therefore, they are promising materials to construct quantum qubits. In this dissertation, I explore novel properties of selected classes of TI's grown and studied by us.

In addition to the ever-increasing need for high speed electronics, the need for energy storage is also increasing. Development of reliable, high-performance solid-state materials for advanced energy conversion and storage is of technological importance for the US economy as well as for a secure, sustainable energy future for humankind. The design of present-day Li and Li-ion based batteries have relied on previous studies of composition, crystal structure-property characterization, and device performance. However, as a mineral, Li is expensive, difficult to mine, and found only in some parts of the globe. Na-ion cathode materials are potential alternatives to Li-ion materials due to the natural abundance, and low cost of sodium resources. Recent developments in suitable electrolyte and anode materials have revived interests in the use of newer Na-based compositions and structures. In this dissertation, I explore and measure crystal structure and properties of several novel variations of Na-ion cathode based batteries.

The above two classes of layered- and intercalated- layered materials are of much current interest in the experimental Condensed Matter Physics community. The training and knowledge gained from my PhD research has been highly applicable to both classes of materials.

2. MATERIAL MOTIVATIONS

This dissertation explores several families of layered compounds which show fascinating electronic properties when a foreign ion is intercalated between the layers. These properties are interesting from the point of view of not only the quantum physics of the systems, but also their

.

applications. In $Cu_xBi_2Se_3$, the Cu intercalation between Bi_2Se_3 layers induces superconductivity and the topological states are theoretically predicted in this sample. Nb interaction between Bi_2Se_3 layers induces superconductivity. In sodium-ion batteries, the intercalation of transition metals such as Fe, Co, Ni and Mn between MO_2 layers of layered metal oxides improve their capacity. Motivated by this unique property of topological insulators and the immense potential of sodium-ion batteries to satiate our energy storage needs, I synthesized these materials to study their properties during my PhD research in collaboration with other PhD students in Prof. Guptasarma's group: William Rexhausen, Nathaniel Smith and Christian Parsons. This dissertation focuses on the synthesis of tin telluride (SnTe) and antimony selenide (Sb_2Se_3) which are potential topological insulators and the study of their transport properties under high magnetic fields and low temperatures. Sb_2Se_3 is an insulator at ambient pressure but is theoretically predicted to become a topological insulator at high pressure. Sb_2Se_3 undergoes a topological quantum phase transition from a traditional ordinary insulator to a nontrivial topological insulator at a critical pressure $P_c \sim 3$ GPa. I performed angle dependent contactless resistivity measurements under high pressure and atmospheric pressure at high magnetic field and low temperature. By scanning the magnetic field at low temperature and at 6.4 GPa pressure, I observed Shubnikov-de Haas (SdH) oscillations in the tunnel diode frequency. However, oscillations were not observed at atmospheric pressure. My study reveals the possible presence of a cylindrical Fermi surface whose axis is parallel to sample's surface. The Berry phase value of π, as measured from my SdH oscillation analysis indicates the possible presence of Dirac states. SnTe is a topological crystalline insulator that has Dirac surface states on {001} and {111} surfaces which are predicted theoretically. I also studied the angle dependence of frequency of SdH oscillations on (100) surface to study its transport properties. This angle dependence of frequency of SdH oscillations

.

gives me the information about the Fermi surface shape and whether the conduction is from the bulk or from the surface states of the sample.

I also focused on fabricating sodium-ion battery cathodes that have high energy density and long cycle life. In particular, I focused on synthesizing P2-type $Na_{0.67}Mn_{0.625}Fe_{0.25}Ni_{0.125}O_2$ and $Na_{0.67}Mn_{0.625}Fe_{0.25}Co_{0.125}O_2$ which have high energy density as compared to $Na_{0.67}Mn_{0.65}Fe_{0.35}O_2$. $Na_{0.67}Mn_{0.65}Fe_{0.35}O_2$ undergoes structural transitions at high charging voltage and at low discharging voltage due to the possible formation of high-spin Jahn Teller active material at higher voltage. In this dissertation, I explored the effects of substituting some Fe content present in cathode with Ni and Co which become Jahn-Teller inactive at higher voltages. I also studied the electrochemical properties of these Ni and Co substituted cathodes and various causes that lead to discharge capacity degradation. Additional introductory discussions are provided separately in Chapters 3 and 4. Chapter 2 presents a brief introduction to the materials characterization and measurement techniques that I used while synthesizing samples and studying their properties. Chapter 3 presents the study of intercalation of Na-ions in layered battery cathodes materials. It also presents the study of P2-$Na_{0.67}Mn_{0.625}Fe_{0.25}Ni_{0.125}O_2$ and P2-$Na_{0.67}Mn_{0.625}Fe_{0.25}Co_{0.125}O_2$, with a focus on their structural stability during the electrochemical insertion and extraction of sodium ions, and their electrochemical performance. This study evaluates the effect of incorporation of nickel and cobalt into $Na_{0.67}Mn_{0.65}Fe_{0.35}O_2$ to address the material's cyclability issue. It also sheds light on the causes that lead to capacity degradation. Chapter 4 presents the study of transport properties of SnTe and Sb_2Se_3 which are both materials with predicted topological properties. This chapter presents the study of Fermi surfaces of these materials using SdH oscillations to evaluate whether their properties arise from bulk states or from surface states. Chapter 5 presents some suggested challenges to address for future work.

.

Chapter 2. Materials Characterization and Measurement Techniques

2.1 Overview

Crystal quality - whether in single crystals, polycrystals, or thin films - affects the properties of materials. The defects and secondary phases formed during the growth of topological crystals and cathode materials affect their transport properties. The defects and vacancies present in topological materials change the Fermi surface energy level and moves it into either conduction or valance bands. For these and other reasons, attention to the growth of high-quality materials is essential to reliable progress in experiments, theory, and applications of basic Condensed Matter Physics.

The understanding of the structure of electrode materials is required to develop efficient batteries. In the research presented in this dissertation, a potential family of materials for the positive electrode in Na-ion batteries were investigated. The research focuses on the structural evolution of the materials induced by insertion and extraction of sodium ions during discharge/charge and the causes that lead to capacity degradation. XRD was used for this purpose. The crystal structures of topological and cathode materials were analyzed by X-ray diffraction and Rietveld analysis. The phase transitions in cathodes induced by the insertion and extraction of sodium ions during galvanostatic discharge and charge cycling were studied by *ex-situ* XRD analysis using a home-built XRD sample holder designed to protect the sample from exposure to air at all times. Scanning electron microscopy (SEM) provided information about the morphology of cathodes before and after cycling. Stoichiometric ratios of elements in the topological and battery were determined using Energy Dispersive X-Ray technique (EDX). The electrochemical performance of materials as positive electrodes vs. sodium metal was examined using

.

galvanostatic cycling. This chapter presents a brief basic introduction to each experimental method and characterization technique employed in this research.

2.2 X-Ray Diffraction

X-Ray diffraction (XRD) is a powerful technique for characterizing crystalline materials. It provides an information on structures, phases, preferred crystal orientations, and other structural parameters, such as average grain size, strain, crystallinity, and crystal defects of materials. Atomic separations in crystals are of order of few Angstroms and, therefore, for diffraction to take place, the incident wave should have wavelength of a few Angstroms. The wavelength of X-rays is also of a few Angstroms and, therefore, crystals with three-dimensional (3D) periodic structures will act as 3D gratings. Thus, X-rays can be used for the study of spatial distribution of atoms in the crystal or for determining the structure of crystals.

X-ray diffraction by crystals are described and formulated by two approaches in direct space: the Laue equations and Bragg's law. The Laue approach provides a rigorous mathematical description of diffraction. In Laue's approach, the X-ray scattering from individual atoms is considered. The diffracted X-rays then recombine to obtain diffraction pattern. On the other hand, in Bragg's approach, parallel crystal planes are considered as mirror planes which reflect X-rays with the angle of reflection equal to the angle of incidence. Figure 2-1 shows the schematic representation of Bragg X-ray diffraction. When two monochromatic parallel X-ray beams with wavelength λ are incident on two subsequent crystallographic planes with interspacing d and Miller indices (hkl), the reflected beams interfere constructively if the path difference is equal to integer multiples of the wavelength. This relation is known as Bragg's law [1]:

$$2d\sin\theta = n\,\lambda$$

where θ is the angle of incidence and n is an integer, known as the order of diffraction.

The θ angle at which Bragg's law is satisfied is called the Bragg angle, θ_B. When the incident angle satisfies the Bragg's law for a particular crystal plane spacing and the X-ray beam wavelength, the X-rays interfere constructively, and a signal is recorded. In a fine powder specimen, crystallites are randomly oriented in every possible direction. Therefore, when a polycrystalline sample is irradiated by a monochromatic X-ray beam, for each set of crystallographic planes, some crystallites are oriented so that Bragg's law is satisfied, and diffraction occurs. X-ray diffraction peaks are produced by constructive interference of a

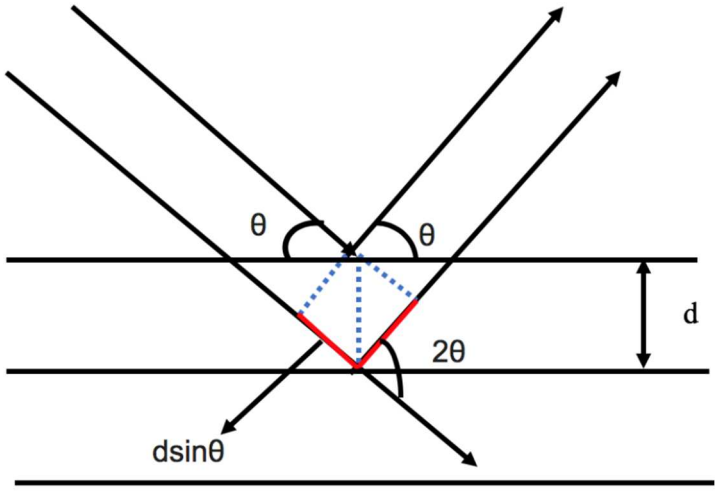

Figure 2-1: Schematic diagram of Bragg X-ray Diffraction

monochromatic beam of X-rays scattered at specific angles from each set lattice planes in a sample. The peak intensities are determined by the atomic positions within the lattice planes. Consequently, the X-ray diffraction pattern is the fingerprint of periodic atomic arrangements in a given material. An online search of a standard database for X-ray powder diffraction patterns enables quick phase identification for a large variety of crystalline samples. X-Ray measurements presented in this

.

thesis were performed using D8 Bruker diffractometer which employs Cu-Kα radiation and is fitted with a high-sensitivity Lynxeye detector.

2.3 Scanning Electron Microscopy

Scanning electron microscopy (SEM) is a technique in which a focused beam of electrons which interacts with sample and produces scattered and secondary electrons, and other emissions which contain information about sample's topography and composition. Electrons are emitted from an electric gun fitted with a tungsten filament cathode. These electrons are focused into a beam by a set of lenses and apertures. The incident electron beam is scanned in a raster scan pattern across the sample, and the position of the beam is combined with the intensity of the detected signal to produce an image. Samples are scanned in high vacuum in this technique. The incident beam of electrons interacts with the sample's surface and leads to many forms of emission from the surface. The types of signals produced by an SEM include secondary electrons (SE), reflected or back-scattered electrons (BSE) and characteristic X-Rays.

Secondary electrons are emitted near the surface of sample when they get excited and have sufficient energy to overcome threshold potential. Secondary electron imaging has greater surface resolution. Some incident electrons may be scattered by atomic nuclei resulting in a change in their direction with a slight reduction of energy (< 1 eV). The electrons deflected back from the sample specimen are called backscattered electrons (BSE). Some electrons that result in the production of characteristic X-rays are produced by inelastic collisions of the incident electrons with electrons in orbitals of atoms in the sample. As the excited electrons return to lower energy states, X-rays of a fixed wavelength, related to the difference in energy levels of electrons in different electron shells for a given element, are emitted. Hence, these X-Rays contain characteristic information about the

.

composition of a specimen. A careful calibrated analysis of such energy dispersive X-rays can provide information about the stoichiometric ratios of elements.

The SEM images presented in this thesis were recorded using a JOEL JSM-6460 LV scanning electron microscope at 15 kV accelerating voltage, currently available at the Advanced Analysis Facility at UWM. The stoichiometric ratios of elements in the samples were confirmed by energy dispersive X-ray spectroscopy (EDS).

2.4 Tunnel Diode Oscillator

Four probe resistivity measurements were difficult to perform on Sb_3Se_3 single crystals, as the resistance of Sb_3Se_3 at ambient pressure is of the order of 10^{11} Ω, and the size of crystals is also small. Therefore, contactless resistivity measurements were performed inside a diamond anvil cell (DAC). A detailed description of this technique is presented below.

2.4.1 Tunnel Diode

A Tunnel diode works on the principle of quantum tunneling effect and is typically used for high frequency switching applications. The p-n junction in these diodes is heavily doped, due to which the depletion layer in these diodes is thin [2]. The tunneling probability increases with the decrease in barrier energy. According to the classical laws of physics, a charged particle should possess energy at least equal to the barrier energy in order to cross it. But quantum mechanically, there exists a non-zero probability that the particle with energy less than the barrier energy will cross the barrier. This is due to the Quantum Tunneling effect. The tunneling probability, *P*, is given as:

$$P \propto e^{-AW\sqrt{E_b}}, \qquad (2.1)$$

where W is the barrier width and E_b is the barrier energy.

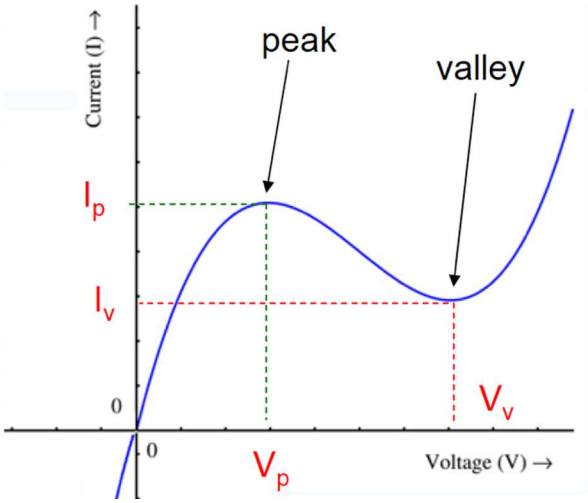

Figure 2-2: I-V characteristics of a tunnel diode

In Figure 2-2, I-V characteristics of a tunnel diode are shown. Initially, a small forward bias voltage is applied. Potential barrier across the p-n junction is still very high and the forward bias current is not noticeable. However, there exists a finite proability that electrons will tunnel from n to p region. This will lead to tunneling current. Due to this, the current increases to peak current, I_p. As the forward bias voltage continues to increase, the electrons in the n region will decrease, resulting in a decrease of tunneling current. This will drive the tunnel diode in the negative resistance region. This means that when the forward bias voltage increases, the current through the p-n junction decreases. As more forward bias voltage is applied, the tunneling current drops to zero. This negative voltage region exists till a certain valley point. At this valley point voltage V_v, the forward bias current starts increasing due to the decrease in potential barrier. As the forward bias voltage increases further, the tunnel diode exhibits I-V characteristics similar to that of a standard p-n diode.

2.4.2 Working Principle of a Tunnel Diode Oscillator

A Tunnel diode oscillator makes use of a tunnel diode for producing oscillations [3]. Figure 2-3a

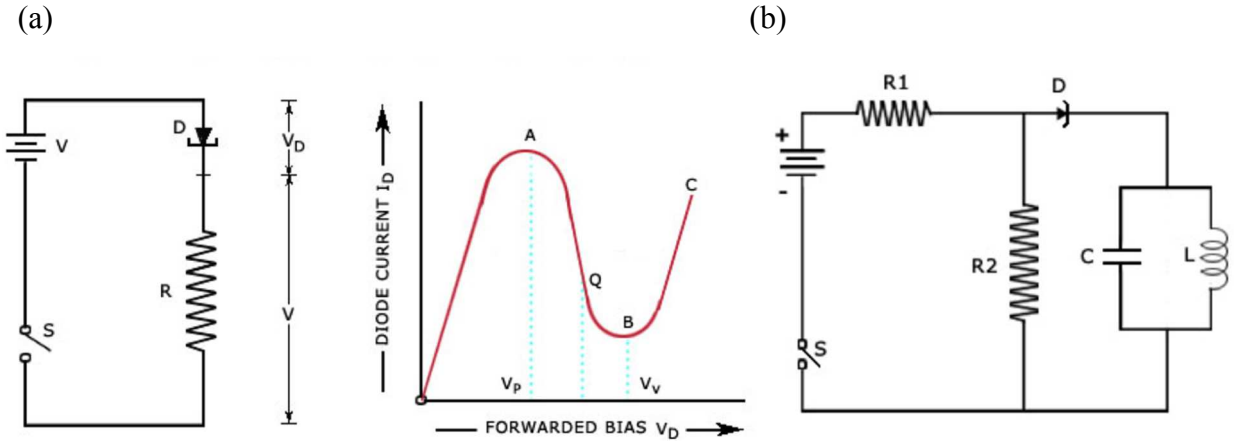

Figure 2-3. (a) Schematic diagram of a TDO circuit (b) Schematic diagram of a TDO circuit with LC tank

shows the schematic diagram of a TDO circuit. The resistance R and the diode resistance D are in series. According to their resistance ratios, the applied voltage V divides between D and R. As the diode voltage, V_D, become greater than V_P (peak voltage) at the point A, the tunnel diode is driven into the negative resistance region and its resistance starts increasing until it becomes equal to the valley voltage V_V at the point B. At this point further increase the forward bias voltage, V_D, drives the diode into the positive resistance region BC. In the region BC, V_R increases, and V_D decreases as the forward bias current increases. This drives the diode back into the negative resistance region. This reduction in V_D causes an increase in circuit current till point A is reached when V_D equals V_P. Thus, the TDO circuit will continue to oscillate back and forth through the negative resistance region between points A and B on the tunnel diode I-V characteristic.

.

2.4.3 General Tunnel Diode Oscillator Setup

Figure 2-3b shows a schematic diagram of a practical TDO circuit. A TDO consists of an LC tank circuit powered by a tunnel diode. A TDR operates by detecting shifts in the resonance frequency of an LC tank circuit driven by the tunnel-diode. When a tunnel diode is properly biased at a voltage in the region of negative differential resistance, a radio frequency current with a constant amplitude continuously flows in the circuit. The sample is placed at the center of the inductor coil. The resonance frequency, *f*, of the tunnel diode oscillator, typically in megahertz range, is given by [4], [5]:

$$f = \frac{1}{\sqrt{LC}} \qquad (2.2)$$

where *L* is the inductance of the coil surrounding the sample and *C* is the capacitance of the tank circuit. The TDO frequency is sensitive to the resistivity of the sample. The oscillations in the resistivity of the sample result in oscillation of the TDO frequency and leads to the measurement of SdH oscillations. The inductance of the coil is proportional to the cross-sectional area occupied by the flux, i.e., the space between the coil and the sample surface plus the skin depth, δ, through which the flux penetrates inside the sample. Change in the skin depth of the sample results in a change in the inductance of the coil, given as [5]:

$$\frac{\Delta L}{L} = \frac{(\Delta\delta) * (2\pi r_s)}{A} \qquad (2.3)$$

Here *A* is the area of the inductance coil, r_s is the radius of the sample rod, and δ is the skin depth. δ is related to the resistivity of the sample as $\delta = \sqrt{\rho/\pi\mu_o f}$, where ρ is the resistivity of sample, and μ_o is the magnetic permeability of free space [5]. The change in frequency of TDO due to the change in inductance is given as [6]:

$$\frac{\Delta f}{f} = \frac{-\Delta L}{2L} \qquad (2.4)$$

.

Hence, a variation in skin depth will lead to change of inductance and the frequency of TDO.

2.5 Measurements under Pressure

Contactless resistivity measurements on Sb_2Se_3 were performed under pressure inside a diamond anvil cell.

2.5.1 Diamond Anvil Cell

High pressure measurements on Sb_2Se_3 were performed using a diamond anvil cell (DAC). A DAC consists of two opposing diamonds with a sample compressed between the tips. The

(a) (b)

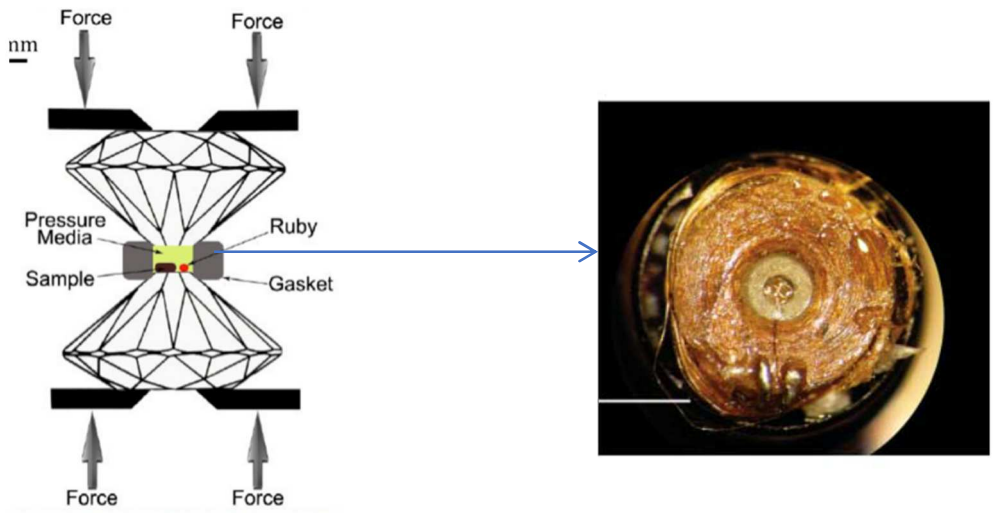

Figure 2-4. (a) Schematic diagram of the diamond anvil cell (DAC). Adapted from reference [7] (b) Expanded view of the metal gasket

sample can be seen through the diamonds and can be illuminated with X-rays and large parts of the visible spectrum. The uniaxial pressure supplied by the diamond tips can be transformed into uniform hydrostatic pressure using a pressure-transmitting medium. A gasket and the two diamond

.

anvils enclose the pressure-transmitting medium. Figure 2-4a shows a schematic diagram of DAC and Figure 2-4b shows the expanded view of the gasket.

A sample of typical dimensions 100 μm x 100 μm x 30 μm was cleaved and loaded inside the DAC made of plastic turnbuckle. The diameter of the diamond anvil was 600 μm. The pressure-transmitting medium used was a mixture of methanol and ethanol with ratio 4:1. Cu gasket with thickness 60 μm was used to contain the medium, and the center hole of 200 μm diameter was drilled. An inductance coil made of insulated copper wire surrounded the sample.

2.5.2 Measurement of pressure inside Diamond Anvil Cell

Pressure inside the cell was measured by calibrating against a ruby fluorescence line shift with pressure. Ruby (Cr^{3+} doped Al_2O_3) spheres placed at the top of sample served as a pressure marker. Cr^{3+} ions in the ruby crystal were excited using green laser light. As these excited Cr^{3+} ions de-excite, they emit light as individual photons. The fluorescence spectrum emitted is composed by the R_1 and R_2 lines (R lines). R_1 and R_2 lines occur at about 694.25 nm and 692.7 nm, respectively, at room pressure. These R_1 and R_2 lines shift towards longer wavelengths as pressure increases. The shifts are fitted to the calibration equation $P = \left(\frac{A}{B}\right)\left[\left(\frac{\lambda}{\lambda_0}\right)^B - 1\right]$ (GPa), with A =1876 ± 6.7, B =10.71 ± 0.14, and λ is the peak wavelength of the ruby R_1 line [8].

2.6 Resistivity Measurements

Resistivity measurements were performed using four-probe techniques. This technique is very useful in measuring resistivity of a sample as compared to two probe method. In this method, four contacts are made on the sample in a row. The current is applied from the outer two probes 1 and 4 as shown in Figure 2-5a. The voltage is measured from the inner two probes 2 and 3.

.

Separation of current and voltage probes eliminates contact resistance and wire resistance from the resistivity

(a) (b)

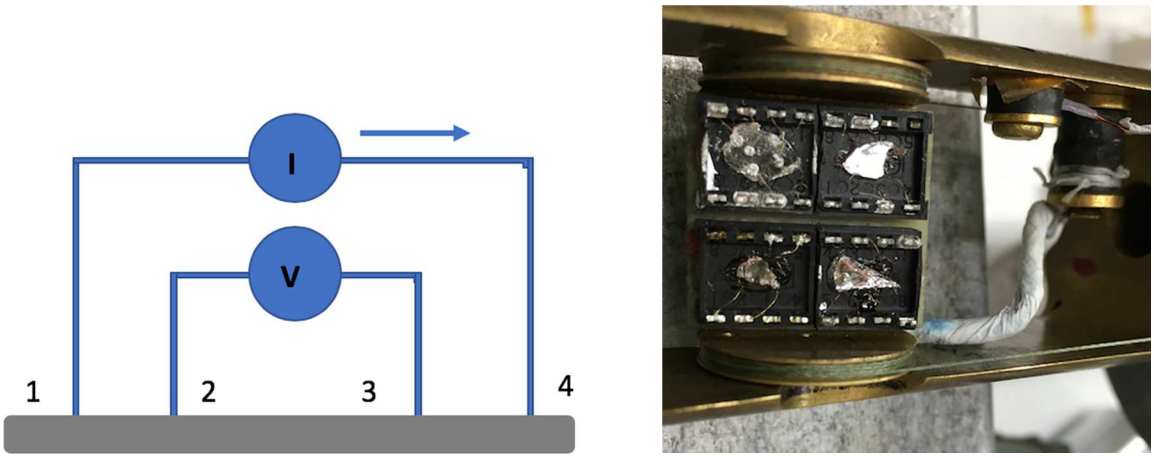

Figure 2-5: (a) Schematic representation of four-probe resistivity measurement (b) Samples mounted on 8 pin dip sockets.

measurements. Electrical contacts were made on samples using 20 μm gold wire and gold wires connected to the sample's surface using silver paint. Samples were mounted on 8 pin dip sockets as shown in Figure 2-5b and were adhered on the socket using VGE 7031 varnish. A small amount of current, typically of the order of 1 mA, was sent so as to minimize sample heating at cryogenic temperatures and maintain a uniform temperature between the sample and the cryostat.

2.7 Electrochemical Measurements

Galvanostatic charge and discharge experiments are standard procedures of evaluation of the electrochemical performance of batteries. Over a galvanostatic cycling experiment, a constant current is applied to the cell, and the cell voltage is measured as a function of time. The applied

current is reversed when a cut-off voltage is reached. Specific capacity, specific energy, rate capability, and cycling stability of the electrochemical cell can be determined by this analysis.

Electrochemical performance of the cathodes was studied using CR2032 coin cell assembly with a half-cell configuration. Na-metal discs (99.8% Sigma Aldrich) were used as counter electrodes; a Celgard separator (Celgard 2325) was used to prevent contact between electrodes. Coin cells were assembled in an ultra-high purity argon-filled glovebox with water and oxygen content lower than 1 ppm. Figure 2-6 shows the schematic representation of the coin cell assembly. The positive and the negative electrode is separated by the Celgard separator. A spring was used for the fabrication of coin cells in order to ensure good contact between different components of the cell. Spacers of 0.5 mm thickness are used to provide mechanical support to the electrodes. Cathode slurries were prepared with an 8:1:1 weight ratio of the active material (NMFO or NMFNO), carbon black (C65 carbon black), and PVDF (polyvinylidene fluoride) in N-methyl-pyrrolidone (NMP, 99.5% Sigma Aldrich) solution. Carbon black is added to increase the electronic conductivity and the binder PVDF is added to bind the particles in the electrode together. Cathodes with loading mass of 4–5 mg cm^{-2} were fabricated by coating the prepared slurry on aluminum foil; the foil was used as a collector for current in the coin cell. The cathodes were subsequently dried at 60°C in a vacuum oven. A 1 M electrolyte solution was prepared with sodium perchlorate ($NaClO_4$, 99.8% Sigma Aldrich) dissolved in 1:1 mixture by volume of EC (Ethylene carbonate) and DEC (Diethylcarbonate) solution.

2.8 Impedance Measurements

Electrochemical Impedance Spectroscopy (EIS) technique is used to measure the impedance of cells. A sinusoidal signal of current or voltage is generated and applied to the battery to obtain

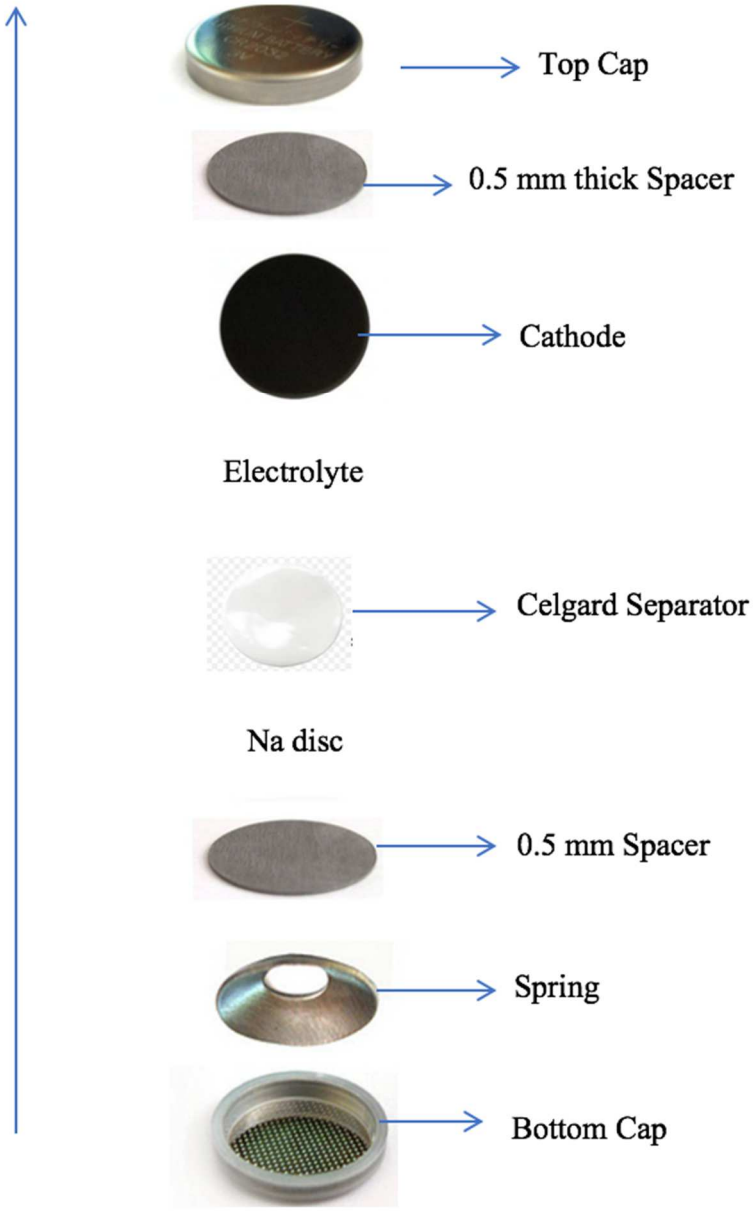

Figure 2-6. Sequence of coin cell fabrication

.

impedance of battery in response. The input signal can be either voltage (potentiostatic mode) or current (galvanostatic mode). In the potentiostatic mode, the impedance of a systems is determined by applying fixed potential to the battery and measuring the resulting current. Nyquist plots are convenient and popular in graphical depictions of EIS measurements. A Nyquist plot is the plot of the real part of impedance on the X-axis and the imaginary part on the Y-axis of a graph. Each point on the Nyquist plot corresponds to the impedance at one frequency. Impedance of a battery is affected by its state of charge, temperature, cycle life, and current. The five kinds of resistances that are present when cells are cycled are:

- **Ohmic Resistance, R_0** - R_0 is the sum of all pure ohmic resistances in the battery and measurement device.
- **Electrical double-layer capacitance, C_{dl}** - Electrical double-layer capacitance describes the capacitive behavior of electrical double layer that is formed as ions from the electrolyte adsorb on the surface of the electrode.
- **Charge-transfer resistance, R_{ct}** – It is used to model the charge-transfer process that happens at each electrode during intercalation.
- **Inductance, L** - It represents the inductive impedance behavior observed at high frequency in the battery. The inductance is due to the porosity of the electrodes and the fact that cell types are formed into compact cylinders.
- **Diffusion & Warburg Element, Z_w** – It models the diffusion process happening inside the battery. It has a constant phase element for which the phase angle is 45° and is independent of frequency. The magnitude of the Warburg impedance is inversely proportional to the square root of the frequency.

.

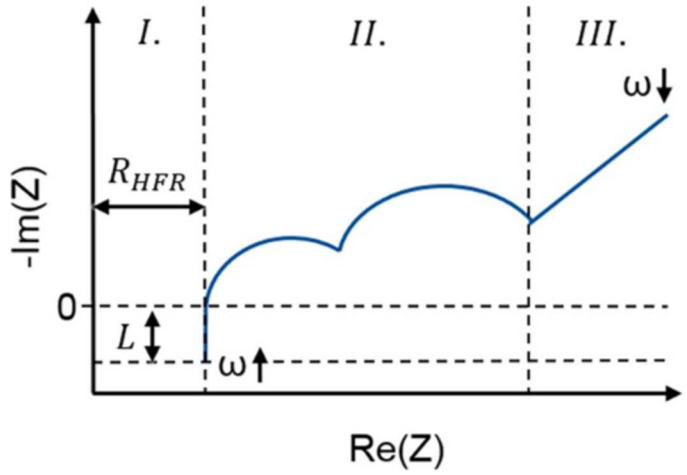

Figure 2-7. Nyquist plot of the EIS of a cycled SIB. Adapted from reference [9].

Figure 2-7 shows the Nyquist plot of the EIS of a cycled SIB. The first section represents the sum of ohmic resistances of electrodes, electrolyte, separator and current collectors. The first semicircle of Section 2 is due to the formation of SEI (Solid Electrolyte Interphase) layer on the surface of anode or cathode during cycling. The second semicircle of Section 2, which is the middle frequency semicircle, represents the impedance of the charge transfer reaction and double layer capacity at electrodes. The linear line in the section 3 represents the low-frequency Warburg impedance.

The total impedance of a cell is modelled with the above elements connected in parallel and in series. The ohmic circuit element resistance, R which has only real part and no imaginary part has the impedance of $Z_R = R$. The phase of current of an ideal capacitor is shifted by -90° with respect to applied voltage. The impedance of an ideal capacitor is given as:

$$Z_c = \frac{1}{j\omega C}, \qquad (2.5)$$

.

where C is capacitance and ω is angular frequency of current and voltage. The ideal capacitor in EIS measurements is often replaced by a constant phase element (CPE) because the surface of an electrode is never ideally flat. The impedance of CPE is given as:

$$Z_{CPE} = \frac{1}{Y_{CPE}} = \frac{1}{Q_0 \omega^n} e^{-\frac{\pi}{2}ni}, \qquad (2.6)$$

where Q_0 which is the admittance of an ideal capacitance and n ($0<n<1$) are frequency independent. The exponent, n, is equal to 1 for a perfect capacitor and 0 for an ohmic resistor. The current of inductor is phase shifted by 90° with respect to applied voltage. The impedance of an inductor is given as:

$$Z_L = j\omega L, \qquad (2.7)$$

where L is impedance of an inductor. The Warburg impedance is

$$Z_W = \frac{1}{Y_0\sqrt{j\omega}}, \qquad (2.8)$$

where Y_0 is the admittance of diffusion.

We performed Electrochemical Impedance Spectroscopy (EIS) measurements to assess the State of Health (SOH) of the cells. We performed EIS on uncycled cells and cells after 10 and 200 cycles, using an AutoLab PGSTAT30 potentiostat from Metrohm with Nova 1.7 software. The EIS was performed in the 1000 kHz to 0.1 Hz frequency range with logarithmic frequency steps, and an AC excitation signal of 10 mV.

.

Chapter 3. Intercalation of Na-ions in layered battery cathodes materials

3.1 Introduction

The development of reliable, high-performance solid-state materials for advanced energy conversion and storage is of technological importance for satisfying growing demands of today's society for energy and a secure, sustainable energy future. Fossil fuels, such as coal and crude oil are used primarily to supply energy and generate electricity. However, pollution arising from their combustion causes a harmful impact on the natural environment. Focus has now shifted to generate power using renewable sources of energy such as solar energy, wind energy and hydro energy. These renewable sources of energy are clean and abundant. The creation of energy from such sources depends on environmental conditions. Wind energy is produced when it is windy, and solar energy production is dependent on sunlight. The electricity produced from these renewable resources need to be stored. Therefore, energy storage in the form of chemical potential using batteries is important.

With the increased use of portable electronic devices such as video cameras, mobile phones, and notebook computers, the need for rechargeable batteries with greater capacity or with reduced size and weight for a given capacity has also increased. Lithium ion batteries are mostly used in portable electronic devices due to the high energy density compared to other rechargeable batteries such as nickel-type batteries and lead acid batteries [10]. The energy densities of lithium ion batteries compared with other rechargeable batteries is shown in Figure 3-1. Lithium-ion batteries (LIBs) have been extensively used to power many modern electronic devices and are now expanding to automotive applications.

.

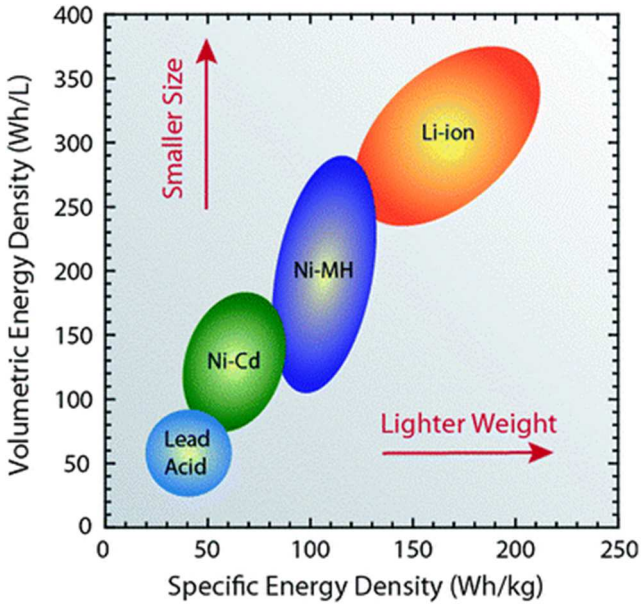

Figure 3-1. Specific energy densities of rechargeable batteries. Adapted from reference [11].

Sodium-ion batteries are potential alternatives to lithium-ion batteries due to the natural abundance, and relatively low cost, of sodium. expanding to automotive applications. Sodium-ion batteries (SIBs) are potential alternatives to lithium-ion batteries for stationary energy storage due to the natural abundance of sodium and the relatively low cost of sodium resources [12]–[15]. The amount of sodium in the earth's crust is over 1000 times higher than that of lithium [16]. Lithium is mostly found from lakes in China, Peru, and parts of the Middle East. Sodium is found in huge amounts in the ocean as well as in the earth crust, whereas the lithium resources are limited. Recent developments in suitable electrolyte and anode materials have revived interest in the use of newer Na-based compounds and structures as potential battery electrode materials. However, the size of Na ion is slightly bigger than Li ion. The larger ionic radius of Na^+ (1.02 Å) vs. Li^+ (0.76 Å) leads to lower capacity, poor cycling stability and slower chemical kinetics. Substantial efforts have been made to apply the successful experience of fabrication of electrodes, especially, that yield

.

higher cyclability and discharge capacity in LIB systems to the SIBs. Development of desirable and efficient electrode materials for SIBs is still an urgent need for their practical application.

Due to the similarity in the operation of LIBs and SIBs, sodium equivalents of many lithium-based electrode materials, such as phosphates, pyrophosphates, and layered oxides are being actively studied as candidates for cathode materials.

3.1.1 Lithium-ion Batteries (LIBs)

A lithium ion battery is typically a rechargeable battery. These are commonly used in portable devices such as laptops, mobiles and tablets. A simple rechargeable lithium battery can be constructed using coin cells in parallel to increase current, or in series to increase voltage. In these batteries, lithium ions move from the anode (negative electrode) through electrolyte to the cathode (positive electrode) during discharge, and back when charging and electrons spontaneously flow in the same direction through an external circuit. The driving force for this process is the difference in the chemical potential of the electrode materials with respect to Li. The space between the two electrodes is filled with electrolyte. Electrolyte is a liquid or a solid medium for transfer of ions between two electrodes during charging or discharging. The electrolyte must have good ionic conductivity and less reactivity with electrodes to achieve desirable discharge capacity and cyclability. Cyclability or cycle life of a cell measures the number of times a battery can be charged and discharged before it begins to break down and no longer can sustain the functions of a device it powers. Discharge capacity is the amount of charge (Amp-hr) available when a cell is discharged at a certain discharge current. A separator is a porous membrane present between the two electrodes which is permeable to Li^+ and prevents a direct contact between

.

positive and negative electrode. Lithium compounds that can be intercalated are typically used as active materials at the cathode and hard carbon or graphite are commonly at the negative electrode.

The first rechargeable Li ion battery was made using TiS_2 as positive electrode active material and Li metal as anode by Whittingham et al. [17] But the battery failed because of Li dendrite formation upon cycling and they could not commercialize it due to safety concerns. Lithium tends to form dendrite on the Li metal surface (anode) after several charging charge cycles. These dendrites may penetrate into the separator and reach the positive electrode leading to a short circuit, overheating of the cell, leading potentially to a fire hazard. Goodenough (Nobel Prize, 2019) first proposed to use layered $LiCoO_2$ as cathode materials in 1981 [18]. $LiCoO_2$/carbon cell was first commercialized by Sony corporation in 1990s [19]. The safety concerns limited the use of $LiCoO_2$ due to dendrite formation. Yazami and Basu reported that graphite could be a good candidate as anode material in which Li ions can intercalate during charging [20], [21]. A carbon electrode that is layered allows intercalation and de-intercalation of Li ions. The synthesis and use of much safer carbonaceous materials such as graphite and hard carbon as the anode active material revolutionized the development of Li-ion batteries and led to their commercialization.

There are several technical terms that are used to describe performance of a battery. They are as follows:

1. Cycle life: Number of cycles a battery can deliver before it becomes inoperative.
2. Self-discharge: Capacity loss that takes place while the battery is in open-circuit condition.
3. State-of-charge (SoC): Indicates charge level of a battery; normally measured in percent.
4. Open circuit voltage (OCV): The voltage between the battery terminals with no load applied.
5. Specific Energy (Wh/kg): The total Watt-hours per unit mass available when the battery is discharged at a certain discharge current.

.

6. Internal Resistance: The resistance to the flow of an electric current within the cell or battery.
7. C-Rate: It is a measure of the rate at which a battery is discharged relative to its maximum capacity. Typically represented as C/10 or C/20, for cycles over 10 or 20 hours.
8. Terminal Voltage (V): The voltage between the battery terminals when load is applied.
9. Discharge Capacity (mAh/g): The total Amp-hours available when the battery is discharged at a certain discharge current.

Figure 3-2 shows the schematic diagram of lithium-ion battery components. Following redox reactions occur on anode and cathode during charging and discharging:

On positive electrode:

$LiCoO_2 \rightarrow Li_{1-x}CoO_2 + xLi^+ + xe-$

On negative electrode:

$C_6 + xLi^+ + xe^- \rightarrow Li_xC_6$

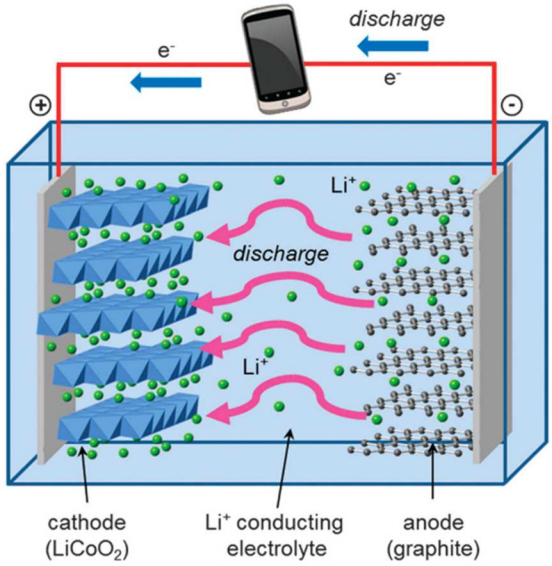

Figure 3-2. Schematic diagram of a Lithium ion battery. Adapted from reference [22].

.

The above reactions are reversible on both electrodes. Theoretical specific capacity, C, of an electrode material which is defined as amount of charge that is stored by battery. It is measured and reported per unit mass of the active material involved in the electrochemical reaction. It can be calculated from the equation: $C = nF/M$ where n is the number of electrons transferred per mole of reaction, F=26.901 $A\square/mol$ is Faraday's constant, and M is the molar mass of the active material. The discharge capacity of $LiCoO_2$ is 175 $mAhg^{-1}$ [18]. The specific energy of a battery is equal to the product of voltage and specific capacity. The volumetric energy density is the energy density per unit volume (Wh/L). As today's electronic devices require more energy within a limited size, volumetric energy density becomes very significant.

The deviation of the actual voltage of from equilibrium voltage is known as polarization. The internal resistance of an electrochemical cell to the flow of ions and electrons deviates the operating voltage of the cell from its equilibrium open circuit voltage. The C-rate or galvanostatic cycling rate specifies the rate at which battery is charged or discharged. In this thesis, 1C rate means that discharge current will discharge entire battery in 1 hour. Similarly, C/20 rate means that entire battery is charged or discharged in 20 hours.

Anode materials offer a higher Li-ion storage capacity than cathodes. Therefore, the cathode material is the limiting factor in the performance of Li-ion batteries. Various cathode materials with layered, spinel, or olivine structures are studied and widely used for Li-ion intercalation.

Aging mechanisms that affect the cyclability and discharge capacity depend on the electrolyte used, active materials in electrodes, electrode design, temperature, charge current, discharge current, and depth of discharge. Crystal structure transitions during charging and discharging may also affect battery's performance. The chemical and crystal-structural stability of

.

an electrolyte is affected by the charging voltage. At higher voltages, electrolyte may decompose which will decrease the cycle life of a cell. The desired characteristics of cathode materials are that it should have robust crystal structure with sufficient sites to intercalate and deintercalate during cycling and have high energy density. Additionally, it should be environment friendly (non-toxic), less reactive with electrolyte, less expensive, light weight, have low self-discharge, have high discharge voltage and have a long cycle life. Similarly, anode material should have low reactivity with electrolyte, non-toxic, and high efficiency of charge and discharge. Considerable research efforts are being made to achieving high specific capacity and good cyclic stability in electrode materials. Active research is underway in the development of an electrolyte that does not decompose at high voltage.

3.1.2 Sodium-ion Batteries (SIBs)

The battery components and energy storage mechanisms of SIBs are essentially very similar to those of LIBs. SIB consists of two electrodes of sodium insertion materials for positive and negative electrodes and they are ionically connected by sandwiching electrolyte which is generally a Na salt dissolved in organic solution. The electrodes are separated by separator to prevent direct contact between them. Figure 3-3 shows the schematic diagram of SIB. In SIBs, due to large size of Na ions compared to Li ions, glass fiber separator is commonly used as the size of pores of this separator is larger than that of Celgard separators. Figure 3-3 shows a schematic illustration of a Na-ion battery. Sodium ions intercalate and de-intercalate in these positive and negative electrodes during charging and discharging.

.

3.1.2.1 Classification of Layered Metal Oxides as Cathode Materials

Layered sodium oxide Na_xMO_2 (M = transition metal) cathode materials are being studied intensively by groups across the world to attain large specific capacity and reversible insertion/extraction. Their crystal structure is similar to that of layered $LiMO_2$ where Li ions intercalate and deintercalate between MO_6 octahedra sheets. Hard carbon (disordered carbon) is extensively studied for the fabrication of negative electrode in SIBs. The most common layered structures are built up by stacking sheets of edge-sharing MO_6 (M = transition metal) octahedra. Layered oxides are characterized mainly in two groups: P2 and O3 type, according to Delma's notation [23]. In P2 type structure, sodium ions are accommodated in prismatic sites whereas in O3-type structures, sodium ions are accommodated at octahedral, as shown in Figure 3-4. The numbers 2 and 3 indicate the number of MO_2 layers in a unit cell. For example, a unit cell of P2-type Na_xMO_2 consists of "two" MO_2 layers and intercalated sodium ion at the prismatic site and O3-type Na_xMO_2 consists of "three" MO_2 layers and intercalated sodium ion at the octahedral site. In the P2 structure, Na occupies two types of prismatic atomic sites, Na_e and Na_f, which share edges or faces with MO_6 octahedra, respectively. From an electrostatic point of view, the Na_e site has been found to be energetically more favorable than the Na_f site [24]. The simultaneous occupancy of both sites allows the in-plane Na^+-Na^+ electrostatic repulsion to be minimized, leading globally to stable configurations [24]. During charging and discharging, the Na ions de-intercalate and intercalate from these prismatic and octahedral sites, respectively. Extraction or insertion of sodium ions from prismatic or octahedral sites of P2 and O3 phases during cycling leads to phase transitions [23].

.

3.1.2.2 Fe and Mn Based Oxides as Cathode Materials

Transition metal oxides-based cathode materials tend to exhibit high discharge capacities

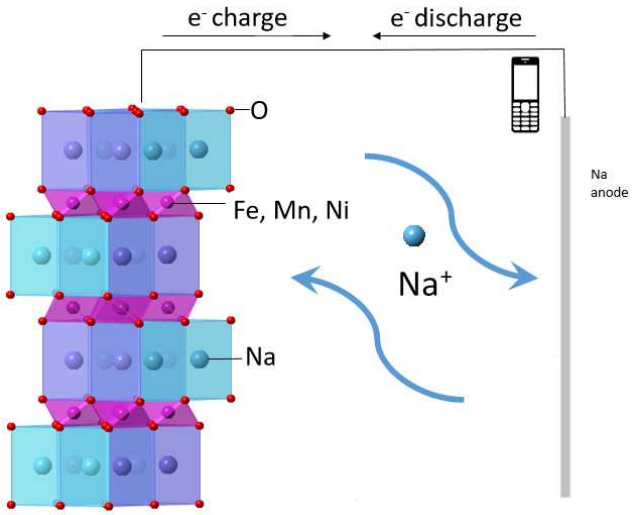

Figure 3-3. Schematic diagram of the configuration of rechargeable Na-ion batteries

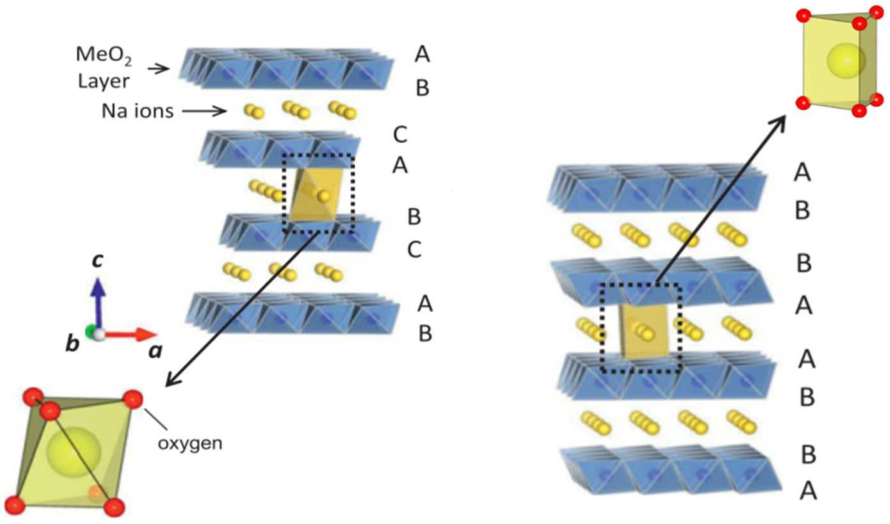

O3 Type **P2 Type**

Figure 3-4. O3 and P2 type layered cathode materials for sodium-ion battery. Adapted from reference [25].

.

due to their compact structural framework. Layered structures of Na_xMnO_2 and Na_xFeO_2 ($x \leq 1$) as cathode materials are being actively explored to fabricate SIB cathodes with high energy density and long cycle life.

Recently, Fe and Mn based cathode materials have gained lot of attention because of their low cost and sustainability. O3-type $NaFeO_2$ is found to be electrochemically active. However, the reversible capacity delivered is nearly equal to 80 $mAhg^{-1}$ when the cutoff voltage is limited to 3.4 V, which is less than half of its theoretical capacity (242 $mAhg^{-1}$) [26]. The cyclability of cathode deteriorates beyond 3.5 V due to the irreversible phase transitions that are observed at high voltages, confirmed by X-ray diffraction [16]. P2-type Na_xFeO_2 is not successfully synthesized yet because of the instability of Fe^{4+} ions in the material under ambient conditions [27]. P2-type $Na_{0.6}MnO_2$ delivers discharge capacity of 150 mAh/g when cycled in a voltage range of 3.8–2.0 V. It retains its pristine crystal structure during the intercalation and deintercalation. However, the stress in lattice caused by intercalation and deintercalation of Na^+ ions leads to the degradation of the crystal quality and to the formation of amorphous material after the first eight cycles [28]. Recent studies by Li et al. show that the presence of Fe in $NaMnO_2$ compounds aids in Na diffusion during charging and leads to high capacity [29]. However, the Jahn Teller distortion of crystal lattice due to the formation of Fe^{4+} leads to structural transitions which are detrimental to cycle life of cells. The substitution of some amount of Fe with Mn, and Ni or Co helps in alleviating the structural transitions driven by Jahn-Teller distortion. Li et al. investigated the effect of substituting Fe with Mn, Ni, and Co in O3-type $Na(Mn_{0.25}Fe_{0.25}Co_{0.25}Ni_{0.25})O_2$. It delivers 180 mAh/g initial discharge capacity and 578 Wh/kg specific energy density with good cycling capability at high cutoff voltage [30].

.

Jahn Teller distortion is a geometric distortion of a molecular system that reduces its symmetry and energy. It is typically observed in octahedral ligand complexes. The distortion leads to elongation or compression of two axial bonds compared to equatorial bonds. The five atomic orbitals are split into two degenerate groups. These two degenerate groups are: t_{2g} (d_{xz}, d_{yz}, d_{xy}) and e_g (d_{z^2} and $d_{x^2-y^2}$) [31]. A molecule distorts to form a lower energy system by removing the

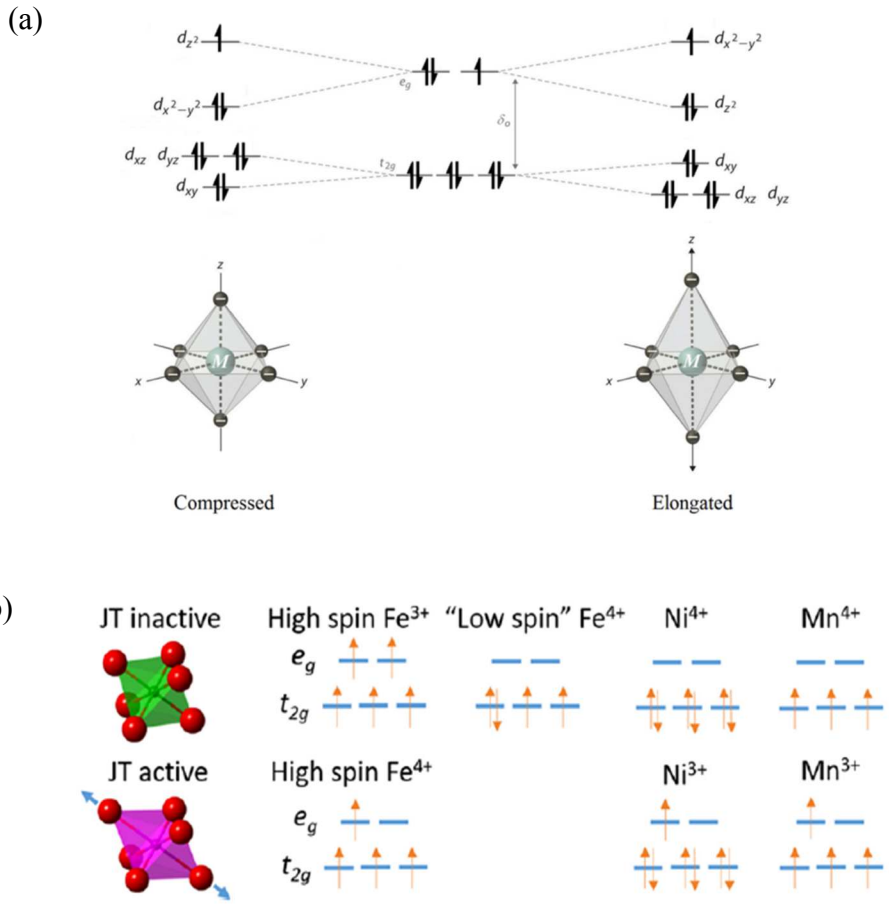

Figure 3-5. (a) Jahn-Teller distortion – Left figure shows that the octahedron is compressed along z direction when the unpaired electron resides in the d_{z^2} orbital. Right figure shows that when an unpaired electron is present in the $d_{x^2-y^2}$ orbital, the octahedra elongates in the z direction. Figure adapted from reference [31]. (b) Electronic configuration of Jahn-Teller active and inactive elements. Figure adapted from reference [29].

.

degeneracy in the ground electronic state. Elongation occurs when the degeneracy is broken by lowering of energy of the d orbitals with a *z* component as shown in Figure 3-5a. In compression, the degeneracy is broken by the stabilization of the d orbitals (lowering their energy) without a z component. Figure 3-5b shows some of the Jahn-Teller active and inactive elements and their electronic configuration.

Yabuuchi et al. partially substituted Fe^{3+} with Mn^{3+} to stabilize the P2 phase and synthesized P2-type $Na_{2/3}Fe_{1/2}Mn_{1/2}O_2$ [27]. They reported that $Na_{2/3}[Fe_{1/2}Mn_{1/2}]O_2$ has initial discharge capacity of 190 $mAhg^{-1}$ when cycled in the voltage range 1.5-4.3 V, with sodium metal used as anode. The energy density is around 520 $mWhg^{-1}$, which is comparable with the energy density of $LiFePO_4$ (530 $mWhg^{-1}$ versus Li) [27]. The initial discharge capacity of P2-$Na_{2/3}[Mn_{1/2}Fe_{1/2}]O_2$ is greater than O3-$Na[Mn_{1/2}Fe_{1/2}]O_2$ [27]. The superior rate capability of P2-$Na_{2/3}[Mn_{1/2}Fe_{1/2}]O_2$ is due to its smooth charge/discharge voltage profile.

There are several factors that lead to capacity degradation, such as electrolyte decomposition, structural transitions in cathodes, etc. Layered Na_xMO_2 materials may undergo phase transitions during cycling due to MO_2 layer glides at low Na contents, and transitions between the different Na^+ ion/vacancy ordered patterns formed at particular Na stoichiometries.

At the end of charging, the Na content in cathode decreases. The deintercalation of Na^+ ions from prismatic sites reduces the screening of $O2^-$ - $O2^-$ repulsions. The increase in repulsion between adjacent MO_2 layers is alleviated by oxygen layer glides perpendicular to the c axis which leads to shrinkage of the interslab distance. These MO_2 layer glides lead to phase transformation from P2 to O2 or OP4 phase. Na^+ vacancies are less stable in prismatic sites than in octahedral sites and structures containing octahedral interslab sites such as O2 or OP4 phase are formed as the Na content decreases when battery is charged to high voltage. The OP4 phase obtained is

composed of an alternate stacking of octahedral (O2) and prismatic (P2) layers along the c-axis. The Na^+ vacancies are located in O-type layers, while the Na^+ ions remain in the P-type layers. The OP4 phase is reported upon Na deintercalation in P2-$Na_xFe_{1/2}Mn_{1/2}O_2$ and P2-$Na_xMn_{1-y}Mg_yO_2$ ($0 < y < 0.2$).

3.2 Crystal Structure Stabilization, Electrochemical Properties, and Morphology of P2-type $Na_{0.67}Mn_{0.625}Fe_{0.25}Ni_{0.125}O_2$

3.2.1 Introduction

Various layered sodium-ion cathode materials Na_xMO_2, where M represents transition metal(s), of P2-type, O3-type, and O2-type have been studied [30], [32], [33]. Of these materials, P2-type $Na_{2/3}[Mn_{1/2}Fe_{1/2}]O_2$ cathode materials are observed to deliver high discharge capacity for limited cycles, while O3-type electrodes have lower capacity but good cyclability. Yabuuchi et al. reported that P2–$Na_{2/3}[Mn_{1/2}Fe_{1/2}]O_2$ delivers a discharge capacity of 190 $mAhg^{-1}$ in the voltage range 1.5–4.3 V [27]. However, they report that $Na_{2/3}[Mn_{1/2}Fe_{1/2}]O_2$ undergoes a structural transition from $P6_3/mmc$ phase to $P6_3$ (OP4) phase when charged to 4.3 V. Pang et al. studied the crystal structure transitions of $Na_{2/3}[Mn_{1/2}Fe_{1/2}]O_2$ during cycling and reported that $Na_{2/3}[Mn_{1/2}Fe_{1/2}]O_2$ undergoes phase transition from $P6_3/mmc$ (P2) phase to $P6_3$ (OP4) phase at 4.3 V charge and to *Cmcm* phase at 1.5 V discharge voltage [34]. Previous authors have identified means by which these structural transitions can be alleviated by analyzing the galvanostatic cycling curves of cycled cells. Yuan et al. and Talaie et al. have studied nickel substituted P2-type $Na_{0.67}Mn_{0.65}Fe_{0.20}Ni_{0.15}O_2$ to suppress these structural transitions during cycling, and report an improvement in discharge capacity [35], [36]. Yuan et al. report that $Na_{0.67}Mn_{0.65}Fe_{0.20}Ni_{0.15}O_2$ has

.

an improved discharged capacity retention upto 30 cycles in the 1.5–4.3 V range in comparison with non-Ni containing NMFO [35], [36]. Additionally, Talaie et al. also report that $Na_{0.67}Mn_{0.65}Fe_{0.20}Ni_{0.15}O_2$ undergoes a structural transition to a *Z* phase when charged to 4.3 V and to *Cmcm* phase when discharged to 1.5 V [35]. However, Yuan et al. report the formation of $P6_3$ (OP4) phase at 4.3V in $Na_{0.67}Mn_{0.65}Fe_{0.20}Ni_{0.15}O_2$ and do not observe structural transition at 1.5V discharge voltage [36].

In this chapter, we clarify these structural issues in $Na_{0.67}Mn_{0.65}Fe_{0.35}O_2$ (NMFO) and $Na_{0.67}Mn_{0.625}Fe_{0.25}Ni_{0.125}O_2$ (NMFNO) cathode materials during cycling using detailed Rietveld crystal structure refinement of X-ray Diffraction (XRD) data at various charge and discharge voltages. We also report detailed analysis of changes in crystal structure of cathode material at different charge and discharge voltages during cycling. Additionally, we also extend the cycling of cathodes to 200 cycles. We also report the morphology and impedance changes that occur in cathodes during cycling.

3.2.2 Synthesis

NMFO and NMFNO were synthesized by a solid-state method. Stoichiometric amounts of Na_2CO_3 (98% Alfa Aesar), Fe_2O_3 (99.99% Alfa Aesar), MnO_2 (99.9% Alfa Aesar), and NiO (99.99% Sigma-Aldrich) were mixed thoroughly for three hours using high energy ball mill. The mixture was pressed into pellets. Pellets were then heated inside furnace at 900°C in air for 12 h, cooled to 600°C at 5°C/ min, and then quenched in air to room temperature from 600°C. Pellets were then stored inside the glovebox having ultra-high purity argon atmosphere.

.

3.2.3 Structural Transitions

Structural transitions of cathode materials limit the cyclability and discharge capacity of cells during cycling. We studied possible crystal structure transitions during sodium intercalation and deintercalation at different charge and discharge voltages. We performed these XRD measurements on cathodes without exposing them to air. CR2032 assembly coin cells were fabricated inside the glove box with ultra-high purity argon gas. Figure 3-6 shows XRD diffractograms of uncycled and cycled NMFO and NMFNO cathodes. The diffractograms were obtained by stopping the cells at different charge and discharge voltages. The cells were cycled 10 times and then were charged or discharged to a particular voltage at the 11^{th} cycle. Our Rietveld analysis confirms that both uncycled NMFO and NMFNO cathodes have P2 type crystal structure and $P6_3/mmc$ space group. In $P6_3/mmc$ space group, first *m* corresponds to mirror plane that is perpendicular to c axis, second *m* corresponds to mirror plane that is parallel to the mirror axis and *c* corresponds to the glide plane along c axis. 6_3 indicates the screw axis. We observe that NMFO undergoes structural transitions when charged to 4.3 V and when discharged to 1.5 V. As shown in Figure 3-6a, our Rietveld analysis shows that NMFO undergoes transition to orthorhombic *Cmcm* phase at 1.5 V during discharge. NMFO transforms to Z phase previously identified by Talaie et al. when charged to 4.3 V or to $P6_3$ (OP4) phase as identified by Yabuuchi et al. and Yuan et al. [27], [35], [36] Previous authors have identified this phase based on the position of a single peak, labelled in Figure 3-6a as "Z/OP4" peak near 2θ equal to 15–17°). We have been unable to fit this particular phase formed at 4.3 V charge. At 4.3 V charge in X/OP4 phase, the shift in peak at 15.4° to 16.7° indicates decrease in distance between MO_2 layers along the c axis. In our XRD studies in NMFO, this Z/OP4 phase has broader and less intense peaks when compared to the diffraction patterns observed in samples at lower cycling voltage. This indicates the

.

degradation of crystal quality at higher charge voltage. However, XRD peaks again sharpen when cell is discharged back to lower voltage from higher voltage, indicating high crystalline quality. Therefore, this effect is reversible. Previous authors identify the phase formed at 1.5 V discharge voltage as a *Cmcm* phase in NMFO. We also observe *Cmcm* phase at 1.5 V discharge voltage in NMFO. We also find that the crystalline quality of this *Cmcm* phase is low as the XRD peaks observed were broad and less in intensity. In summary, NMFO undergoes structural transitions as well as crystalline quality degradation when charged to 4.3 V and discharged to 1.5 V. These structural transitions limit its performance at these voltages. We further discuss that NMFNO cathodes do not undergo structural transitions and are stable in the subsequent paragraphs.

Phase transition during charging at higher voltages in NMFO from a $P6_3/mmc$ (P2) phase to "Z" or "$P6_3$ (OP4)" phase need further discussion. Talaie et al. (2015) rule out the formation of $P6_3$ (OP4) phase, indicated by Yabuuchi et al. (2012), due to Jahn-Teller effect. The Jahn-Teller effect is observed in octahedral complexes containing transition metals such as Mn^{3+}, Fe^{4+}, and Ni^{3+}. This effect results in distortion of the MO_6 octahedra to stabilize the energy of the complex. This Jahn-Teller distortion assists the diffusion of Na ions during cycling and influences cyclability in SIB and LIB batteries [19]. Talaie et al. suggest that the transition at 4.3 V charge is from the pristine $P6_3/mmc$ (P2) to an O2-phase and name it the "Z" phase.

As shown in Figure 3-6, we find that both transitions to the Z/OP4 phase at 4.3 V charge voltage and to the *Cmcm* phase at 1.5 V discharge voltage are absent in Ni-substituted NMFNO. This is in contrast with Talaie et al. and Yuan et al. results [35], [36]. Rietveld analysis of the XRD pattern of NMFNO when charged at 4.3 V shows that it retains the native $P6_3/mmc$ phase. We observe that new peaks appear near the (102), (103), and (104) peaks when NMFNO is discharged to 1.5 V, as shown in Figure 3-6b and 3-6c. These new peaks are labelled by subscript 'a' in Figure

.

3-6c. We find the formation of two $P6_3/mmc$ (P2-type) phases, with slightly different in-plane axis, from the Rietveld analysis. There in-plane axes values are reported in Table 2. This formation of new peaks are also observed below 2.0 V by Talaie et al., but they interpret this as structural transition to a *Cmcm* phase. Therefore, from our XRD measurements and Rietveld analysis, we conclude that structural transitions are not present at 1.5 V discharge or 4.3 V charge voltage in NMFNO. Details of crystal lattice parameters of these two $P6_3/mmc$ (P2) phases formed at 1.5 V discharge voltage in NMFNO are given in Tables 1 and 2.

The substitution of Mn and Fe with Ni in NMFO alleviates structural transitions at 4.3 V charge and 1.5 V discharge and leads to an increase in initial discharge capacity. When the battery is charged to higher voltage, Fe oxidizes to high spin Fe^{4+} for the charge compensation. This formation of Fe^{4+} distorts octahedral complex because of Jahn-Teller effect and helps in deintercalation of Na ions [29]. Mn^{3+}, Fe^{4+}, and Ni^{3+} show the strongest Jahn-Teller effect among the 3d transition metal ions. At the end of charge, Fe is the only 3d transition metal that becomes Jahn-Teller active in Na_xTMO_2, while Mn^{4+} and Ni^{4+} become Jahn Teller inactive. The presence of Fe decreases the Na-ion diffusion barrier at higher charge voltage and increases capacity of cathode. However, the Jahn-Teller effect can cause structural distortions and affect the crystal structural integrity and, thereby, the cyclability of a cell. The substitution of Fe with Ni in NMFNO suppresses Jahn-Teller distortion of crystal lattice at higher voltages. Li et al. report that in O3-$NaTMO_2$ layered cathode materials, Fe becomes high spin Jahn-Teller active at higher charge voltage. The high spin Jahn-Teller active Fe aids in Na-ion diffusion by buckling of Fe-O bonds as well as distorts crystal lattice at higher charge voltages. These two competitive mechanisms can be balanced by substituting some amount of Fe with transition elements which become Jahn-Teller inactive during cycling to synthesize layered oxide cathode materials with high discharge capacity

.

[29]. We obtain results that substituting Fe with Ni in NMFO improves discharge capacity and cyclability, consistent with the result of Li et al. [29].

Tables 1 and 2 show crystal axis parameters of NMFO and NMFNO at different charge and discharge voltages, respectively, obtained after Rietveld refinement of XRD. During charging, the c axis parameter of the NMFO and NMFNO unit cells increases as the interlayer distance between MO_2 layers increases. The increase in c axis with charging is due to the decrease in screening of the repulsion between successive oxygen layers as the sodium ion content decreases from the prismatic sites to their de-intercalation [32], [37]. The in-plane lattice parameters, a and b, of NMFO and NMFNO decrease while charging to higher voltage as the transition metals oxidize during deintercalation of Na ions, causing contraction of M-O bond length in MO_6 octahedra [32].

Figures 3-7 and 3-8 show ex situ XRD measurements performed on uncycled NMFO and NMFNO cathodes and cathodes cycled 200 times. Note that, although we call these measurements ex situ, the XRD was performed in a sealed sample holder, with the sample transferred in a highly controlled glove box maintaining an inert atmosphere. Thus, there was no exposure to air (oxygen) at any time, including during the XRD measurement. We observe that the pristine $P6_3/mmc$ crystal phase does not change after 200 cycles in NMFO and NMFNO. Tables 3 and 4 show lattice parameters of NMFO and NMFNO after 200 cycles obtained from Rietveld analysis. The c-axis decreases for both NMFO and NFMNO after 200 cycles. The lack of crystal structure changes in NMFNO during charging and discharging, when compared with NMFO, indicates that Ni-substitution contributes to the stability of the cathodes during cycling.

.

3.2.4 Results from Electrochemistry

We also investigated the effect of Ni substitution on cycling performance, cycling capacity and specific energy of cells. Figure 3-9 shows the discharge capacity versus number of cycles for NMFO and NMFNO cathodes during constant current cycling. We cycled NMFO and NMFNO cells up to 200 cycles in the voltage ranges 1.5–4.3 V, 1.5–4.0 V, and 2.0–4.0 V. In 1.5-4.3 V range, we allowed the structural transitions to occur in NMFO in order to examine their effect on cyclability. Even though NMFNO does not undergo through structural transitions observed in NMFO at higher voltages, we observe a degradation of crystalline quality at high (4.3 V) and low (1.5 V) voltage in NMFNO. Due to this reason, we also cycled cells in the 2.0–4.0 V range up to 200 cycles wherein we exclude structural transitions. The cells are cycled at C/20 rate (0.047 mA) for the first two formation cycles and at C/10 rate (0.0945 mA) for the remaining cycles in each voltage range. We observe that NMFNO has first-cycle specific energy of 335 Whg^{-1} in caparison with 275 Whg^{-1} for NMFO in the voltage range 1.5–4.3 V. We also find that first cycle specific energy is higher in NMFNO than in NMFO for all three voltage ranges. The discharge capacity of NMFNO remains significantly higher than NMFO up to 200 cycles in the 2.0–4.0 V range. NMFNO starts with a slightly higher discharge capacity than NMFO in the 1.5–4.3 V range. After 30 cycles in 1.5-4.3 V range, the capacity retention of NMFNO is 83% and of NMFO is 81%. We were able to cycle cells only till 30 cycles in the 1.5–4.3 V range, possibly due to breakdown of the electrolyte at higher voltage [38]. The capacity retention of NMFNO is 77% and that of NMFO is 67% at 100^{th} cycle in the cycling window 1.5–4.0 V. The capacity retention of NMFNO is higher than NMFO up to 100 cycles in 1.5-4.0 V range. However, the capacities of both cathodes converge and decrease at the same rate after 100 cycles. The capacity retention of NMFNO is 95% and NMFO is 94% at the 50th cycle in the 2.0–4.0 V range. At the end of 200 cycles, the discharge

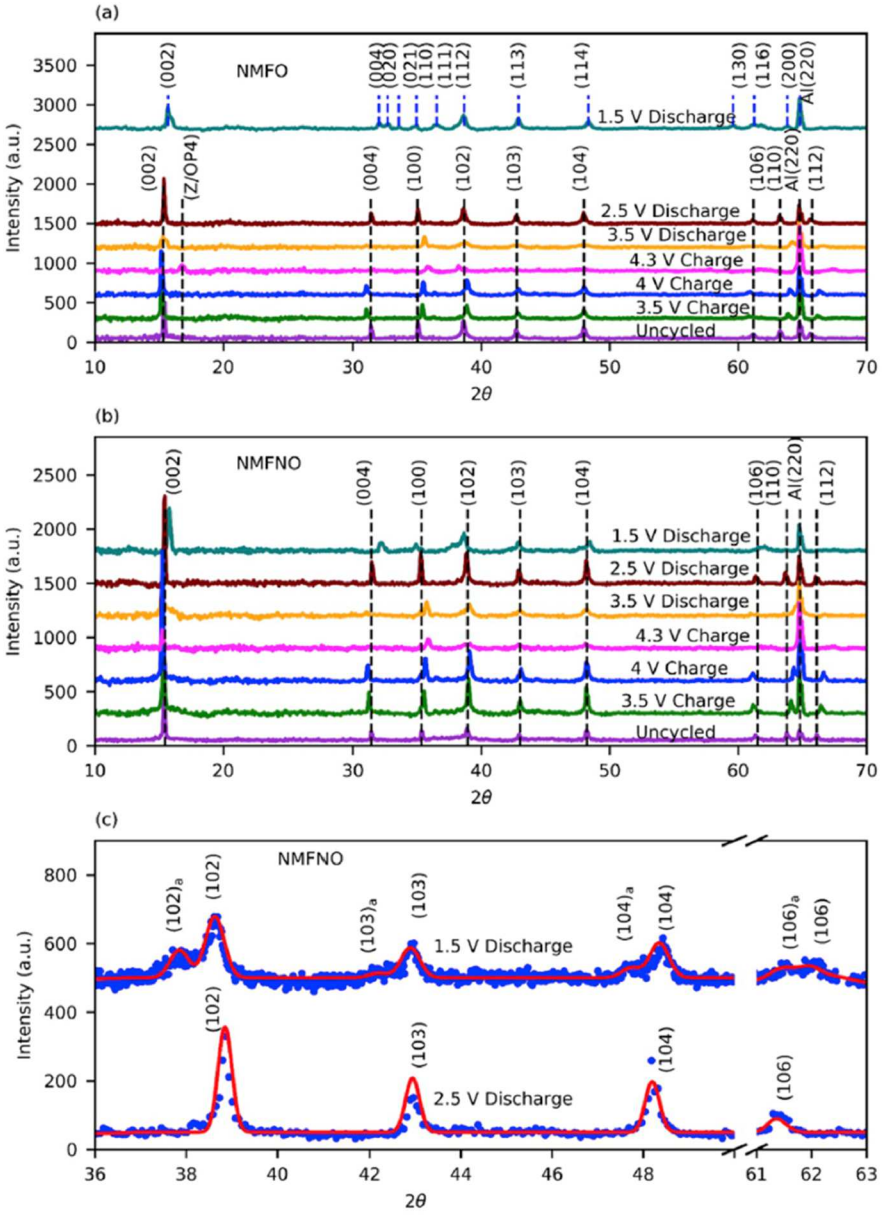

Figure 3-6. XRD of Na-ion cathode materials during charge/discharge of (a) NMFO (also see Table 1) and (b) NMFNO (also see Table 2) during cycling at different voltages in the voltage range 1.5–4.3 V; (c) Rietveld analysis of XRD diffractogram of NMFNO at 1.5 V discharge potential (the blue dots are collected data; the red curve represents Rietveld analysis fitting). The Miller indices written as $(hkl)_a$ indicate the formation of second P2-type, $P6_3/mmc$ phase (also see 1.5 V discharge data in Table 2).

.

Crystal lattice parameters from Rietveld refinement of $Na_{0.67}Mn_{0.65}Fe_{0.35}O_2$ during cycling				
Voltage (V)	**a (Å)**	**b (Å)**	**c (Å)**	**Phase**
Uncycled	2.925	2.925	11.274	*P*6$_3$/*mmc*
3 V Charge	2.911	2.911	11.364	*P*6$_3$/*mmc*
3.5 V Charge	2.895	2.895	11.392	*P*6$_3$/*mmc*
4 V Charge	2.897	2.897	11.413	*P*6$_3$/*mmc*
4.3 V Charge				Z/OP4 (see [35], [36])
3.5 V Discharge	2.895	2.895	11.392	*P*6$_3$/*mmc*
2.5 V Discharge	2.928	2.928	11.272	*P*6$_3$/*mmc*
1.5 V Discharge	2.907	5.492	11.126	*Cmcm*

Table 1. Evolution of lattice parameters of P2-$Na_{0.67}Mn_{0.65}Fe_{0.35}O_2$ (NMFO) at different voltages during cycling in the 1.5-4.3 V range; fitting results from data in Figure 3-6a.

Crystal lattice parameters from Rietveld refinement of $Na_{0.67}Mn_{0.625}Fe_{0.25}Ni_{0.125}O_2$ during cycling			
Voltage (V)	**a = b (Å)**	**c (Å)**	**Phase**
Uncycled	2.904	11.285	*P*6$_3$/*mmc*
3 V Charge	2.894	11.338	*P*6$_3$/*mmc*
3.5 V Charge	2.894	11.333	*P*6$_3$/*mmc*
4 V Charge	2.884	11.386	*P*6$_3$/*mmc*
4.3 V Charge	2.879	11.480	*P*6$_3$/*mmc*
3.5 V Discharge	2.885	11.427	*P*6$_3$/*mmc*
2.5 V Discharge	2.908	11.248	*P*6$_3$/*mmc*
1.5 V Discharge	2.947	11.048	*P*6$_3$/*mmc*
	3.038	11.048	

Table 2. Evolution of lattice parameters of P2-$Na_{0.67}Mn_{0.625}Fe_{0.25}Ni_{0.125}O_2$ (NMFNO) at different voltages during cycling in the 1.5-4.3 V range; fitting results from data in Figure 3-6b.

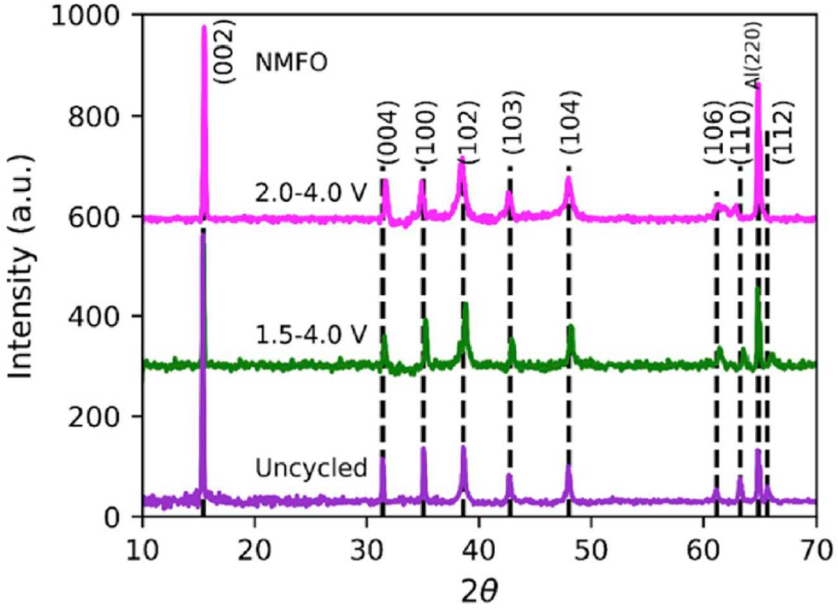

Figure 3-7. XRD diffractograms of uncycled NMFO and NMFO after 200 cycles in the 1.5–4.0 V and 2.0–4.0 V ranges (see Table 3).

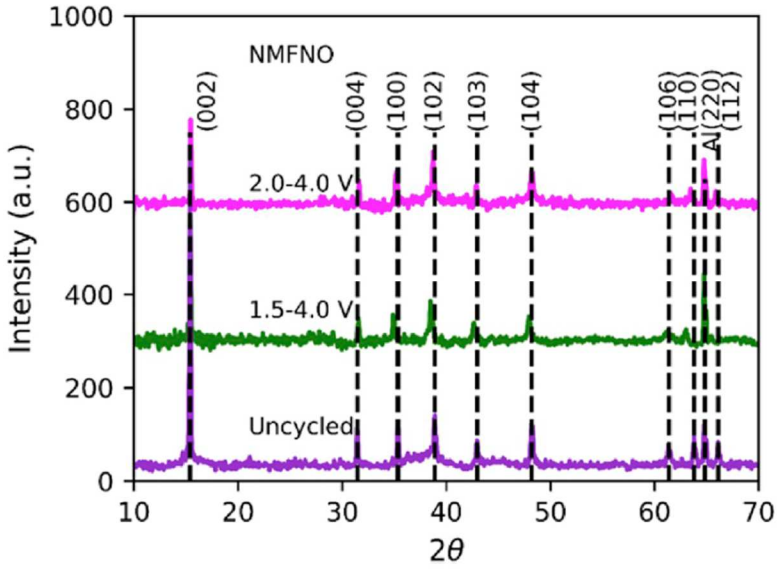

Figure 3-8. XRD diffractograms of uncycled NMFNO and NMFNO after 200 cycles in the 1.5–4.0 V and 2.0-4.0 V ranges

.

Crystal lattice parameters from Rietveld refinement of $Na_{0.67}Mn_{0.65}Fe_{0.35}O_2$ before cycling, and after 200 cycles			
Voltage Range	**a = b (Å)**	**c (Å)**	**Phase**
Uncycled	2.925	11.274	*P*6$_3$/*mmc*
1.5-4.0 V	2.909	11.247	*P*6$_3$/*mmc*
2.0-4.0 V	2.949	11.202	*P*6$_3$/*mmc*

Table 3. Lattice parameters of uncycled cells and cycled cells (upto 200 cycles) of P2-$Na_{0.67}Mn_{0.65}Fe_{0.35}O_2$ (NMFO) in 1.5-4.0 V and 2.0-4.0 V range, obtained after fitting results from data in Figure 3-7.

Crystal lattice parameters from Rietveld refinement of uncycled $Na_{0.67}Mn_{0.625}Fe_{0.25}Ni_{0.125}O_2$, and after 200 cycles.			
Voltage Range	**a = b (Å)**	**c (Å)**	**Phase**
Uncycled	2.904	11.285	*P*6$_3$/*mmc*
1.5-4.0 V	2.934	11.242	*P*6$_3$/*mmc*
2.0-4.0 V	2.918	11.206	*P*6$_3$/*mmc*

Table 4. Lattice parameters of uncycled cells and cycled cells (upto 200 cycles) of P2-$Na_{0.67}Mn_{0.625}Fe_{0.25}Ni_{0.125}O_2$ (NMNFO) 1.5-4.0 V and 2.0-4.0 V range, obtained after fitting results from data in Figure 3-8.

capacity retention of NMFO and NMFNO reduces to 66% and 69%, respectively. Thus, we find the discharge capacity of NMFNO improves over NMFO in the 1.5–4.3 V, 1.5–4.0 V and 2.0–4.0 V ranges. The higher reversible capacity of NMFNO can be due to the better Na diffusion while intercalation or due to disruption of Na-Na ordering by Ni-substitution in NMFNO. In Figure 3-10, NMFNO shows a smaller overpotential at the low voltage end in 2.0-4.0 V range, suggesting a faster Na diffusion rate. To summarize, we find that the capacity retention is more in the voltage window of 2.0-4.0 V, which avoids structural transitions as well as crystalline degradation.

.

Additionally, we report galvanostatic cycling studies up to 200 cycles for the 1.5-4.0 V and 2.0-4.0 V cycling range and extend the study of Talaie et al. [35].

Figure 3-10 shows galvanostatic cycling curves of NMFO and NMFNO in the 1.5-4.3, 1.5-4.0, and 2.0-4.0 V ranges. We observe plateaus at 4.3 V in NMFO as well as in NMFNO (Figure 3-10a and 3-10b) in 1.5-4.3 V range. These plateaus can be present due to ordering of Na^+ ion/vacancy, oxidation of the transition metal at higher voltages, or the formation of SEI layer [39]. In the next section, we further discuss the possible SEI layer formation, shown in Figure 3-11e to 3-11h. Our cycling data confirms NMFNO as an effective cathode for sodium-ion batteries when cycled in the 2.0-4.0 V range. Both NMFO and NMFNO show polarization at the end of the discharge profile in all three cycling voltage ranges. The polarization of NMFO is greater than that of NMFNO. Further research work is in progress to understand the origins of these differences.

3.2.5 Morphology of Cathodes

To further investigate the cause of capacity degradation in cathodes, we performed SEM on cycled and uncycled cathodes of NMFO and NMFNO to study the morphology changes. Figure 3-11 (c)-(h) shows SEM micrographs of NMFO and NMFNO cathode surfaces before and after cycling up to 200 cycles in different voltage ranges. In SEM images of as-prepared powdered cathode materials, shown in figures 3-11a and 3-11b, we observe that both NMFO and NMFCO are highly crystalline and have particles of average size 2-3 μm. Since both NMFO and NMFNO have particles of similar size, we conclude that charge diffusion length does not influence cycling performance or crystal structure differences between NMFO and NMFNO. Figure 3-11e to 3-11h shows SEM images of surfaces of cathodes of NMFO and NMFNO cycled up to 200 cycles in the voltage ranges 1.5-4.0 V and 2.0-4.0 V. We observe crack formation in cycled cathodes of both

NMFO and NMFNO. The uncycled cathodes of NMFO and NMFNO shown in Figure 3-11c and 3-11d display a coarse and grainy texture. On the other hand, the cycled cathodes of NMFO and NMFNO show less coarseness (see Figure 3-11e, 3-11f, 3-11g, 3-11h). We believe that the decrease in coarseness of cycled cathodes is due to the formation of a Solid Electrolyte Interface

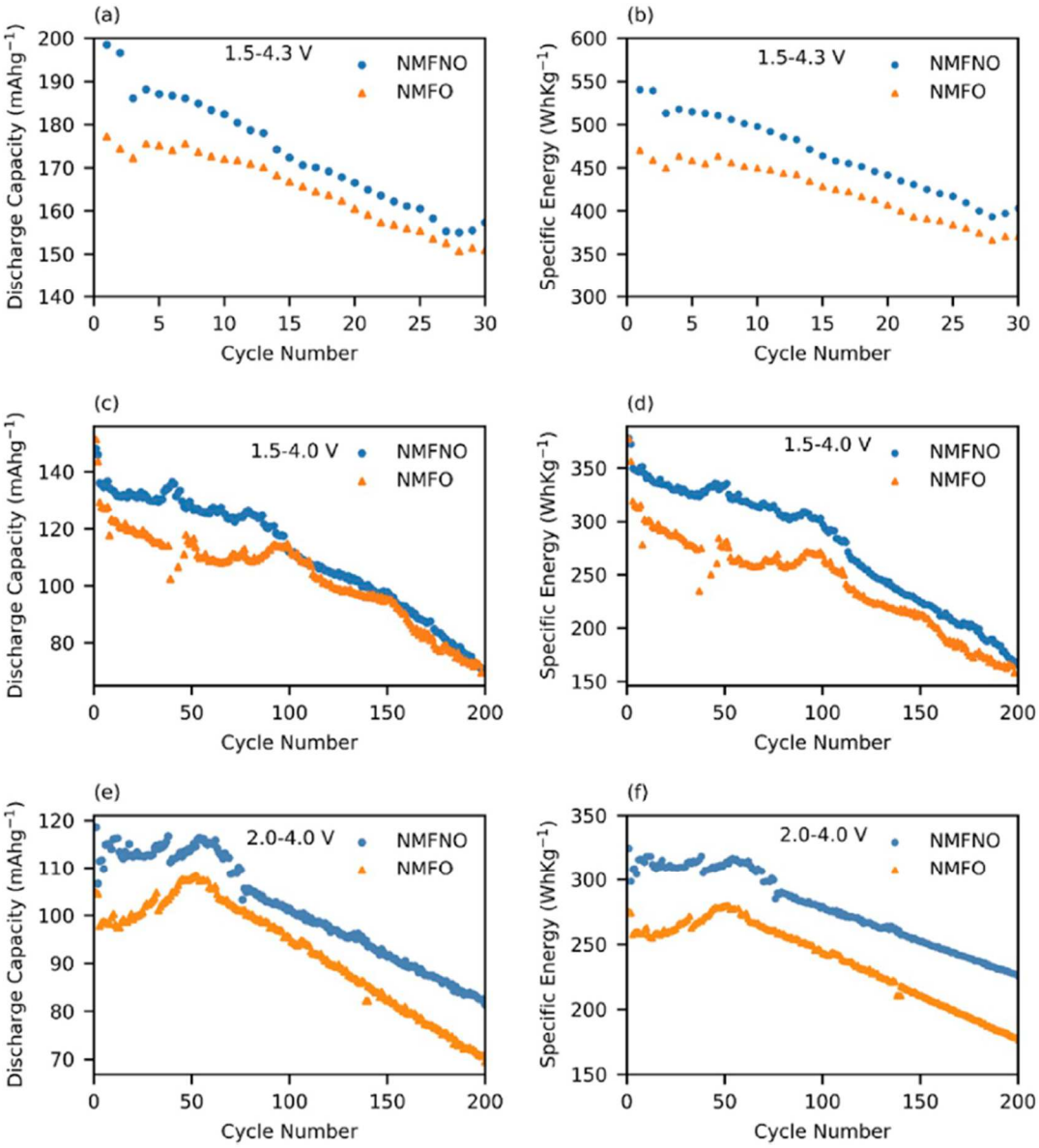

Figure 3-9. Discharge Capacity and Specific Energy of NMFO and NMFNO cycled in the voltage ranges (a, b) 1.5-4.3 V; (c, d) 1.5-4.0 V; and (e, f) 2.0-4.0 V.

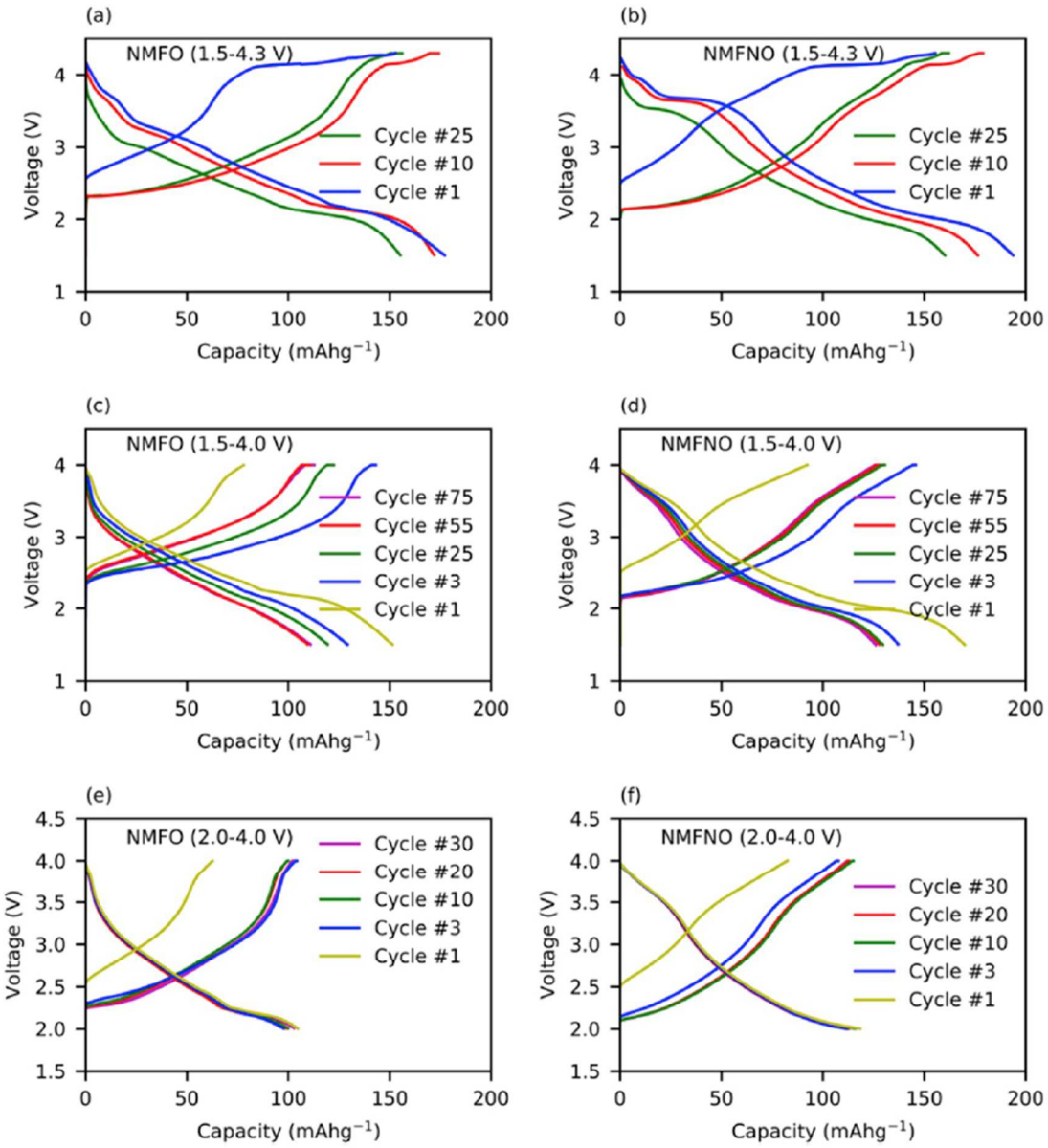

Figure 3-10. Galvanostatic cycling charge-discharge profiles at 15 mAg^{-1} (C/10) in the voltage range 1.5-4.3 V for (a) NMFO and (b) NMFNO cathodes; in the voltage range 1.5-4.0 V for (c) NMFO and (d) NMFNO cathodes; in the voltage range 2.0-4.0 V for (e) NMFO and (f) NMFNO cathodes.

.

(SEI) layer on their surface, revealed in our SEM inages as a matt-like surface layer [40]–[43]. The effect of SEI layer formation on cycling performance of cells has both with both beneficial and harmful aspects and is an active topic of research in LIBs. The formation of SEI is beneficial for the cell performance. The SEI layer formation prevents the further reaction of electrolyte with electrode surface which results in chemical and electrochemical stability of the cell while cycling. The crack formation in SEI layer, however, can lead to consumption of electrolyte and thereby leading to an increase in battery resistance and deteriorating cell performance [43].

Change in morphology and the formation of cracks on the cathode surface can also affect cycling performance of a cell. These morphology changes, also observed in LIBs, are likely due to the high strain developed due to the continuous expansion and contraction of crystal lattice during cycling. The expansion/contraction of the crystal lattice axes during repeated Na^+ intercalation/de-intercalation stresses the cathode surface and leads to crack formation. The crack formation can increase interfacial resistance and can also lead to loss of contact of particles with the current collector, leading to low cyclability. The cracks formed in the SEI layer also expose more cathode surfaces to electrolyte and leads to further reaction between electrolyte and cathode. This results in depletion of electrolyte and limits cyclability of a cell. The loss of contact between particles and cathode cracks is known as delamination. This phenomenon has been observed in LIBs and can partly explain why the cycling performance of NMFNO does not improves significantly as compared to NMFO even after the crystal-structure stabilization in NMFNO.

3.2.6 Impedance Measurements

To further study the state of health (SOH) of the cells before and after cycling, we also report Electrochemical Impedance Spectroscopy (EIS) study results in the frequency range 0.1 Hz-1000

.

kHz. Figure 3-12 shows Nyquist plots of uncycled and cycled cells (after 10 cycles and 200 cycles) of NMFO and NMFNO. A zoomed-in plot of high frequency data is shown in the inset of Figure 3-12. Basic introduction to this technique and analysis is mentioned in section 2.8. For both NMFO and NMFNO uncycled cells, two semicircles are observed. The semicircles observed are very small at high frequencies, whereas are much larger at lower frequencies. These semicircular features may be associated with charge transfer impedance at the interface between electrode and electrolyte [9]. We find that uncycled NMFNO cell has lower impedance than uncycled NMFO. We also note that the difference between NMFNO and NMFO increases with increasing number of cycles. The depressed semicircle of the NMFO becomes almost twice of that of NMFNO after 200 cycles. This signifies the increase of impedance of NMFO as compared to that of NMFNO. Figure 3-13 shows a semi-log plot of total impedance Z versus $\log_{10}$ of frequency. It is evident from this semi-log plot that the total impedance of NMFNO is lower than that of NMFO. We also notice in this plot that the total impedance of NMFO is higher at all frequencies going from 0 to 200 cycles, whereas the impedance of NMFNO remains roughly unchanged at higher frequencies between 0 and 200 cycles. The total impedance of NMFO is significantly higher than NMFNO at lower frequencies. The frequency at which the difference between the total impedance of NMFNO and NMFO becomes greater increases with increasing cycles. We are exploring the cause of this difference in impedance by numerical equivalent circuit fitting. We conclude from these impedance spectroscopy measurements that the health of NMFNO cells after cycling is better than NMFO cells. Thus, our ac impedance results are in agreement with the crystal structure and galvanostatic cycling analysis of NMFO and NMFNO cells.

(a)

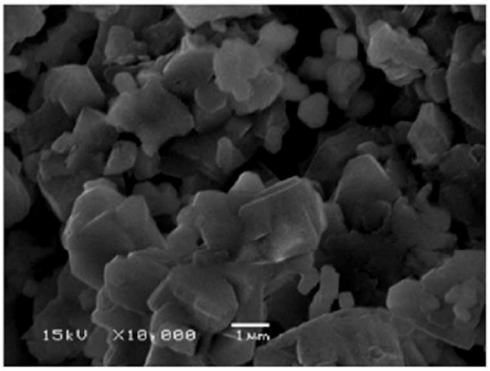
15kV X10,000 1μm

(b)

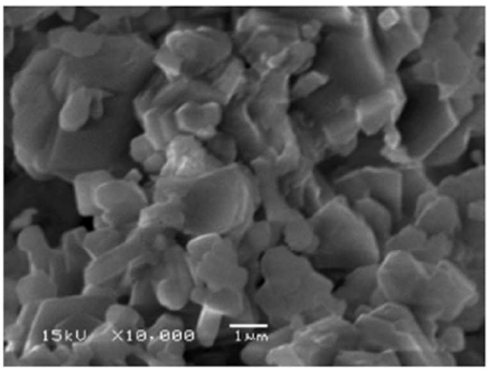
15kV X10,000 1μm

(c)

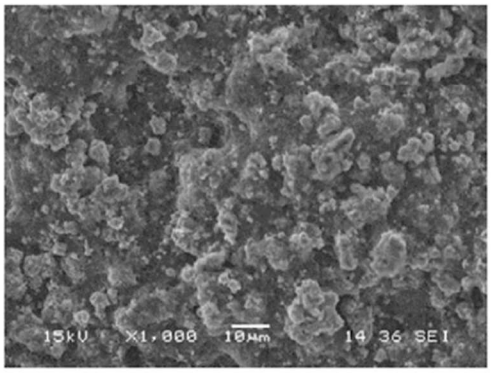
15kV X1,000 10μm 14 36 SEI

(d)

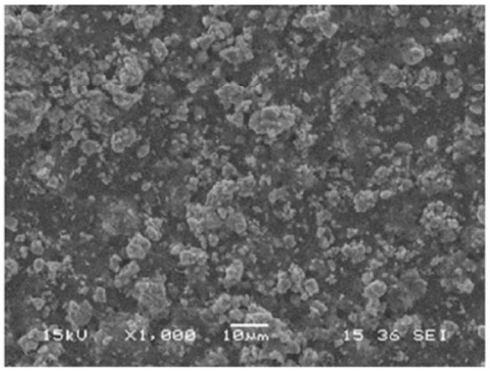
15kV X1,000 10μm 15 36 SEI

(e)

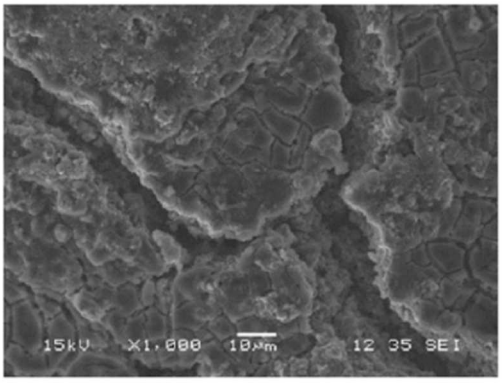
15kV X1,000 10μm 12 35 SEI

(f)

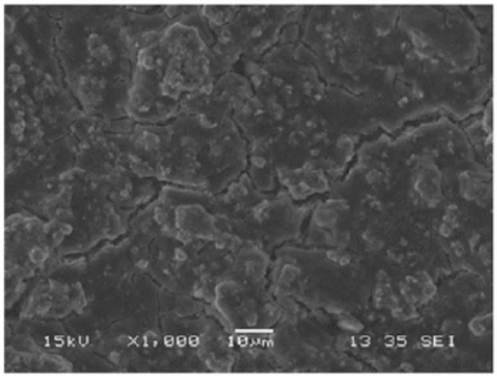
15kV X1,000 10μm 13 35 SEI

.

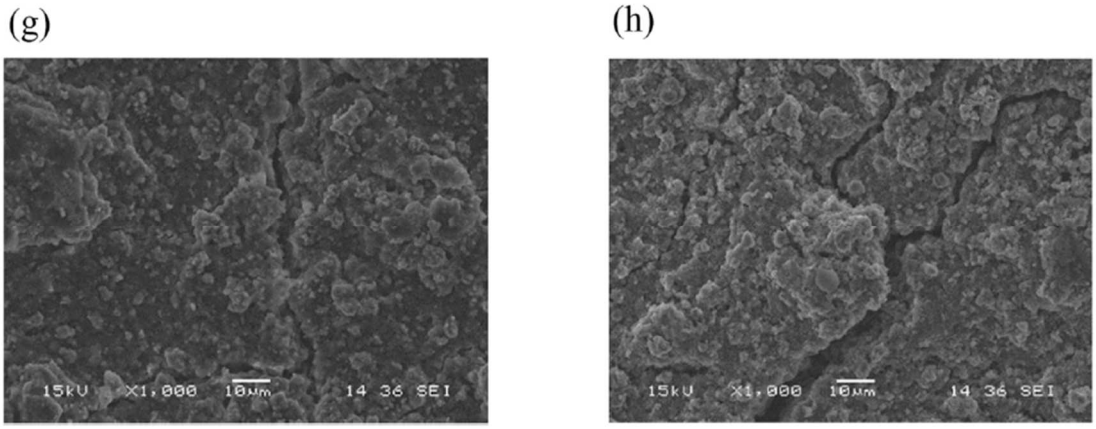

Figure 3-11. SEM images of as-prepared powder, uncycled, and cycled cathode surfaces of $Na_{0.67}Mn_{0.65}Fe_{0.35}O_2$ (NMFO) and $Na_{0.67}Mn_{0.625}Fe_{0.25}Ni_{0.125}O_2$ (NMFNO). (a) NMFO powder as-prepared; (b) NMFNO powder as-prepared; (c) uncycled NMFO cathode; (d) uncycled NMFNO cathode; (e) NMFO cathode after 200 cycles in the 1.5-4.0 V range; (f) NMFNO cathode after 200 cycles in the 1.5-4.0 V range; (g) NMFO cathode after 200 cycles in the 2.0-4.0 V range; (h) NMFNO cathode after 200 cycles in the 2.0-4.0 V range.

3.2.7 Conclusions

We performed galvanostatic, morphology, and impedance studies on pure P2-phase $Na_{0.67}Mn_{0.65}Fe_{0.35}O_2$ (NMFO) and $Na_{0.67}Mn_{0.625}Fe_{0.25}Ni_{0.125}O_2$ (NMFNO). Both NMFO and NMFNO are characterized by $P6_3/mmc$ phase. Our Rietveld analysis of XRD patterns of the NMFNO electrodes charged to 4.3 V and discharged to 1.5 V show an absence of crystal structure transitions which were observed in NMFO. However, our Rietveld analysis shows the formation of mixture of two $P6_3/mmc$ phases with unequal in-plane axes when NMFNO is discharged to 1.5 V. We also observe that c-axis expands, and in-plane axes contract due to sodium deintercalation during charging, and vice versa due to sodium intercalation during discharging. The c-axis expands

.

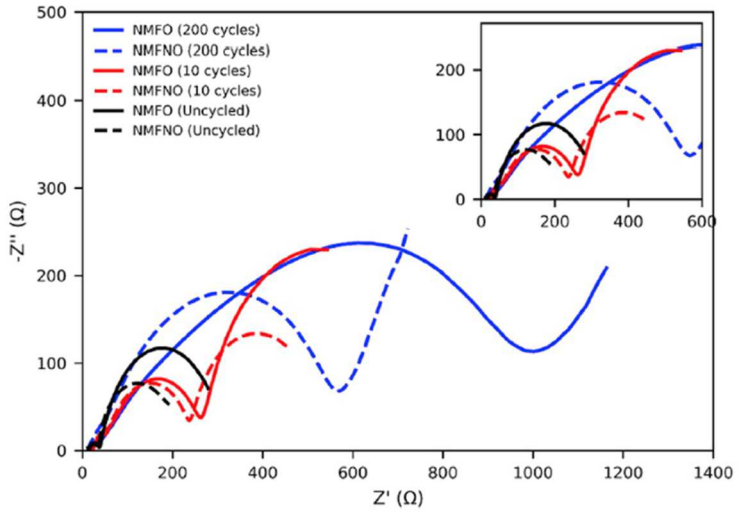

Figure 3-12. Nyquist plot of NMFO (solid line) and NMFNO (dashed line). Data is shown for uncycled cells (black), and for cells after 10 cycles (red) and 200 cycles (blue) cycled in the 2-4 V range. All the AC impedance spectra are obtained by varying frequency from 1000 kHz to 0.1 Hz. Frequencies increase from left to right of the figure, as in Fig. 3-13.

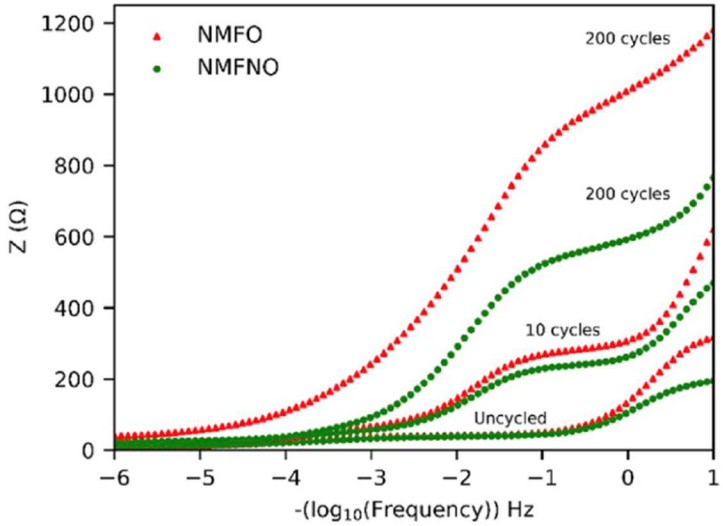

Figure 3-13. Total impedance versus negative log of frequency of uncycled and cycled (10 cycles, 200 cycles) cells of NMFO (red triangle) and NMFNO (green circle). In this plot, the frequency decreases from left to right as in Fig. 3-12.

during de-intercalation as the screening of electrostatic repulsion between successive oxygen layers decreases as the sodium ions deintercalated during charging. In this work, we extend the galvanostatic cycling to 200 cycles. We observe that the cyclability and discharge capacity of NMFNO remain superior than that of NMFO up to 100 cycles in the 1.5-4.0 V range, and up to 200 cycles in the 2.0-4.0 V range. We conclude from our Rietveld analysis results that the substitution of Fe with Ni stabilizes the crystal structure of NMFNO during cycling by alleviating crystal structure transitions observed in the case of NMFO. Morphology studies of cathodes using Scanning Electron Microscopy after 200 cycles reveal the formation of cracks and a solid electrolyte interface (SEI) layer; we present our preliminary results here to initiate further detailed work on Na-ion cathodes. We observe crack formation on the cathode surface. These are similar to those observed in Li-ion batteries (LIBs). Such crack formation is well-studied in LIBs but not yet extensively studied in Na-ion batteries. In summary, even though Ni-substitution in NMFO stabilizes the crystal structure during cycling, the crack formation after 200 cycles leads to the degradation of cycling performance of cathodes in our results. Given this stabilizing effect of Ni in NMFO, further work is needed to reduce the crack formation by improving cathode design which could make NMFNO a promising cathode material for sodium ion batteries.

3.3 P2-$Na_{0.67}Mn_{0.625}Fe_{0.25}Co_{0.125}O_2$ as the Positive Electrode for Na-ion Batteries

3.3.1 Introduction

The study of sodium ion-transition metal oxide cathodes dates back to the earliest research on lithium and sodium ion batteries, as mentioned in previous sections. Fouassier et al. studied Na_xMO_2 with M = Mn, Co, Cr in the 1970s, and Delmas et al. studied the stacking structure of

.

such compounds in the 1980s, leading to the Delmas notation for stacking patterns [23], [44]. With the recent focus on sodium ion batteries due to concerns about the sustainability of lithium resources, the subject has become popular again, and examples of more recent work using Co as one of the transition metal ions include studies by Wang et al. and Meng et al. on the phase stability of sodium cobalt oxide, and a study by Bucher et al. on the relation between morphology and cycling stability in sodium manganese cobalt oxide [45]–[47].

As described in previous sections, layered cathode materials with transition metals present in MO_6 layers can suffer from Jahn-Teller distortion. Cobalt is known to possess a low-spin cobalt (II) oxidation state which is Jahn-Teller active [48]. However, at higher voltage, Co generally oxidizes to 3+ or 4+ oxidation states which are not Jahn-Teller active [29]. The NMFCO structure we report in this chapter is based on

the idea that Co could help minimize structural distortions in NMFO and thereby, improving the cyclability of cells.

In addition to studying the effect of Ni substitution in cathode materials, we also studied the effect of Co substitution on the cyclability and discharge capacity of cathodes. We synthesized $Na_{0.67}Mn_{0.625}Fe_{0.25}Co_{0.125}O_2$ (NMFCO) to study its cyclability and morphology changes during cycling. This system is related to P2-type $Na_{0.67}Mn_{0.65}Fe_{0.35}O_2$ (NMFO) which has been studied by us, and by others [35], [36], [49]. Liu et al. has studied similar composition [50]. Since Co is costly and toxic, we reduce the amount of Co in NMFCO than used by Liu et al. [50] Since Na-ion battery research area is still novel, it is important to explore new electrode materials. It is also important to explore electrode materials which have the promise of reducing negative impact on the environment. Thus, beyond the basic science information such studies can provide, use of a

.

significantly lower amount of Co is worthy of study from the point of view of the severe environmental impact of the mining, toxicity, and high dollar cost of Cobalt.

In this chapter, we report electrochemical performance, morphology changes, and the structural evolution during charge/discharge of NMFCO cycled 200 times using Rietveld refinement of XRD data. We also perform the Electrochemical Impedance spectroscopy (EIS) to study the state of health (SOH) of cells after cycling. We also report the analysis of Nyquist plots and the quantitative information about the effects of cycling on different cell components in equivalent circuit model. Additionally, we compare this with active polarization obtained from galvanostatic plots to evaluate the internal resistance of our cells. Our study reveals that the internal resistance of cells due to formation of Solid Electrolyte Interface (SEI) layer on the cathode surface is lower in NMFCO as compared to NMFO when they are cycled 200 times. Finally, we discuss factors affecting the changes in morphology of the cathode at the electrode-electrolyte interface for NMFCO cathodes.

3.3.2 Experimental Details

The target composition, $Na_{0.67}Mn_{0.625}Fe_{0.25}Co_{0.125}O_2$, was synthesized by a solid-state method. Stoichiometric amounts of Na_2CO_3 (98% Alfa Aesar), Fe_2O_3 (99.99% Alfa Aesar), MnO_2 (99.9% Alfa Aesar), and CoO were mixed together using a high energy ball mill and then pressed into pellets. CoO was synthesized by the thermal decomposition of cobalt carbonate. Cobalt carbonate was kept in a ceramic boat and heated at 500°C for 3 hours in the argon atmosphere. The furnace was then turned off and cooled to room temperature. Pellets were reacted at 900°C in air for 12 hours, cooled to 600°C at 5°C/ min, and then quenched in air to room temperature from 600°C. Pellets were then stored inside the glovebox in an ultra-high purity argon atmosphere. XRD

measurements were performed on Bruker D8 Diffractometer using Cu-Kα radiation. Ni filter was used to filter Cu-Kβ radiation while performing XRD. The slurry was prepared with an 8:1:1 weight ratio of active material; carbon black (C65); and polyvinylidene fluoride (PVDF) in N-methyl-pyrrolidone (NMP, 99.5% Sigma Aldrich). The slurry was then coated on aluminum foil used as a current collector with a loading mass of 4-5 mg/cm^{-2} to fabricate cathodes. The cathodes were dried in a vacuum oven at 60°C. The electrolyte was prepared with 1 M solution of sodium perchlorate ($NaClO_4$, 99.8% Sigma Aldrich) dissolved in a 1:1 by volume mixture of ethylene carbonate (EC) and diethylcarbonate (DEC). 2032 assembly coins cells were fabricated inside the glove box filled with ultra-high purity argon and having oxygen content less than 1 ppm. Electrochemical performance of the NMFCO cathodes was analyzed using CR2032 coin cell assembly. We also performed studied the morphology of uncycled and cycled cathodes. As described in previous sections, Scanning Electron Microscopy (SEM) was performed on a JEOL JSM-6460 LV scanning electron microscope. We also performed an Electrochemical Impedance Spectroscopy (EIS) study to further assess SOH of the cells. We performed EIS on uncycled cells and cells cycled for 10 and 200 times, using an AutoLab PGSTAT30 potentiostat from Metrohm with Nova 1.7 software. The EIS was performed in the 1000 kHz to 0.1 Hz frequency range with logarithmic frequency steps, and an AC excitation signal of 10 mV.

3.3.3 Structural Transitions

The XRD diffractogram and the Rietveld analysis of synthesized cathode material confirms an undistorted P2 crystal structure (space group *$P6_3/mmc$*) of the sample. No impurity peaks or second phases are detected in the diffraction patterns. The P2 structure (Figure 3-15) can be described as a stack of edge-sharing MO_6 layers accommodating two different prismatic sodium

.

sites in between, Na_e and Na_f, which share edges and faces, respectively, with the MO_6 octahedra [37].

The ex-situ XRD was performed on cycled cathodes by stopping charge cycling at different charge and discharge voltages to study the crystal structure changes during the sodium insertion/extraction processes. To perform XRD on cycled cathodes, the coin cells were opened inside the glove box. The cathodes were then taken out and washed with DMC solution to remove electrolyte from the surface. The cathodes were soaked in DMC solution for 24 hours and dried at 50°C inside the vacuum chamber. The XRD was performed in an airtight XRD holder to prevent the exposure of cathodes to air. Figure 3-14a shows the XRD of NMFCO cathode material charged and discharged at different voltages (also see Table 5). During the first 10 cycles, the cells were charged to 4.3 V and discharged to 1.5 V. Their cycling was stopped at various charge and discharge voltages at the 11^{th} cycle. We observe the structural transition to the Z/OP4 phase at 4.3 V, and to the *Cmcm* phase at 1.5 V are absent in Co-substituted NMFCO. However, these transitions are observed by us in NMFO by us and other authors [34], [35], [49]. We observe through Rietveld analysis that NMFCO maintains its pristine P2 crystal structure upon charging to 4.3 V. New peaks are observed near the (102), (103), and (104) peaks in NMFCO at 1.5 V discharge. We interpret this as the formation of a new phase with same crystal structure and symmetry, but with different crystalline axes, a = b. Figure 3-14b shows Rietveld refinement of this two-phase mixture. The additional shoulder peaks are fitted with another $P6_3/mmc$ phase, with a' = b' = 3.076 Å.

In contrast with this result, Liu et al. do not observe a phase transition at 1.5 V discharge voltage [50]. Additional effort in fitting the XRD diffractogram at 1.5 V discharge voltage with *Cmcm* phase, following up the Rietveld analysis performed by Boisse et al. for P2-$Na_xMn_{1/2}Fe_{1/2}O_2$

.

discharged to 1.5 V, led to an alternative result [32]. The shoulder peaks formed at 1.5 V discharge can be fitted well both with the mixture of two $P6_3/mmc$ phases and the *Cmcm* phase. At the time of writing of this dissertation, it remains unclear to us as to whether what is forming is a mixture of two $P6_3/mmc$ phases or a *Cmcm* phase. Some of this is limited by the signal-to-noise quality accessible to a lab-based X-ray diffractometer such as the Bruker D8 and Linxeye detector. Further research and analysis, perhaps using a synchrotron source, which can help improve signal-to-noise, is needed to determine which of the two phases is forming at 1.5 V discharge voltage. We also need to follow up this work with "operando" or true in situ experiments.

Broadly speaking, our data reveals a degradation of crystalline quality at high (4.3 V) and low (1.5 V) voltage in NMFCO as the XRD peaks broaden even though the crystal structure transitions are suppressed. Table 5 shows the changes in lattice parameters of NMFCO during cycling obtained after Rietveld analysis of the XRD diffractograms measured at different voltages. As the cell charge to higher voltages, the c-axis increases due to de-intercalation of Na ions from prismatic sites. As the sodium ions de-intercalate from sites, the screening effect decreases and the repulsion between oxygen layers increases and results in the expansion of c-axis [35], [51]. The in-plane a and b axis decrease due to the oxidation of transition elements sitting inside the MO_6 octahedron.

A comment is in order on the subject of the Jahn-Teller effect, because cobalt possesses an oxidation state that is strongly Jahn-Teller active. The Jahn-Teller effect occurs in a molecular system when there is a degenerate electronic state, and results in a distortion that reduces the symmetry and energy of the system. This can result in a lengthening or shortening of different bonds. It is an important consideration in battery electrodes because of the possibility that this distortion will aid or inhibit the diffusion of ions during charge-discharge cycling. The strongly

.

Jahn-Teller active cobalt state is low-spin cobalt (II). In the case of NMFCO, the cobalt will be oxidized to the +3 or +4 state. Because of this, we don't expect any Jahn-Teller distortion to occur

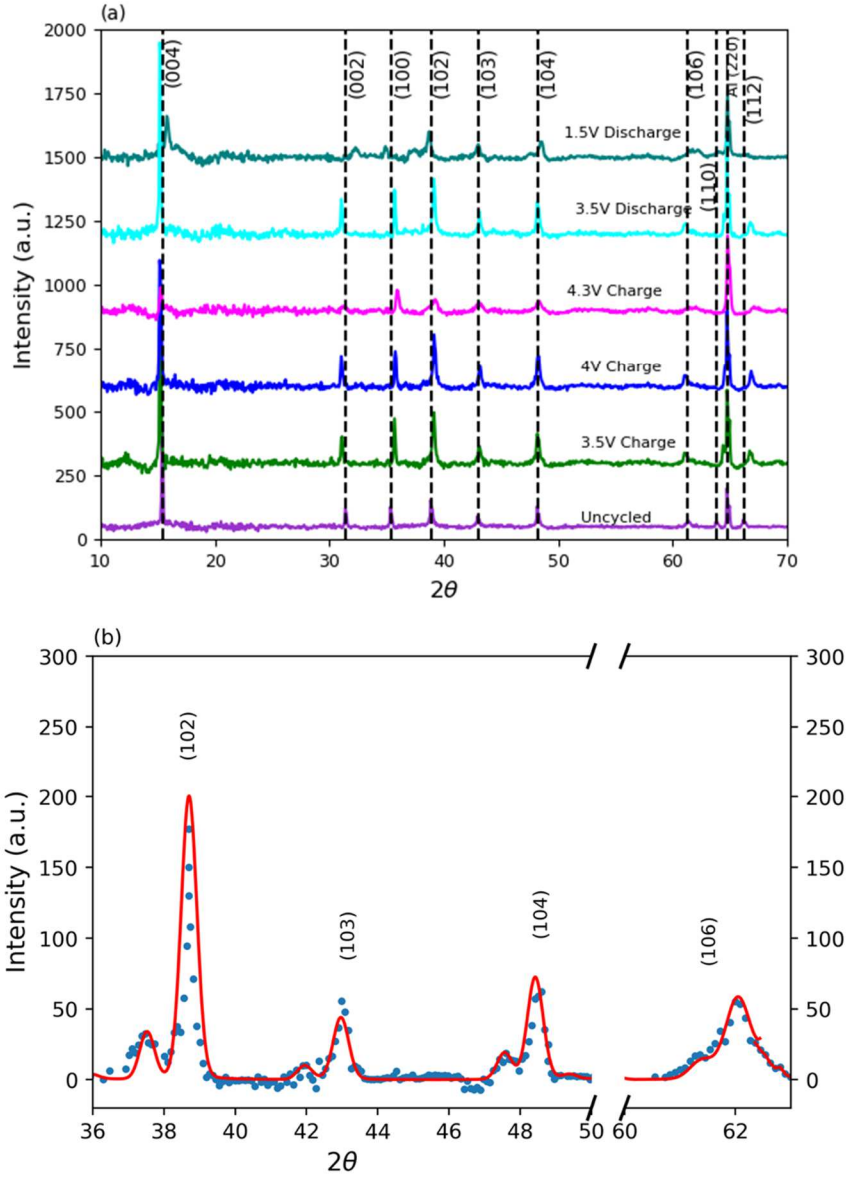

Figure 3-14. (a) XRD diffractograms of NMFCO cathode material charged and discharged at different voltages (also see Table 5) during cycling in the voltage range 1.5-4.3 V. (b) XRD diffractogram of NMFCO at 1.5 V. Red curve is the Rietveld fit and blue points are the XRD data points.

.

Crystal lattice parameters from Rietveld refinement of $Na_{0.67}Mn_{0.625}Fe_{0.25}Co_{0.125}O_2$ during cycling			
Voltage (V)	**a = b (Å)**	**c (Å)**	**Phase**
Uncycled	2.900	11.329	*P*6$_3$/*mmc*
3 V Charge	2.886	11.349	*P*6$_3$/*mmc*
4 V Charge	2.875	11.402	*P*6$_3$/*mmc*
4.3 V Charge	2.856	11.399	*P*6$_3$/*mmc*
3.5 V Discharge	2.877	11.392	*P*6$_3$/*mmc*
1.5 V Discharge	2.953	11.084	*P*6$_3$/*mmc*
	3.076	11.084	

Table 5. Evolution of lattice parameters of P2-type NMFCO at different voltages during cycling in the 1.5-4.3 V range. These are fitting results from the data in Figure 3-14.

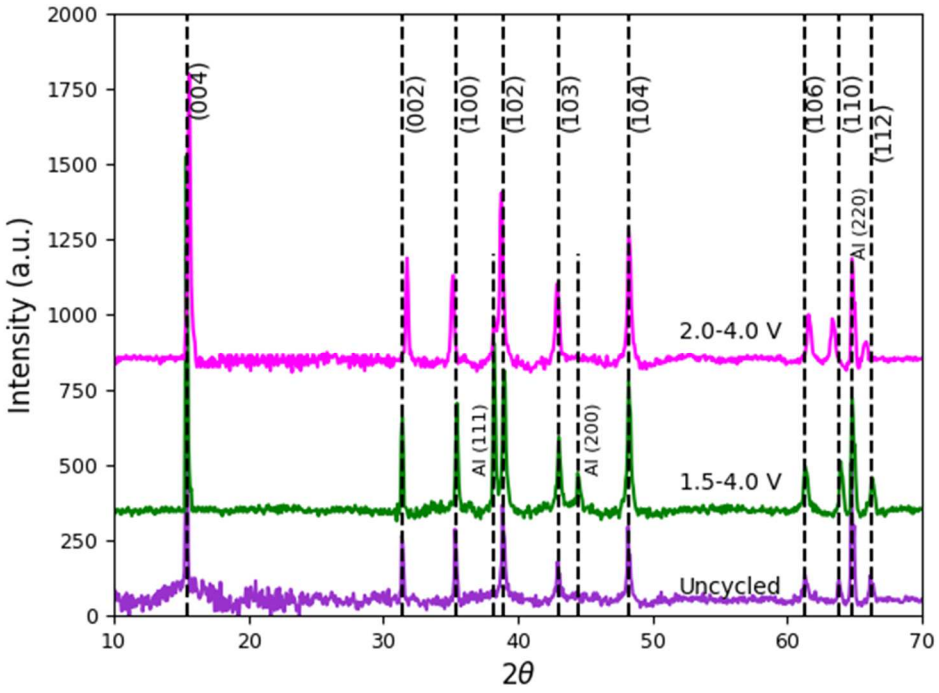

Figure 3-15. XRD diffractogram of uncycled and cycled $Na_{0.67}Mn_{0.625}Fe_{0.25}Co_{0.125}O_2$ after 200 cycles in the 1.5-4.0 V and 2.0-4.0 V ranges.

.

in NMFCO, in contrast to some other materials in the sodium-transition metal-oxide families that have elements with multiple Jahn-Teller-active modes. Figure 3-15 shows the crystal lattice parameters of uncycled P2-type NMFCO, together with results after 200 cycles, in the 1.5-4.0 V and 2.0-4.0 V ranges. It is important to note that although we find a suppression of mid-cycle crystal structure changes in NMFCO when compared with NMFO, both cathode types revert to their pristine P2-type crystal structure in the open-circuit state following 200 cycles.

3.3.4 Results from Electrochemistry and Galvanostatic measurements

We also examine the impact of Co substitution on cycling performance, discharge capacity and specific energy of cathodes. Figure 3-16 shows the discharge capacity and specific energy of NMFCO and NMFO cathodes during constant current charging and discharging in the 1.5-4.3 V, 1.5-4.0 V, and 2.0-4.0 V range. These three voltage windows mentioned above are selected to allow as well as avoid crystalline degradation and crystal structure transitions [35]. In each voltage range, the first two formation cycles are at C/20 rate (0.047 mA) and the remaining cycles are at C/10 rate (0.0945 mA). In 1.5-4.3 V range, we observed that NMFCO has capacity of around 195 mAh/g and better cyclability than NMFO. We were not able to cycle the cells beyond 40 cycles in 1.5-4.3 V range possibly due to electrolyte degradation. In the 1.5-4.3 V range, cathode undergoes structural transitions. NMFCO displays a first-cycle specific energy of 520 Whg^{-1}, compared with 470 Whg^{-1} for NMFO in the voltage range 1.5–4.3V. We cycled NMFCO and NMFO up to 200 times in the 1.5-4.0 V, and 2.0-4.0 V voltage ranges. NMFCO retains 71% capacity as compared to NMFO which retains 55% capacity after 200 cycles in the voltage range 1.5-4 V. NMFCO retains 66% capacity while NMFO retains 64.76% capacity after 200 cycles in the voltage range 2.0-4.0 V. Thus, we conclude that the discharge capacity of NMFCO improves over NMFO in the

.

1.5-4.3 V, 1.5-4.0 V, and 2.0-4.0 V voltage ranges. Liu et al report that $Na_{2/3}Mn_{½}Fe_{¼}Co_{¼}O_2$ has higher discharge capacity as compared with other P2-type layered cathode materials [50]. Our results reveal that NMFCO has high energy capacity, but after a few cycles discharge capacity of $Na_{0.67}Mn_{0.625}Fe_{0.25}Co_{0.125}O_2$ is nearly equal to P2- $Na_{0.67}Mn_{0.625}Fe_{0.25}Ni_{0.125}O_2$.

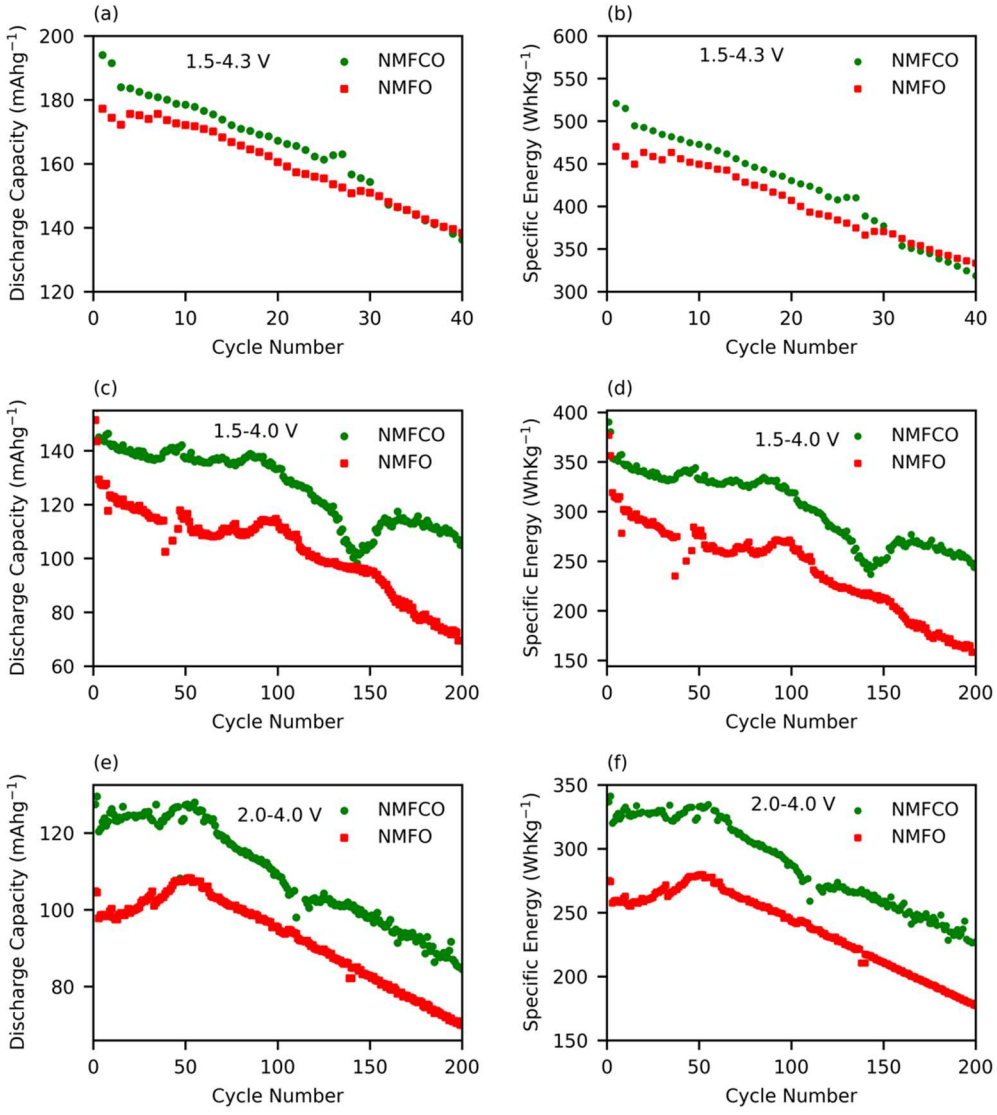

Figure 3-16. Discharge Capacity and Specific Energy of NMFO and NMFCO cycled in the voltage ranges (a, b) 1.5-4.3 V; (c, d) 1.5-4.0 V; and (e, f) 2.0-4.0 V.

.

Figure 3-17 shows the cycling curves of NMFCO cycled in the voltage ranges 1.5-4.3 V, 1.5-4.0 V, and 2.0-4.0 V. The plateaus observed in 1.5-4.3 V range near 3.75 V are absent in 1.5-4.0 V and 2.0-4.0 V range. The plateaus observed in 1.5-4.3 V range are due to the presence of structural transitions. As evident from the cycling curves, the internal resistance of NMFCO is less as compared with NMFO.

We also analyzed the initial slope from galvanostatic results shown in Figure 3-17 to compare the internal resistance of the cells during cycling [52]. The initial slope in galvanostatic cycling curves characterizes active polarization at cathode surface which arises due to the charge transfer process at electrode-electrolyte interface [52]. Figure 3-18 shows the initial slope of galvanostatic discharge curves plotted for all 200 cycles for NMFO and NMFCO cathodes. We find that general trends between NMFO and NMFCO do not significantly change for other reasonable choices of energy capacity range. The linear region used to find the initial slope was chosen to be in the 0 - 3.6 $mAhg^{-1}$ energy capacity range. Extreme outliers, attributed to voltage fluctuations, are not shown in the figure.

An inspection of the initial slope of NMFCO shown in Figure 3-18 immediately reveals that the internal resistance of NMFCO is less as compared with NMFO. Thus, we conclude that the active polarization of NMFCO is less than that of NMFO. This is due to the reduced kinetic hindrance to the charge transfer process at the cathode-electrolyte interface in the case of NMFCO [52]. This kinetic hindrance to charge transfer presents itself as an increase of the total internal resistance of the cell, as demonstrated by our analysis and modeling of the Electrochemical Impedance Spectroscopy discussed in later sections. Therefore, we conclude that the internal resistance of NMFCO is less than NMFO, indicating that the state of health of the NMFCO cells is superior to that of NMFO.

.

We observe that the size of the error bars in Figure 3-18 increases beyond 20 cycles in Figure 3-18a, and beyond 100 cycles in Figure 3-18b. This may happen due to a deviation from linearity of the initial slope of the galvanostatic curve which indicates a change in nature of the resistive element of the equivalent circuit shown in Figure 3-20. The error bars in NMFO increase early than NMFCO during cycling as shown in Figure 3-18. This is because the degradation of NMFO cathode earlier than NMFCO when cycled repeatedly. We will describe the effect of this on the equivalent circuit in a separate paper [53]. We conclude from Figure 3-18 that the active polarization and equivalent internal resistance of NMFCO is less than that of NMFO. This implies that NMFCO cells maintain superior state of health when compared with NMFO cells.

3.3.5 Morphology of Cathodes

To further investigate the cause of capacity degradation in NMFCO cathodes, we performed SEM on cycled and uncycled NMFCO in the voltage range 1.5-4.0 V as shown in Figure 3-19. We observed cracks on surface in the cathodes cycled in 1.5-4.0 V and 2.0-4.0 V range. We observed cracks on surface in the cathodes cycled in 1.5-4.0 V range. The effect of crack formation on battery performance has been extensively studied in Li-ion batteries, but not much in the case of Na-ion batteries [49]. High strain developed in the crystal lattice during intercalation and deintercalation of sodium ions during cycling could lead to crack formation on cathode's surface. The unit cell volume decreases from 95.28 $Å^3$ for uncycled cells to 93.91 $Å^3$ for cells that are charged to 4 V. The unit cell's volume change due to deintercalation of Na ions can lead to crack formation. The formation of cracks also causes interfacial resistance which leads to the decrease in discharge capacity. The cracks also lead to more consumption of electrolyte and thus limit cyclability of a cell. We also observe that the surface of uncycled NMFCO cathode surface is

.

grainy as shown in Figure 3-19a. However, the surface of the cycled cathodes is not grainy as shown in Figure 3-19b and Figure 3-19c. This indicates the formation of a matt-like deposition, a solid electrolyte interface (SEI) layer on the surface of cycled cathode. SEI layer is formed due to the interfacial chemical reactions between electrolyte and electrodes. The formation of cracks in cycled cathodes leads to electrolyte depletion as the electrolyte seeps into the cracks and further reacts with cathode material. As a result, the electrolyte depletion limits battery performance.

3.3.6 Impedance Measurements

We also performed electrochemical impedance measurements on uncycled and cathodes cycled 10 and 200 times. Freshly prepared cells have less impedance as compared to the cycled ones as shown in Figure 3-20a and 3-20b. The same cells were used for the uncycled and 10 cycle tests and a different cell was used for the 200 cycle test for both NMFO and NMFCO. Figure 3-20a shows Nyquist plots which display in phase and out of phase component of impedance. The frequency of plot decreases as real impedance (resistance) increases. We observe that the size of depressed semicircle at high frequencies, associated with the formation of an SEI layer, increases for NMFO as well as NMFCO as cycling is increased [54], [55]. Semicircles in the 1 kHz - 10 mHz frequency range are thought to correspond to the charge-transfer processes from the electrolyte to the cathode. The frequency range < 10 mHz is characterized by diffusion processes in the electrodes [56]. Figure 3-20b shows the total impedance versus the logarithm of frequency. We observe that the total impedance of NMFO is much greater than NMFCO at lower frequencies. This can be associated with the greater emergence with cycling of some capacitive element in NMFO, compared to NMFCO.

.

To further understand the electrochemistry, and the State of Health (SoH), of our cells, we modeled equivalent circuits using the impedance spectra for both NMFO and NMFCO. Our group developed an equivalent circuit modeling program in Python. This modeling begins with an examination of the impedance spectrum to determine the number and type of the circuit elements that are likely to factor into the model. Starting with an initial estimate of the values for each circuit element based on the size and shape of the Nyquist plot, the program generates a best fit for the circuit elements modeled in Figure 8c. Our cells were effectively modelled by three pairs of a resistor in parallel with a constant-phase element (CPE), and a separate CPE and a resistor in series with them. The simulated dataset agreed well with the measured impedance versus frequency data for our cells. A CPE is a circuit element used to describe capacitance in real electrochemical systems. It is used to describe an imperfect capacitor that does not have a fixed boundary due to the porosity of the cathode material. The impedance of CPE by itself results in a straight line. A parallel combination of CPE and a resistor leads to a semicircular feature in cell's impedance in the Nyquist plot. A semicircle or the straight-line "tail" of the Nyquist plot at low frequencies, could not always be fitted reliably in some cells. Hence, we did not fit it with a separate CPE or resistor-CPE circuit loop. For this reason, the first resistor-CPE loop and the separate CPE are excluded from the fit for some cells and the parameters corresponding to them are left blank in Table 6. We use the following definitions to describe Nyquist plots:

R, CPE Loop 1 (high frequency)	f > ~100Hz
R, CPE Loop 2 (mid frequency)	~1Hz < f < ~100Hz
R, CPE Loop 3 (low frequency)	100 < f < 1,000 mHz

Here, f denotes the frequency at the peak of the semicircle. The impedance behavior of a cell is modeled by a parallel combination of resistor and CPE. The resistor models the charge-transfer

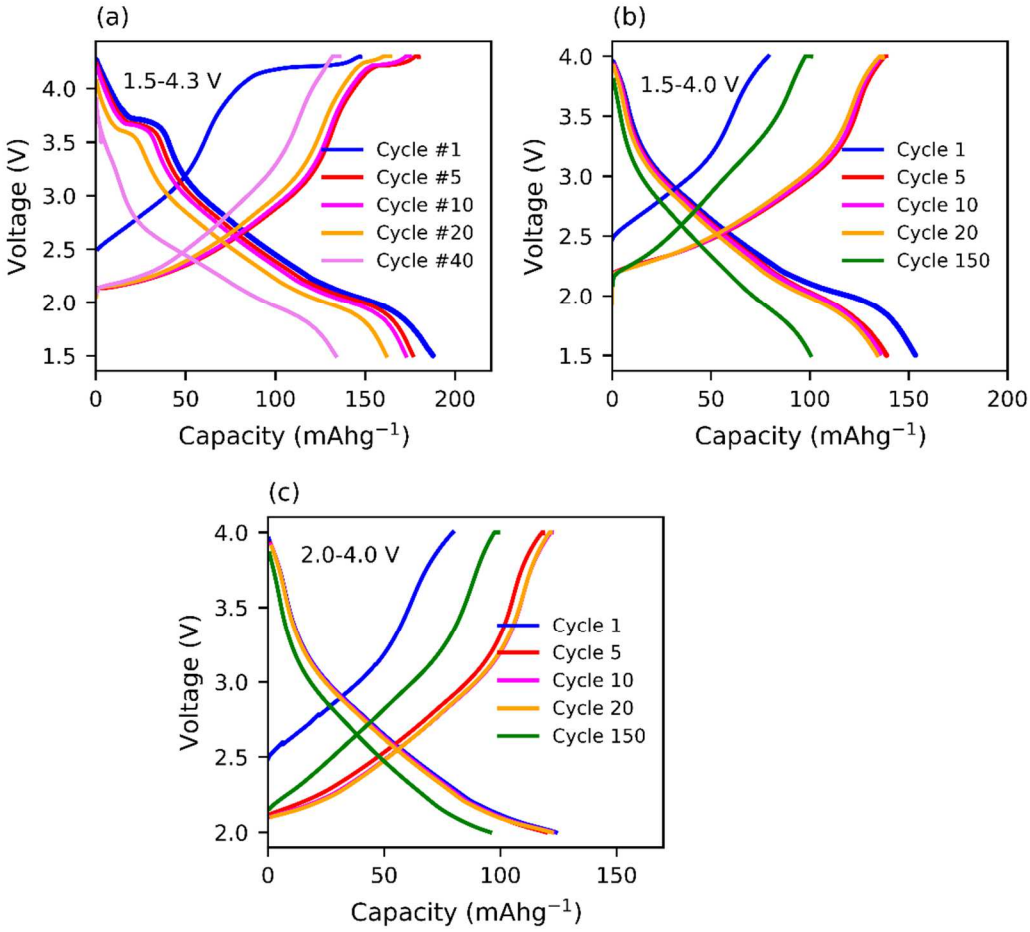

Figure 3-17. Cycling curves of NMFCO cathodes cycled in the voltage ranges 1.5-4.3 V, 1.5-4 V and 2-4 V range.

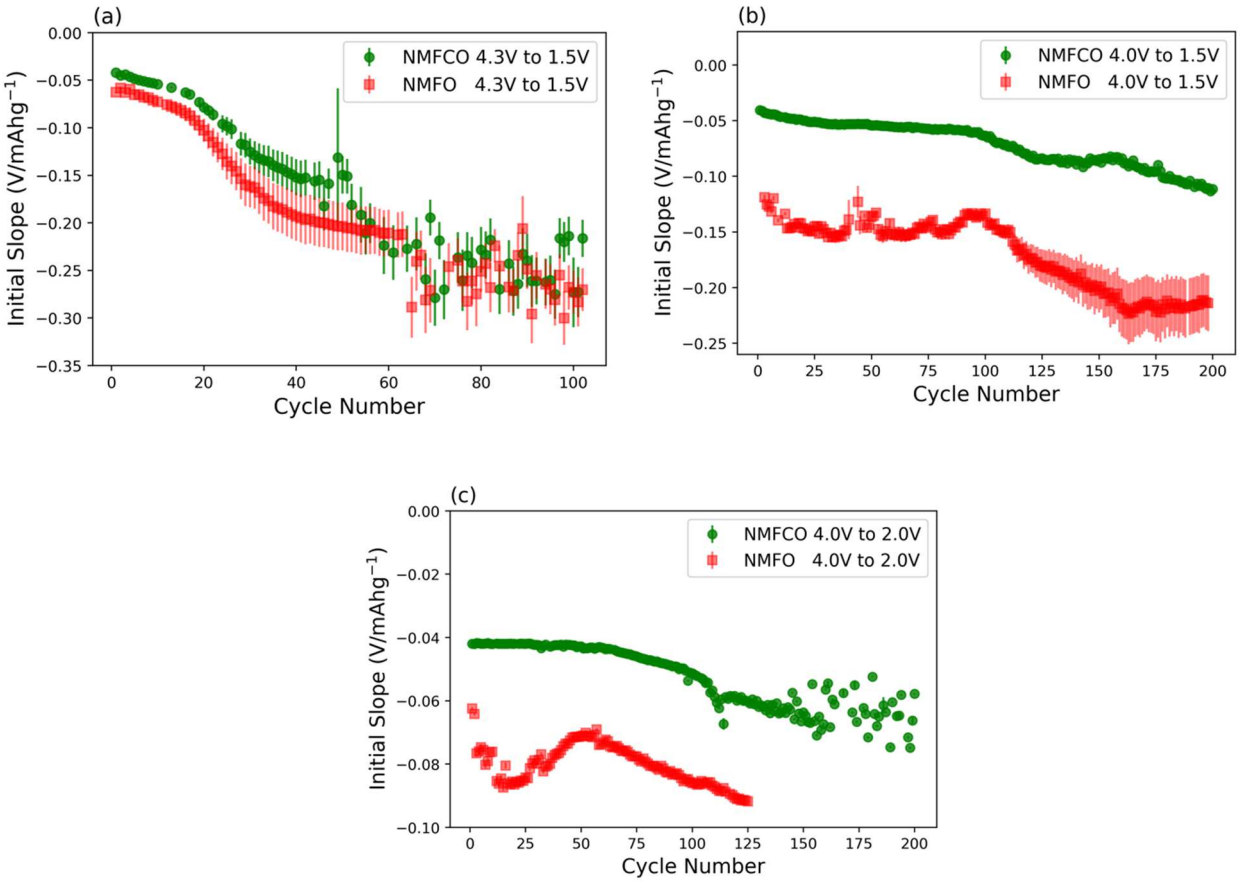

Figure 3-18. Initial slope of galvanostatic discharge curves as a function of cycle number. The data was obtained from our galvanostatic charge-discharge measurements, including data shown in Figure 3 for different cycle numbers, for NMFO and NMFCO cathodes in the (a) 1.5-4.3 V, (b) 1.5-4.0 V and (c) 2.0-4.0 V ranges. Points depict best fit slopes in the 0-3.6 mAhg^{-1} energy capacity range.

.

(a) (b)

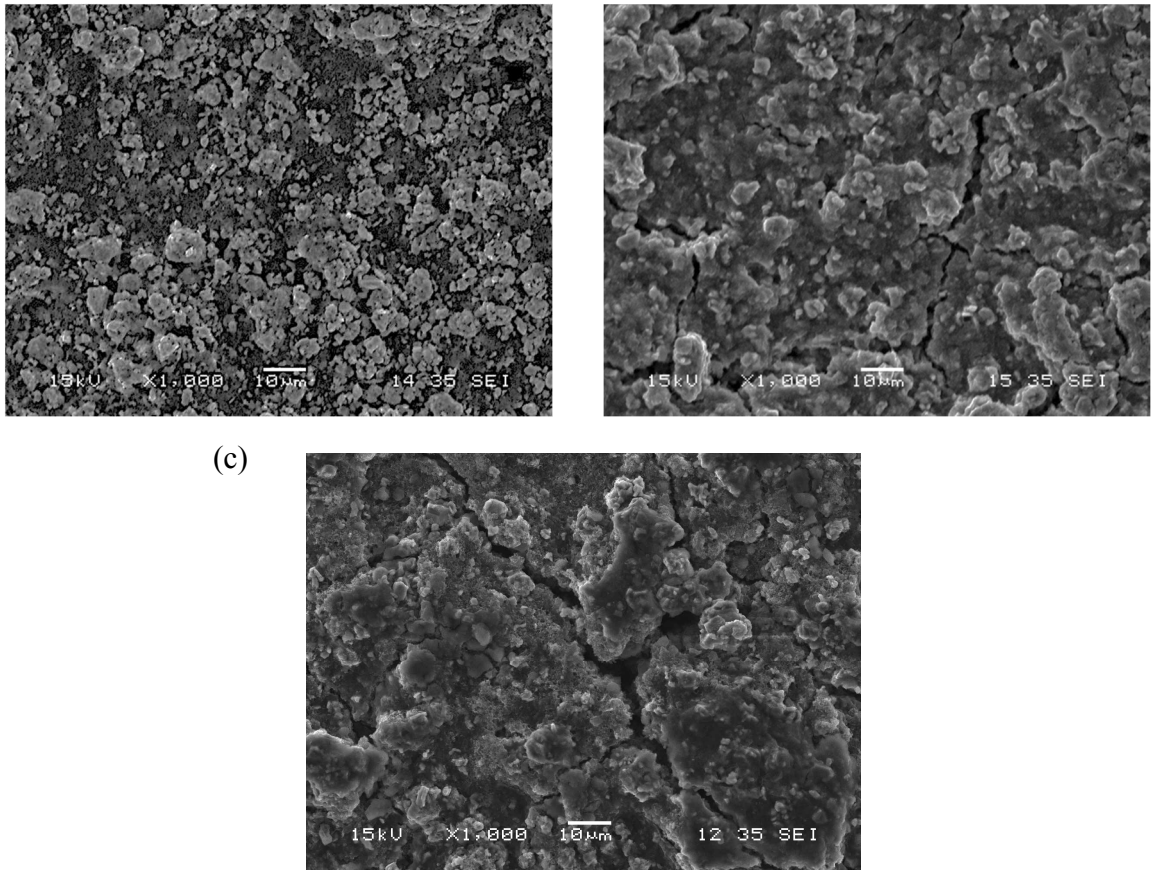

Figure 3-19. SEM images of $Na_{0.67}Mn_{0.625}Fe_{0.25}Co_{0.125}O_2$ (NMFCO) cathode surfaces as prepared, and after cycling. (a) uncycled cathode; (b) After 200 cycles in the 1.5–4.0 V range; (c) After 200 cycles in the 1.5-4.0 V range.

(a)

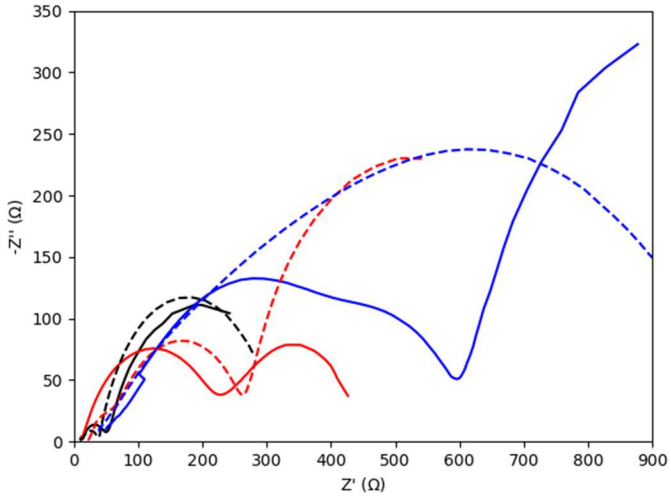

(b)

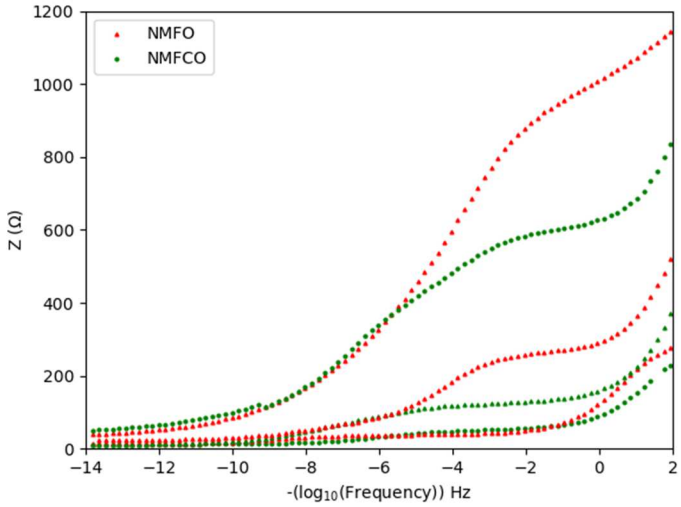

(c)

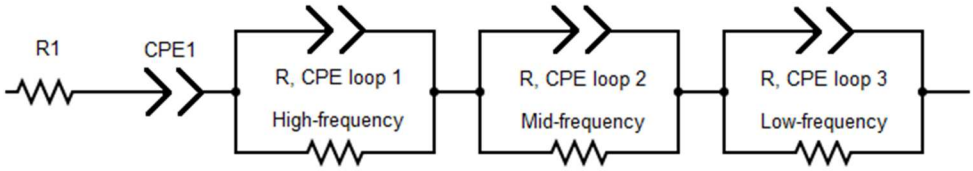

Figure 3-20. (a) AC impedance spectra of NMFO (dashed line) and NMFCO (solid line). Data is shown for uncycled cells (black), and for cells after 10 cycles (red) and 200 cycles (blue) cycled in the 2-4 V range. All the spectra are obtained by varying frequency from 1000 kHz to 0.1 Hz. (b) Total impedance of uncycled and cycled (10 cycles, 200 cycles) cells of NMFO (red triangle) and NMFCO (green circle) as a function of negative log of frequency. (c) Equivalent circuit diagram obtained after analysis of impedance spectra of cycled and uncycled NMFCO and NMFO half cells.

.

resistance of sodium ions entering the electrolyte region and the CPE models the capacitive behavior due the formation of the SEI double layer. The impedance Z, of a CPE, is given by $1/Z = Q_0(\omega i)^n$. Here, Q_0 is the analog of capacitance for the CPE with units s^n/Ω, not Farad ($F = s/\Omega$). Here, $n = 0$ describes a pure resistor and $n = 1$ describes an ideal capacitor. The phase of the impedance of a CPE is given by $-(90*n)°$, where $0 \leq n \leq 1$. In table 6, resistances are given in Ω, Q_0 in s^n/Ω, and n is dimensionless. Table 6 shows resistor-CPE values which are obtained after fitting Nyquist plots for cycled and uncycled NMFCO and NMFO cells. We analyzed these

				Resistor-CPE 1			Resistor-CPE 2			Resistor-CPE 3			Z′
	R	Q_0	n	R	Q_0	n	R	Q_0	n	R	Q_0	n	
NMFCO Uncycled	13	--	--	37	$7.1*10^{-5}$	0.78	0	--	--	276	$3.7*10^{-3}$	0.86	242
NMFCO 10 cycles	28	$3.8*10^{-3}$	0.77	100	$6.0*10^{-6}$	0.81	151	$1.8*10^{-5}$	0.85	0	--	--	445
NMFCO 200 cycles	72	--	--	364	$6.1*10^{-6}$	0.73	166	$6.3*10^{-5}$	0.83	888	$2.8*10^{-3}$	0.86	878
NMFO Uncycled	11	--	--	28	$3.3*10^{-5}$	0.66	0	--	--	275	$1.7*10^{-3}$	0.89	279
NMFO 10 cycles	20	--	--	58	$3.0*10^{-5}$	0.64	192	$3.5*10^{-5}$	0.86	517	$2.8*10^{-3}$	0.93	543
NMFO 200 cycles	30	$7.38*10^{-3}$	0.70	98	$6.8*10^{-3}$	0.71	298	$4.6*10^{-5}$	0.83	689	$5.8*10^{-5}$	0.48	1163

Table 6: Values for R, Q_0, and n obtained from fitting. The fit did not yield certain parameters; these entries are left blank. Resistances are given in Ω, Q_0 in s^n/Ω, and n is dimensionless. Z′ is based on the resistance up to the lowest measured frequency. The R values reported for Resistor-CPE loops are, in some cases, extrapolated below the measured frequency.

.

parameters to understand the state of health of cells. The data for uncycled and 10 cycles is from same set of cells. However, the data for 200 cycles is from a separate set of cells. All the uncycled and cycled cells (10 cycles, 200 cycles) were fabricated and cycled in the same way.

Table 7 shows the values of C_{eff} and time constants $\tau = RC_{eff}$ for the resistor-CPE combinations and the separate CPE. We obtained these values by using the equation given by Hsu and Mansfeld, and others, $Z_{(CPE)} = Q_0^{-1}(j\omega)^{-n}$ for a resistor CPE combination where $Q_0C = \tau^n$ and $\tau = RC$. The effective capacitance was given as $C_{eff} = Q_0^{1/n}R^{(1-n)/n}$, with R the fitted value for the resistor-CPE combination (the width of the semicircle) and NMFCO in the uncycled cells [57]–[59].

	Resistor-CPE 1		Resistor-CPE 2		Resistor-CPE 3	
	C_{eff}	τ	C_{eff}	τ	C_{eff}	τ
NMFCO Uncycled	$1.3*10^{-5}$	$4.8*10^{-4}$	--	--	$3.7*10^{-3}$	1.0
NMFCO 10 cycles	$1.1*10^{-6}$	$1.1*10^{-4}$	$6.3*10^{-6}$	$9.5*10^{-4}$	--	--
NMFCO 200 cycles	$6.4*10^{-7}$	$2.3*10^{-4}$	$2.5*10^{-5}$	$4.1*10^{-3}$	$3.2*10^{-3}$	2.9
NMFO Uncycled	$9.0*10^{-7}$	$2.5*10^{-5}$	--	--	$1.5*10^{-3}$	0.41
NMFO 10 cycles	$8.4*10^{-7}$	$4.9*10^{-5}$	$1.6*10^{-5}$	$3.1*10^{-3}$	$2.9*10^{-3}$	1.5
NMFO 200 cycles	$5.8*10^{-3}$	0.57	$1.9*10^{-5}$	$5.7*10^{-3}$	$1.8*10^{-6}$	$1.2*10^{-3}$

Table 7: Values for C_{eff} and τ obtained from the values for R, Q_0, and n in Table 3. The units are R in Ω, C_{eff} in F, and τ in seconds.

After 10 cycles, we observe a mid-frequency semicircle yielding R = 151 Ω in NMFCO, with a near-constant phase when compared with the low-frequency semicircle in the uncycled cell.

.

For NMFO, we observe a mid-frequency semicircle with R = 192 Ω after 10 cycles. In addition, we find a low-frequency semicircle with R = 517 Ω. Both these semicircles for NMFO display a phase nearly equal to that of the low-frequency semicircle of the uncycled cell. We note that the mid- and low-frequency semicircles are about an order of magnitude apart in peak frequency and significantly overlap for the cycled cells with very similar phases. We therefore associate both semicircles with CTK.

Previous authors relate the high-frequency semicircles to SEI layer in Li-ion cathodes. Deng et al. and Nagasubramanian report that the contribution to increase in cell impedance is mostly from the cathode and from anode is negligible [54], [55], [60]–[63]. Also, all our cells were measured under the same conditions and Na anode was used for all our cells. Therefore, we are confident that our comparison of impedance to evaluate cathode performance is meaningful. We characterize resistor-CPE loop 1 as the fit of the high frequency semicircle. For both NMFO and NMFCO, R increases and Q_0 decreases after 10 cycles, with the phase staying almost same. We interpret that this is due to the growth of the SEI layer with cycling.

Charge transfer kinetics (CTK) can give information about accessibility of electrolyte to cathode for motion of ions across its surface. Previous authors report that semicircular features at mid and low frequency region in Nyquist plots can give information charge transfer resistance. The semicircles in the 100-1000 mHz range are above 10 mHz region which is associated with diffusion processes. We observe a semicircle at low frequency which gives R ~ 275 Ω for both uncycled NMFO and NMFCO as shown in Table 6 and Figure 3-20a. We observe that the mid-frequency semicircle yields R = 151 Ω after 10 cycles, with nearly constant phase when compared with the low-frequency semicircle in the uncycled NMFCO cell. We observe a mid-frequency semicircle with R = 192 Ω after 10 cycles and an additional low-frequency semicircle with R =

.

517 Ω for NMFO. We also observe that peak frequency of mid- and low-frequency semicircles is an order of magnitude apart and notably overlap for the cycled cells having similar phases. Therefore, we associate both semicircles with CTK.

Internal resistance Z′ of a cell is generally dominated by CTK. The CTK deteriorates with cycling and leads to an increase in internal resistance of a cell. Table 6 reports the total internal resistance, Z′, which is measured at the lowest measured frequency. We observe from Table 6 and Fig. 3-20(a) that the increase in Z′ for NMFO cells when cycled 200 times is 15% greater than that of NMFCO. Our galvanostatic cycling results shown in Figure 3-18 corroborate this increase in Z′, where we find that the initial slope of the galvanostatic plots, which represents interfacial resistance, increases with cycling. An extrapolation beyond the measured frequency range to complete a semi-circle at lower frequency in NMFO at 200 cycles would lead to a larger resistive component in NMFO in comparison with NMFCO at 200 cycles. Hence, we conclude that performance of NMFCO is better than NMFO at maintaining lower Z′ up to 200 cycles.

The low-frequency impedance is fitted with a Warburg element (a CPE with a phase of 45°, or 0.5 in our units of n). A Warburg impedance element is used to model linear diffusion for which the phase angle is a constant 45° and independent of frequency. We observe that the NMFO impedance fit requires an additional low-frequency resistor-CPE loop after 10 cycles and the NMFCO impedance fit requires an extra CPE (n = 0.77).

We conclude that an SEI layer is formed at the cathode-electrolyte interface for NMFCO. The SEI layer formed has lower resistance and does not deteriorate with cycling. Thus, the low-resistance SEI layer helps form a better contact with the electrolyte and effectively decreases the internal resistance of the battery. We conclude that NMFCO undergoes a small increase in total

.

internal resistance as compared to NMFO when cycled 200 times. Therefore, our analysis shows that NMFCO is a good candidate for sodium-ion batteries.

3.3.7 Conclusions

We synthesized P2-$Na_{0.67}Mn_{0.625}Fe_{0.25}Co_{0.125}O_2$ (NMFCO) cathode with $P6_3/mmc$ phase. We performed crystal structure stabilization, morphology and electrochemical studies on P2-$Na_{0.67}Mn_{0.625}Fe_{0.25}Co_{0.125}O_2$ (NMFCO). Detailed Rietveld analysis of XRD patterns of the NMFCO electrode at different charge and discharge voltages reveals an absence of crystal structure transitions which were observed in NMFO. In particular, we do not observe Z/OP4 phase formation in NMFCO at 4.3 V charge voltage. Our Rietveld analysis of NMFCO discharged to 1.5 V reveals a mixture of two $P6_3/mmc$ phases with unequal in-plane axes. We include an additional observation from our Rietveld fitting results that the additional features in XRD could also be interpreted as the formation of a *Cmcm* phase. We also observe an expansion of the c-axis parameter and a reduction of in-plane axes during cycling. Our impedance analysis shows NMFCO has higher impedance than NMFO. Further, we also observe crack formation in the cathodes after 200 cycles which can be due to intercalation and deintercalation of sodium ions. The crack formation leads to electrolyte depletion and affects the cyclability of cells. Further research work is needed to improve the cathode design to prevent crack formation. Detailed electrochemical impedance analysis reveals that the internal resistance of NMFCO does not increase much with cycling in contrast with NMFO. Therefore, we conclude that $Na_{0.67}Mn_{0.625}Fe_{0.25}Co_{0.125}O_2$ (NMFCO) is the potential candidate for the sodium-ion batteries.

.

Chapter 4. Topological Insulators

4.1 Introduction

Topological insulators have gained enormous interest in the recent years. Topological insulators are materials with insulating bulk and conducting surface or edge states. Topological insulators (TIs) have gapless surface or edge states protected by time reversal symmetry [64]–[68]. They possess gapless surface or edge states with spin momentum locked energy dispersion as shown in Figure 4-1. In a topological insulator, spin–orbit coupling causes an insulating material to acquire protected edge or surface states that are similar in nature to edge states in the quantum Hall effect. The electronic states responsible for this motion are chiral in the sense that they propagate in one direction only along the edge. Electrons moving in +k direction have spins pointing to one direction while those moving in -k have spins pointing in the opposite direction. If there is no time-reversal symmetry breaking mechanism in the material such as sample specific disorders or magnetic fields, the spins cannot be flipped from +k to −k due to spin-momentum locking, i.e. electron back-scattering cannot occur. Topological insulating states have been found in Bi_2Se_3, Sb_2Te_3, and $Bi_{1-x}Sb_x$ [69]–[71]. In the bulk of a non-interacting topological insulator, the electronic band structure resembles an ordinary band insulator, with the Fermi level falling between the conduction and valence bands. On the surface of a topological insulator there are special states that fall within the bulk energy gap and allow metallic conduction on the surface.

4.1.1 The quantum Hall state

The topological insulators are closely related to two-dimensional integer quantum Hall state having edge states [64]. The outer electrons are pinned by their atoms in insulators. An energy

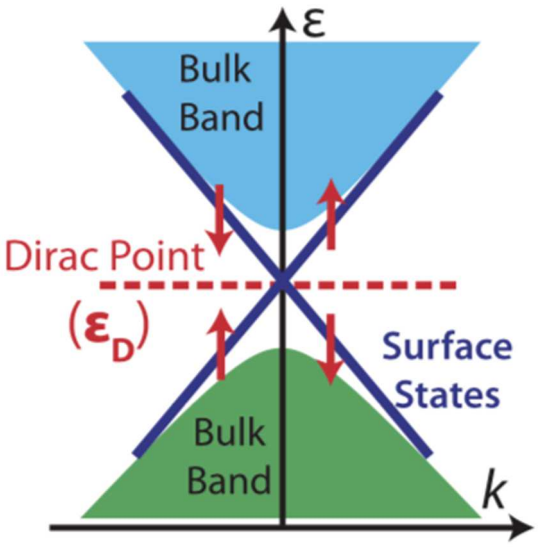

Figure 4-1. Spin momentum locked energy dispersion in topological insulators. Adapted from reference [72].

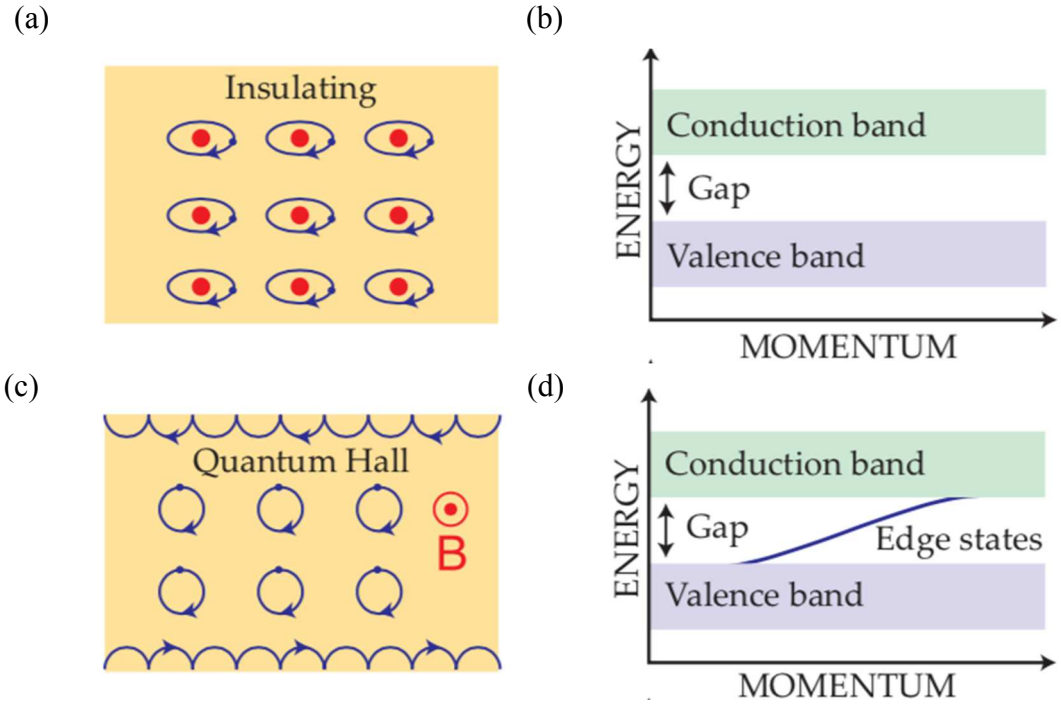

Figure 4-2. (a) An atomic insulator (b) Band structure of an insulator (c) Skipping circular orbits along the edges of sample (d) Edge states crossing band gap in quantum Hall state.

gap is present at all values of momentum as shown in Figure 4-2b and 4-2d. In quantum Hall effect, external magnetic field and low temperature is needed. In the presence of magnetic field, the electrons' circular orbits lead to quantized Landau levels with energy $E_n = (n+1/2)\hbar\omega_c$ where ω_c is the cyclotron frequency. The electrons in the bulk revolve in cyclotron orbits while the electrons near the edges hop in semi-circular orbits along the edges as shown in Figure 4-2c. This results in edge states crossing the bulk energy gap carrying counterpropagating currents of spin up and spin down electrons (Figure 4-2d). The quantized Hall conductivity is given by $\sigma_{xy} = Ne^2/h$, where N is the number of Landau levels. The Hall conductivity is odd with respect to time reversal symmetry. Time reversal symmetry needs to be broken to obtain non-zero total conductance. Due to the presence of magnetic field, the time reversal symmetry is broken in this system.

4.1.2 The quantum spin Hall (QSH) State

A Quantum Spin Hall state was first suggested theoretically by Kane and Mele in graphene [73]. The 2D topological insulator is also known as a quantum spin Hall insulator. QSH is the special case of quantum hall effect without the application of external magnetic field. In this case, spin orbit coupling (SOC) plays an important part and the resulting current on the surface is spin current and not the normal electron current. The up spin moves in one direction while the down spin moves in opposite direction as shown in Figure 4-3a. The QSH state preserves T symmetry and examines its effect on spin 1/2 systems. The chiral motion up and down spins at the edge states have Hall currents that flow in opposite directions in the presence of applied electric field. Therefore, the net Hall conductivity is zero, but there is a non-zero quantized spin Hall conductivity, given as: $J_x^{\uparrow} - J_y^{\downarrow} = \sigma_{xy}^s$ where $\sigma_{xy}^s = e/2\pi$. Figure 4-3b shows the edge states dispersion in quantum spin Hall

state in which opposite spins propagate in opposite directions.

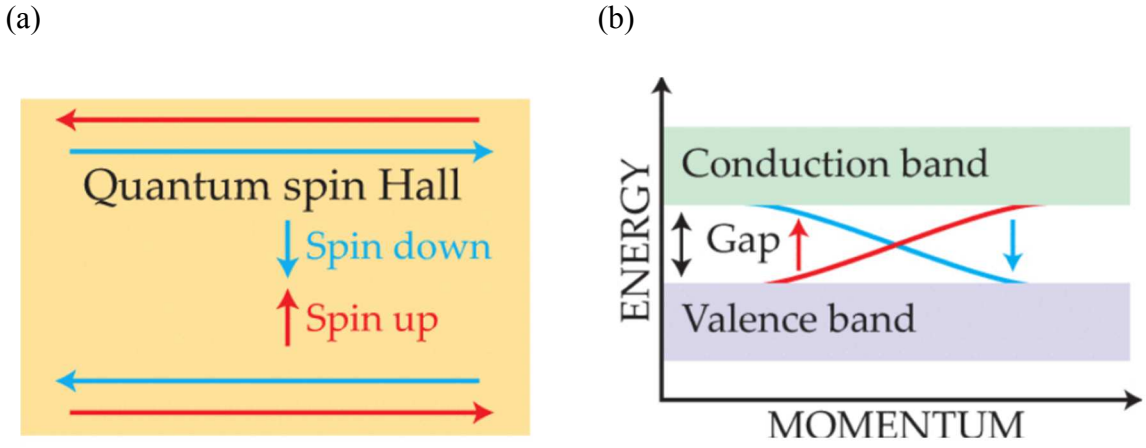

Figure 4-3. (a) Motion of spin up and spin down electrons along the edges in the quantum spin Hall insulator. (b) The edge state dispersion in quantum spin Hall insulators.

4.1.3 Time Reversal Symmetry

Time reversal symmetry is needed to obtain topological states. Time reversal symmetry is represented by anti-unitary operator T, where $T^2 = -1$ for half spin particles. Under time reversal symmetry, t → -t, x → x, p → -p, and $TH(\mathrm{k})T^{-1} = H(\mathrm{-k})$ [74]. Time reversal symmetry is represented by an antiunitary operator $\Theta = \exp(i\pi S_y/\square)K$, where S_y is the spin operator and K is complex conjugation operator. For spin 1/2 electrons, $\Theta^2 = -1$ and anti-unitarity of Θ yields $< u|Tu >= 0$ where $|Tu >$ is a time reversed state. This implies that all eigenstates of a T invariant Hamiltonian are at least twofold degenerate, and the states are orthogonal. This is known as Kramer's theorem.

4.1.4 Topological Number

A material's topological distinctness is determined by a topologically invariant quantity such as the Chern number. To define the Chern number, let us first consider a Bloch Hamiltonian

.

$H(\boldsymbol{k})$ with the crystal momentum k. The eigenstates are given as follows:

$$H(\boldsymbol{k})|u_n(\boldsymbol{k})>= E_n(\boldsymbol{k})|u_n(\boldsymbol{k})> \qquad (4.1)$$

The Berry connection $A^n(\boldsymbol{k})$ which measures the change in wave function in the momentum space is given as:

$$A^n(\boldsymbol{k}) = i<u_n(k)|\partial_k u_n(k)> \qquad (4.2)$$

and the field strength, $F_{ij}^n(\boldsymbol{k})$, is given as:

$$F_{ij}^n(\boldsymbol{k}) = \partial_{k_i} A_{k_j}^{(n)}(k) - \partial_{k_j} A_{k_i}^{(n)}(k) \qquad (4.3)$$

The Chern number of the n[th] band for 2D system is now defined as:

$$Ch_1^{(n)} = \frac{1}{2\pi}\oint dk_x dk_y F_{xy}^n(\boldsymbol{k}), \qquad (4.4)$$

where the integration is performed over whole Brillouin zone. The above integral is non-zero for non-trivial topologies. The Chern number is zero for trivial topologies. The Berry phase, ϕ, is similarly defined as the line integral of $A^n(\boldsymbol{k})$ given as:

$$\phi = \oint dk\, A^n(\boldsymbol{k}) \qquad (4.5)$$

The Berry phase is 0 or 2π for conventional metals and π for non-trivial topologies [75], [76].

4.1.5 Topological Crystalline Insulators (TCIs)

4.1.5.1 TCIs with rotational symmetry

The idea of topological crystalline insulators was first introduced theoretically by Fu et al. [77] Fu et al. considered system with C_4 rotational symmetry and spinless electrons which implies that $\Theta^2 = 1$. Θ^2 should be equal to -1 so that $|n\rangle$ and $\Theta|n\rangle$ are different states with two-fold degeneracy. Therefore, in systems with integer spin, time-reversal symmetry alone does not guarantee topological states. It turns out that a combination of time-reversal symmetry and crystal

.

symmetry leads to topological states in such systems [77], [78]. A system in which topologically protected states result from a combination of time reversal symmetry and crystal symmetry is called a topological crystalline insulator. A TCI cannot be adiabatically deformed to an atomic insulator while preserving certain crystal symmetry. Only some surfaces will support gapless states. Surfaces with low symmetry do not have robust surface states. Consider the Bloch wave functions given as:

$$\left|\psi_n(\boldsymbol{k})\right> = e^{i\boldsymbol{k}.\boldsymbol{r}}\left|u_n(\boldsymbol{k})\right> \qquad (4.6)$$

Together with time-reversal symmetry, the Hamiltonian satisfies the following relations:

$$H(k_x, k_y, k_z) = UH(k_y, -k_x, k_z)U^{-1} \qquad (4.7)$$

and

$$H(\boldsymbol{k}) = \Theta H(-\boldsymbol{k})\Theta^{-1} \qquad (4.8)$$

a doublet gives rise to an effective Kramer's theorem with respect to the operator $\widetilde{\Theta} \equiv U\Theta$, because $\widetilde{\Theta}^2 = -1$ where $U = e^{i\sigma_y \pi/4}$ is the C_4 rotational operator. $\Theta^2 = 1$ for integer spin systems is already mentioned above. The topological nature of a spinless, time-reversal invariant (TRI) insulator with C_4 symmetry can be understood in the following way. There are four C_4-invariant momenta k_i in the three-dimensional (3D) BZ of the system. They are $\Gamma = (0, 0, 0)$, $M = (\pi, \pi, 0)$, $A = (\pi, \pi, \pi)$, and $Z = (0, 0, \pi)$. At these points, $H(k_i)$ commutes with the unitary operator U representing a C_4 rotation. Hence, the energy states at k_i can be chosen to be eigenstates of fourfold rotation with eigenvalues 1, −1, i, and −i. This gives $\widetilde{\Theta}^2 = U\Theta U\Theta = -1$, where we have used that the rotation operator U squares to −1 with eigenvalues ±i. We do not have an effective Kramer's theorem for bands with rotation eigenvalues ±1, because the corresponding rotation operator would square to +1.

.

4.1.5.2 Systems with mirror symmetry

SnTe is a topological crystalline insulator in which topological states are protected by the mirror symmetry. SnTe was theoretically identified as a TCI by Hseih et al. [79] In SnTe, band inversion occurs at high-symmetry L points of the bulk Brillouin zone. Tanaka et al. performed angle-resolved photoemission spectroscopy (ARPES) measurements around $\overline{\mathrm{X}}$ point on the surface Brillouin zone which corresponds to projection of the L point of the bulk Brillouin zone on (001) surface of SnTe [80]. It is at the L points where the direct bulk band gap resides, and the band inversion takes place [80]. Figure 4-4a shows the bulk Brillouin zone of SnTe (red lines) and the corresponding (001) surface Brillouin zone (blue lines). The shaded green plane is (110) mirror plane. Figure 4-4b shows the energy distribution measured along $\overline{\Gamma}\overline{\mathrm{X}}$ direction. The band dispersion along $\overline{\Gamma}\overline{\mathrm{X}}$ cut is linear. The top of this Dirac band touches Fermi energy and is slightly away from the $\overline{\mathrm{X}}$ point. The point where the top of the Dirac band is located is called $\overline{\Lambda}$ point. The band dispersion shows maxima on both sides of the $\overline{\mathrm{X}}$ point, labelled as $\overline{\Lambda}_1$ and $\overline{\Lambda}_2$ for the first and second surface Brillouin zones, respectively. Figure 4-4c shows the ARPES intensity measured at T = 30 K with photon energies 92 eV and 87.5 eV at $\overline{\Lambda}_2$ point.

The topological crystalline insulators are defined by another topological invariant known as mirror Chern number. $M^2 = -1$ for ½ spin electrons. Therefore, the Bloch Hamiltonian decomposes into two blocks with mirror eigenvalues m = +i and m = -i. The mirror Chern number is defined as: $n_{\mathrm{M}} = (n_{+i} + n_{-i})/2$, where n_{+i} and n_{-i} are Chern numbers associated +i and -i eigenstates, respectively [79]. A non-zero mirror Chern number defines a topological crystalline insulator with mirror symmetry.

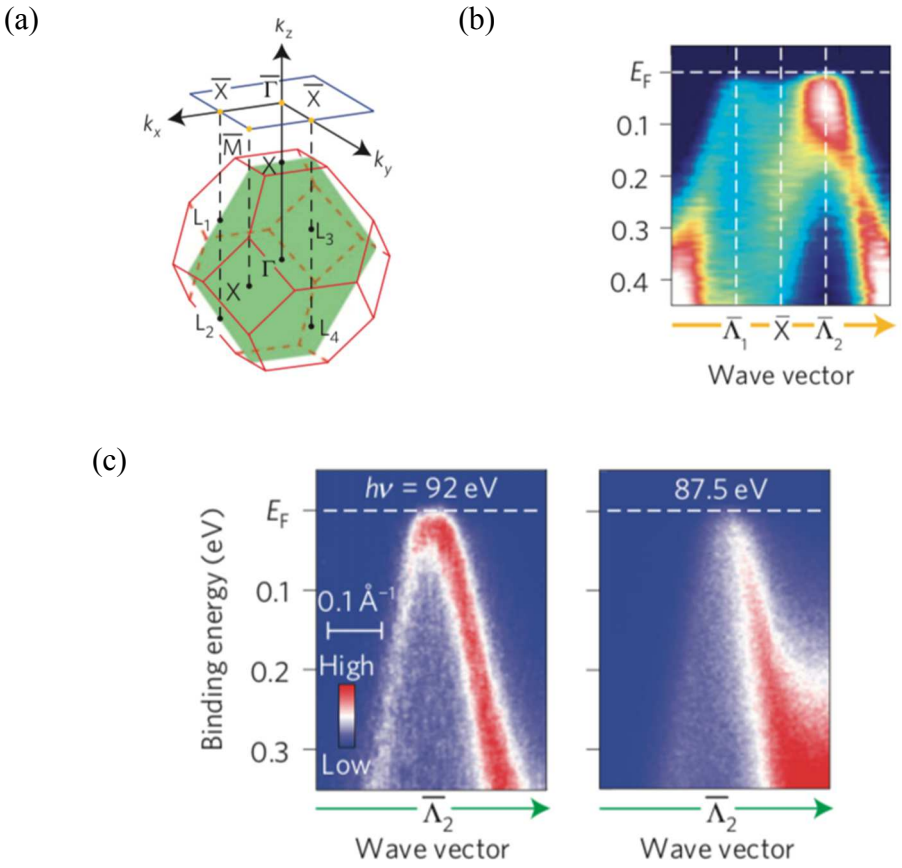

Figure 4-4. (a) The bulk Brillouin zone of SnTe (red lines) and the corresponding (001) surface Brillouin zone (blue lines). The shaded green plane is (001) mirror plane. (b) Energy distribution measured along $\bar{\Gamma}\bar{X}$ direction. (c) ARPES intensity measured at T = 30 K with various photon energies at $\bar{\Lambda}_2$ point. [80]

Similar band dispersion is also observed for $Pb_{1-x}Sn_xTe$ and $Pb_{1-x}Sn_xSe$ [81]–[83]. However, PbTe and PbSe which are isostructural to SnTe don't show Dirac dispersion and are identified as trivial insulators [80]. In $Pb_{1-x}Sn_xTe$, direct band gap is located at the L points in the Brillouin zones, which are the centers of the eight hexagonal faces of the Brillouin zone [82], [84]. The double Dirac-cone surface state is observed for all the $Pb_{1-x}Sn_xTe$ samples with $x \geq 0.3$. In samples with $x < 0.2$, the Dirac-cone surface states are not observed experimentally through ARPES measurements, confirming the occurrence of the topological quantum phase transition at

.

x ~ 0.35. Shubnikov de-Haas oscillations measurements for x lying in between 0 and 0.28 reveal the presence of [111] spheroid shaped Fermi surfaces, confirming that $Pb_{1-x}Sn_xTe$ with x < 0.3 is a trivial insulator [85]. Yan et al. observed Dirac-like surface states on (111) surface of $Pb_{1-x}Sn_xTe$ thin films [86]. Topological surface states are observed in $Pb_{1-x}Sn_xSe$ with x = 0.23 through temperature dependent ARPES measurements which confirm that $Pb_{0.77}Sn_{0.23}Se$ crystal is a TCI. The band-inversion temperature occurs at T_c < 100 K [87]. A topological phase transition from a trivial insulator with gapped surface states to a TCI with Dirac-like metallic surface states is observed below band inversion temperature. $Pb_{0.77}Sn_{0.23}Se$ (001) surface at T = 300 K yield a noninverted band structure and hence no gapless states. Discovery of TCIs has opened a new research branch in the area of topological materials. There might be new TCIs with different lattice symmetries waiting to be discovered.

4.2 Shubnikov-de Haas Oscillations

SdH oscillations are the oscillations observed in the resistivity or conductivity of sample at high magnetic field and low temperatures. At low temperature and high magnetic field, the free electrons behave as quantum oscillators and their motion is quantized. These quantized orbits of electrons are known as Landau levels. Landau levels are degenerate with number of electrons per level directly proportional to the applied magnetic field. If *B* is applied in the z direction, then the vector potential *A* is given as,

$$A = (0, Bx, 0) \qquad (4.9)$$

For an electron in magnetic field,

$$P \rightarrow P + eA \qquad (4.10)$$

The Hamiltonian of an electron can then be expressed as:

.

$$\left(\frac{p_x^2}{2m} + \frac{\left(p_y + eA\right)^2}{2m} + \frac{p_z^2}{2m}\right)\psi = E\psi \quad (4.11)$$

p_x and p_z commute with Hamiltonian. Therefore, they can be replaced by their eigenvalues. Equation (4.11) becomes:

$$\left(\frac{\hbar^2 k_x^2}{2m} + \frac{\left(p_y + eBx\right)^2}{2m} + \frac{\hbar^2 k_z^2}{2m}\right)\psi = E\psi \quad (4.12)$$

Making substitution $E' = E - \frac{\hbar^2 k_z^2}{2m}$ and $x_0 = \frac{-\hbar k_y}{eB}$, Equation (4) becomes

$$\left(\frac{p_x^2}{2m} + \frac{1}{2}m\omega_c^2(x - x_0)^2\right)\psi = E'\psi \qquad (4.13)$$

where $\omega_c^2 = eB/m$. Equation (4.13) has the one-dimensional harmonic oscillator form and gives $E' = \left(n + \frac{1}{2}\right)\hbar\omega_c, n = 0, 1, 2, 3, \ldots$ The Landau level energy is:

$$E = \left(n + \frac{1}{2}\right)\hbar\omega_c + \frac{\hbar^2 k_z^2}{2m} \qquad (4.14)$$

Figure 4-5 and 4-6 shows the formation of Landau levels as magnetic field increases. As magnetic field increases further, the spacing between the Landau levels increase and they start crossing Fermi level. As each Landau energy level passes through the Fermi level, it depopulates as the electrons become free to flow as current. This causes the material's transport properties such as resistivity and conductivity to oscillate periodically. The degeneracy of Landau levels increases, and electrons redistribute among Landau levels to occupy most favorable energy states. As the Landau level crosses Fermi level, the resistance decreases. Once the Landau level is empty, the Fermi level moves from empty Landau level to next filled Landau level and the resistance increases again. This results in oscillations in the resistivity of sample known as SdH oscillations. Conditions to observe SdH oscillations are:

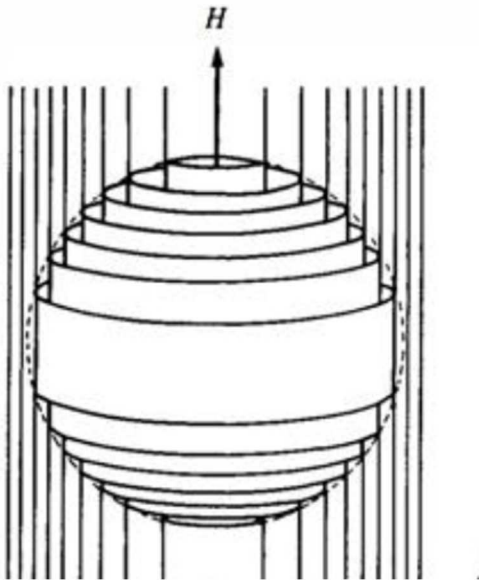

Figure 4-5. Landau tubes for a spherical Fermi surface. Adapted from reference [88].

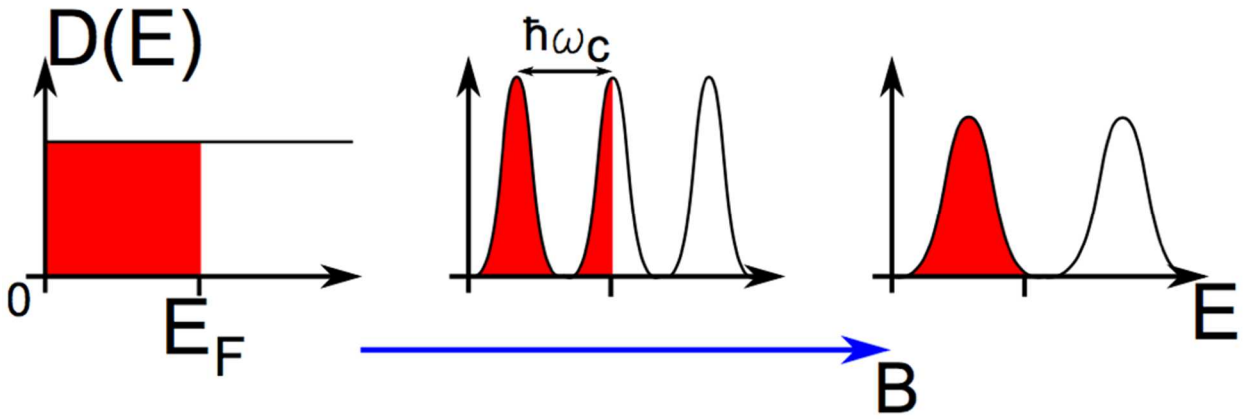

Figure 4-6. Formation of Landau levels and their movement across the Fermi surface in an increasing magnetic field from left to right. Adapted from reference [89].

1) ΔE between two Landau levels is larger than the broadening of the Landau levels due to scattering because of impurities and defects, i.e., $\tau\omega_c \gg 1$, where τ is the scattering time. As B increases, $\hbar\omega_c$ will increase, so that the broadened Landau levels are resolved.

.

2) Small thermal broadening of the Fermi distribution, i.e., $\Delta E = \hbar\omega_c \gg k_B T$. At high temperature, the sharp edge of the Fermi surface distribution, which separates the filled and empty space, smears out and the amplitude of the oscillations will be very low. Hence, the amplitude of the oscillations increases as the temperature decreases.

The Landau level crosses extremal cross section when

$$a_{ext} = \frac{2\pi eB(n + \gamma)}{\hbar}, \qquad (4.15)$$

where a_{ext} is the extremal cross section area in k-space, and γ is a phase correction, typically ½. Equation 4.15 is known as the Onsager relation [90]. The k-space area occupied enclosed by an orbit of allowed energy is quantized and the annular cross section area between two consecutive Landau tubes is given as:

$$\Delta a = \frac{2\pi eB}{\hbar} \qquad (4.16)$$

Thus, the sample's properties will oscillate as B changes, with a period given by [91], [92]:

$$\Delta\left(\frac{1}{B}\right) = \frac{2\pi e}{\hbar a_{ext}} \qquad (4.17)$$

Frequency of oscillations is thus given as:

$$B_F = \frac{\hbar a_{ext}}{2\pi e} \qquad (4.18)$$

SdH oscillations are the tool to measure the Fermi surface shape and topological properties of materials. Four probe resistivity measurements and contactless resistivity measurements are the measurement techniques to measure the SdH oscillations. The magnetic field dependence of SDH oscillation is given as:

$$\Delta\rho = A\cos[2\pi(\frac{B_F}{B} + 0.5 + \beta)], \qquad (4.19)$$

.

where A is the amplitude, B_F is the frequency of SDH oscillations, and $2\pi\beta$ is the Berry phase. The amplitude A has the following temperature dependence given by,

$$A \propto \exp(-\alpha T_D/B)\frac{\frac{2\pi^2 k_B T}{\hbar\omega_c}}{\sin h\left(\frac{2\pi^2 k_B T}{\hbar\omega_c}\right)}, \qquad (4.20)$$

where $\omega_c = eB/m_{eff}$ is the cyclotron frequency ($m_{eff} = m^* m_e$ is the effective mass of the electron, m_e being the mass of a free electron), k_B is the Boltzmann constant, $\hbar$ is the reduced Planck's constant, and $\alpha = 2\pi^2 k_B m_e/e\hbar$ = 14.69 T/K.

4.3 Shubnikov de-Haas Oscillations in Tin Telluride

Overview

In a topological insulator with half-integer spins, spin–orbit coupling causes an insulating material to acquire protected edge or surface states that are similar in nature to edge states in the quantum Hall effect. The surface states are protected by time reversal symmetry [66]. A new class of materials with integer spins that has recently emerged are topological crystalline insulators (TCIs). In TCIs, surface states are protected by point group symmetry of the crystal structure [77]. The combination of time reversal symmetry and mirror symmetry give rise to Kramer's degeneracy in SnTe. SnTe is a topological crystalline insulator having a rock salt crystal structure. The {001}, {110} or {111} surfaces of SnTe which are symmetric about {110} mirror plane possess gapless surface states. It is predicted theoretically by Fu et al that all {001} planes with C_4 rotational symmetry will show Dirac bands [77]. The Dirac states in SnTe have quadratic dispersion whereas the Dirac states possess linear dispersion in conventional topological insulators. The topological states are observed by Tanaka et al. from ARPES measurements on the

.

(001) and (111) SnTe surface [80]. The study of SdH and de Haas–van Alphen effect (dHvA) oscillations study by Dybko et al. shows a quadratic frequency dispersion that correlates to the presence of a cylindrical Fermi surface and indicates the presence of topological states on the (001) and (010) surfaces of SnTe [93]. Magnetoresistance studies on (111) SnTe thin films reveal the presence of a two-dimensional Fermi surface [94]. Tanaka et al. report the presence of Dirac states on (111) surface of SnTe, confirmed through their ARPES measurements [95]. Wang et al. theoretically predict the presence of surface states on the (111) surface of SnTe [96].

In this chapter, we present the study of the angle dependent Shubnikov De-Haas (SdH) oscillations on (001) surface of SnTe. We observe SdH oscillations at high magnetic field and low temperature. Our results suggest the presence of topological surface states, in agreement with experimental studies on other surfaces and on the theoretical calculations of Fu et al [77]. We also use variable-angle and variable-temperature measurements to characterize the Fermi surface and report the Dingle temperature, Fermi velocity, and other physical parameters for this surface.

4.3.1 Crystal Growth

In order to study the properties of SnTe, high-quality single crystals are synthesized. The growth of single crystals is essential for the study of crystal properties as it ensures sample homogeneity. Inhomogeneity in sample results in defects and affects crystal quality. To form good contacts using gold wire for transport measurements, large crystals are needed. Thus, the growth of large single crystals is a great advantage in the characterization of many material properties.

SnTe single crystals were grown by a self-flux method. A starting ratio of Sn/Te = 51:49 was chosen to synthesize SnTe single crystals having minimum Sn vacancy. The process was successful, and yielded crystals with low bulk carrier concentration as compared with other recent reports. The elements Sn (99.999 % Alfa Aesar) and Te (99.999% Alfa Aesar) were mixed together

.

and sealed in the evacuated quartz ampoule inside the glove box in ultra-high purity argon environment. The pressure inside the evacuated ampoule was 10 millitorr. The ampoule was placed vertically inside a Lindberg box furnace in ceramic boat supported by quartz wool. The ampoule was heated to 900°C at 5°C/min and kept at 900°C for 3 days. The ampoule was then slowly cooled to 550°C at 0.6°C/hr. The samples were then annealed at 500°C for 2 days. The ampoule was then cooled to room temperature at rate 1.8°C/hr. Nice flat crystals were obtained. Crystals were stored inside a sealed and evacuated pyrex glass tube before performing measurements. Figure 4-7 shows the binary phase diagram of Sn-Te system [97].

4.3.2 Magnetoresistance measurements on SnTe

X-Ray diffraction measurements and Rietveld analysis were performed to confirm the crystal structure of air protected SnTe samples. Figure 4-8a shows the powder X-ray diffraction data for SnTe at room temperature. Nickel filter was used to filter K_β radiation. SnTe crystallizes in rocksalt/cubic structure (space group $Fm\bar{3}m$), confirmed by Rietveld analysis of XRD diffractogram. All the diffraction peaks observed were fitted well with the space group $Fm\bar{3}m$.
The morphological quality of our crystal surfaces was examined under a Scanning Electron Microscope (SEM). Stoichiometric ratios of elements in the crystal were determined by Energy Dispersive X-ray Analysis inside the SEM. To more directly observe properties of the Fermi surface of SnTe, investigations were carried out via magnetoresistance measurements of SdH oscillations. SdH oscillations that arise from Landau level quantization help in resolving the Fermi surface shape and in exploring the electronic properties of materials. We performed angle dependent magnetoresistance measurements on pure SnTe samples at low temperatures and higher magnetic field. Resistivity measurements were performed using standard four-probe ac technique

and the electrical contacts were made using gold wires using silver paste on the (001) plane (shiny and flat surface) of SnTe. Figure 4-8b shows the XRD rocking curve around (200) peak. The presence of sharp (200) peak indicates crystalline (001) plane. The full width half maximum (FWHM) of the Cu-Kα peak in Figure 4-8b is 0.024° which indicates high crystal quality.

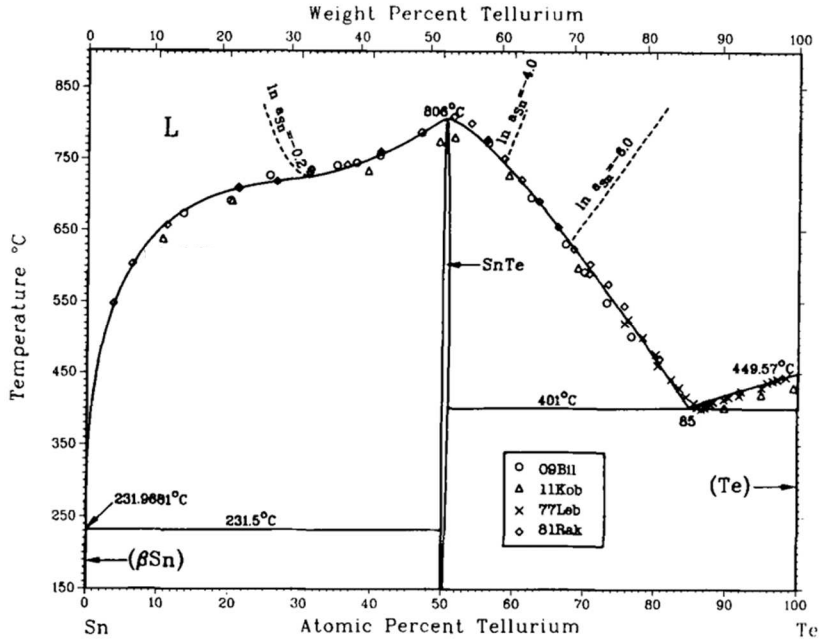

Figure 4-7. Phase diagram of Sn-Te binary system [97].

4.3.3 Results and discussion

Figure 4-9a shows the results of the Hall resistivity measurement performed on SnTe sample. We should note here that physical limitations in the placing of resistivity probes on a small crystal surface can lead to an unavoidable mix of ρ_{xx} and ρ_{xy} components in measured values. A linear fit to the Hall voltage versus magnetic field above 1 Tesla yields a bulk charge carrier concentration of n = 0.8 $*10^{20}$ cm^{-3}. As shown in Table 8, our value for the bulk charge concentration is at the lower end of that reported by previous authors [80], [93], [98], [99]. As is clear from Hall measurements, our SnTe crystal is p-type in nature, indicating continued presence

.

of Sn vacancies in spite of the slight excess of Sn used during growth (we used a ratio of 51:49 of Sn:Te), but with relatively low carrier concentration [99]. Such Sn vacancies introduce holes [80]. As is clear from Hall measurements, our SnTe crystal is p-type in nature, indicating continued presence of Sn vacancies in spite of the slight excess of Sn used during growth (we used a ratio of 51:49 of Sn:Te), but with relatively low carrier concentration [80]. Oscillations periodic in $1/B$ are observed at higher magnetic fields in ρ_{xy} as magnetic field varies. The angle dependence of the frequency of SdH oscillations gives useful information about the shape and size of the Fermi surface. The shape of Fermi surface indicates whether the conduction is from bulk or surface states. The bulk states will have ellipsoidal Fermi surface while the surface states will have cylindrical Fermi surface. Figure 4-9b shows the SdH oscillations obtained after background subtraction at

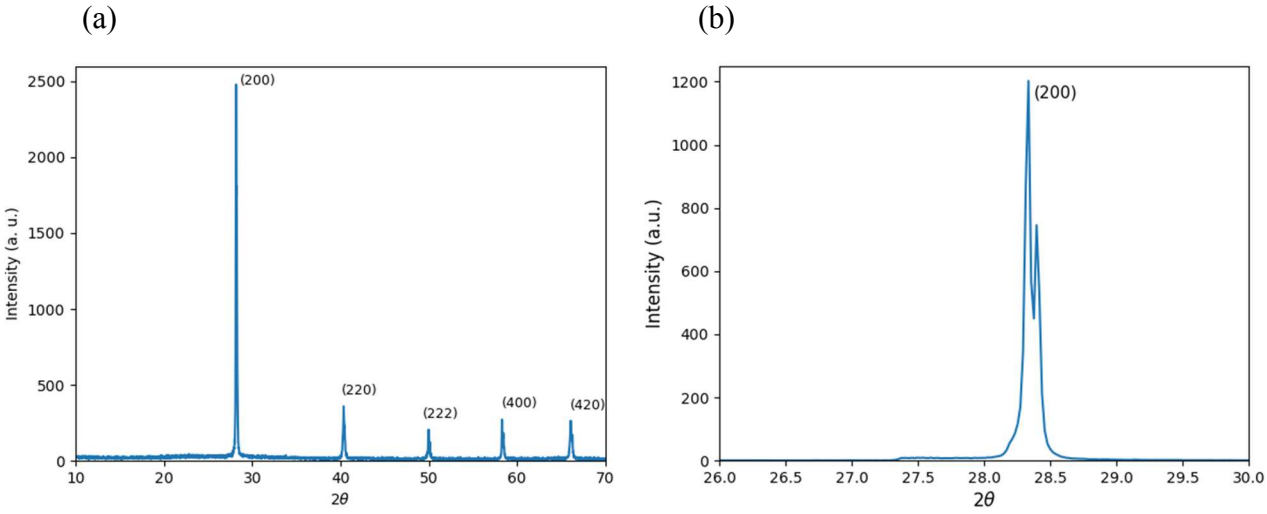

Figure 4-8. (a) Powder X-Ray diffractogram of SnTe (b) XRD rocking curve around (200) peak.

different tilt angles at 0.35 K. Here, the tilt angle is the angle between sample's c-axis and magnetic field, i.e., θ is zero when magnetic field is perpendicular to sample's surface and 90° when the magnetic field is parallel to the sample's surface. Although we performed measurements at different angles up to 75°, we did not observe SdH oscillations above 30°. Based on the onset field

.

and amplitude when compared with other angles, we do not believe that the changes in slope at high field in the 45° and 60° measurements represent an onset of quantum oscillations. The frequency of oscillations was obtained after background subtraction from the resistance curves and fitting the oscillations with SdH oscillation equation (Equation 4.19). Table 9 shows the frequency of SdH oscillations at different angles and temperatures obtained after background subtraction and fitting the oscillations with the SdH oscillation equation at different angles and temperatures. Figure 4-10 shows the angular dependence of the SdH oscillation frequency for SnTe sample at 0.35 K. The frequency of oscillations appear to follow the relation $f \propto 1/\cos(\theta)$, possibly due to a cylindrical Fermi surface. The Berry phase obtained after fitting SdH oscillation equation is nearly equal to π, leading us to believe that the oscillations arise from topological surface states. The value of Berry phase is equal to π for the topological surface states and 0 for conventional metals [76]. The presence of cylindrical Fermi surface and Berry phase equal to π indicates the possible presence of topological surface states on (001) surface.

We also observe that the amplitude of quantum oscillations decreases with increase in temperature. The oscillations are not resolvable above 4 K. The oscillations have a single frequency nearly equal to 232 T at 0°, independent of temperature. The amplitude of the oscillations is plotted at fixed magnetic field for different temperatures, and the effective cyclotron mass is obtained by fitting amplitude dependence, *A*, on temperature given by $A \propto \frac{\frac{2\pi^2 k_B T}{\hbar\omega_c}}{\sin h\left(\frac{2\pi^2 k_B T}{\hbar\omega_c}\right)}$ as shown in Figure 4-11a. Here, $\omega_c = eB/m_{eff}$ is the cyclotron frequency, k_B is the Boltzmann constant, $\hbar$ is the reduced Planck's constant, and $m_{eff} = m^* m_e$ is the effective mass of the electron, where m_e is the mass of a free electron. The effective mass obtained is m_{eff} ~ 0.21 m_e on the (100) surface being studied by us, in contrast with m_{eff} ~ 0.08 m_e obtained by

.

Dybko et al. on the (001) surface and $m_{eff} \sim 0.094\ m_e$ by Savage et al. [93], [98] Further analysis of the quantum oscillation amplitude damping yields the mean-free path and scattering time of the samples. Figure 4-11b shows the Dingle plot which is equal to the slope obtained after fitting the straight line in the plot of ln(D) versus 1/B at different temperatures, where $D = \Delta\rho B \sinh(2\pi^2 K_B T/\hbar\omega_c)$. The Dingle temperature T_D calculated from the slope is 12.0 K and is constant irrespective of temperature and angle. The scattering time $\tau_S = \hbar/2\pi k_B T_D$, extracted using Dingle temperature is found to be 2.1×10^{-14} s. Using Onsager equation: $F_s = \hbar A/2\pi e$, one obtains the Fermi wave vector, $k_F = 8.46 \times 10^8$ m^{-1}. The Fermi velocity, $v_F = \hbar k/m_{eff}$, obtained is 4.9×10^5 m/s. In fermionic systems, the Dirac velocity is equal to the Fermi velocity. ARPES studies by Tanaka et al. have found the Dirac velocity $v_D = 4.56 \times 10^5$ m/s for the right-hand branch and 6.84×10^5 m/s for the left-hand branch when performing a linear extrapolation on the dispersion branches used to find the Dirac point [80]. We see that our value agrees well with the right-hand branch, as does the value of Dybko et al. [93]. The reason that we observe the right branch of the Dirac cone here could be related with the presence of high density of states, as also observed by Tanaka el al. in their ARPES measurements on (001) surface [80]. From the frequency of SdH oscillations, we obtain $n_{2D} = 5.7 \times 10^{12}$ cm^{-2}. It is predicted theoretically by Hsieh et al. that all {001} planes with mirror symmetry will show Dirac bands [79]. The fact that we are seeing cylindrical Fermi surface, and our values for transport-related constants using the (001) surface are in good agreement with those obtained by Dybko et al. and Tanaka et al. on the (001) surface, corroborates this prediction of Fu [77], [80], [93].

.

		Garg et al. [this work]	**Dybko et al.** [ref 16]	**Savage et al.** [ref 19]		**Tanaka et al.** [ref 14]	**Burke et al.** [ref 18]
Technique used			SdH oscillations	SdH oscillations	SdH oscillations	ARPES	SdH oscillations
Surface studied		(001)	(001)	(001)	(100)	(001)	(001)
Bulk carrier concentration		n_D (cm^{-3})	0.8 x 10^{20}	1.4 x 10^{20}	0.72 x10^{20} – 8.0 x 10^{20}	2.0 x 10^{20}	0.9 x 10^{20}
Fermi wave vector		k_F (m^{-1})	8.46 × 10^8	2.7 × 10^8			
Fermi velocity		v_F (m/s)	4.9 × 10^5	4.0 × 10^5		4.56 × 10^5 and 6.84× 10^5	
Berry Phase (2π)		Units of 2π	~ 0.5	~ 0.5			
Effective electron Mass		m_{eff}	0.2 m_e	0.08 m_e	0.094 m_e		
Dingle Temperature		T_D (K)	12		17.3		
Frequency of quantum oscillations		f (T)	~230	~25	~200		
Surface carrier concentration (2D)		N_s (n_{2D}) (cm^{-2})	5.7 x10^{12}	6.2 x 10^{11}			

Table 8. Comparison of various parameters measured experimentally at different surfaces of SnTe by us and other authors

(a)

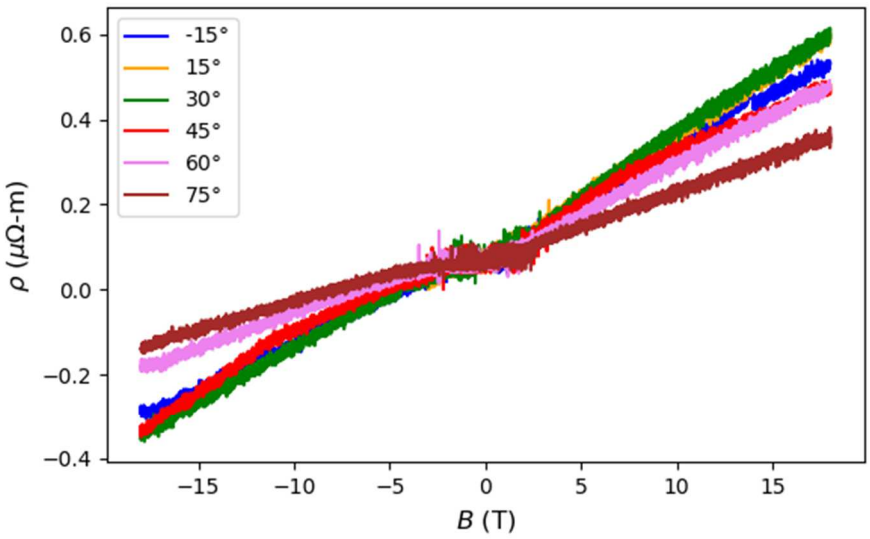

(b)

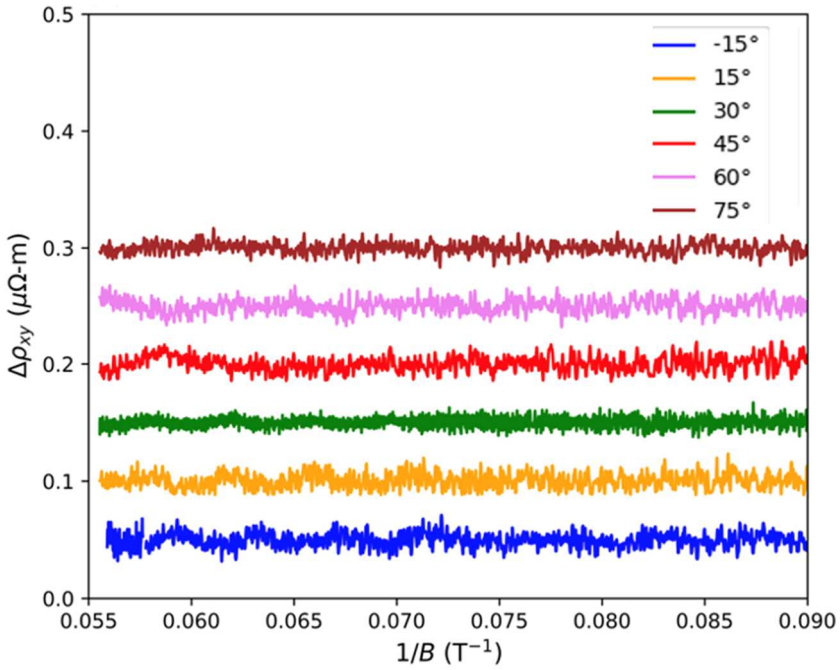

Figure 4-9. (a) ρ_{xy} vs magnetic field at different angles at 0.35 K (b) Shubnikov-de Haas oscillations in sample SnTe with varying magnetic field at 0.35 K and different angles, obtained after subtracting background. Data collected at 45, 60, and 75 degrees do not show oscillations.

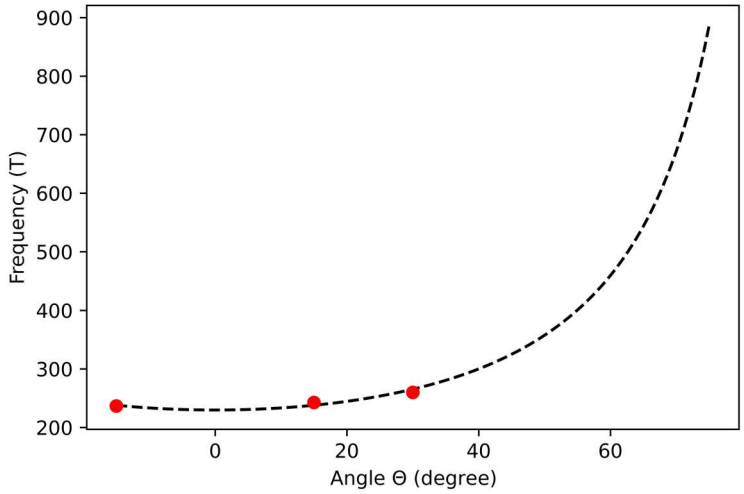

Figure 4-10. Angular dependence of the SdH oscillation frequency for SnTe sample at 0.35 K. Solid red curve corresponds to the cylindrical fit ($f \propto 1/\cos(\theta)$ for the Fermi surface and blue points correspond to the frequencies obtained after fitting SdH oscillation equation.

Temperature (K)	**Angle (Degree)**	**SdH Oscillations Frequency (T) ± 2 T**	**Berry Phase (Units of 2π) ± 0.1π**
0.35	-15	236	0.44
0.35	15	243	0.46
0.35	30	260	0.38
1.0	-15	232	0.45
4.0	-15	231	0.53

Table 9. Frequency of SdH oscillations obtained at different temperatures and angles in SnTe sample.

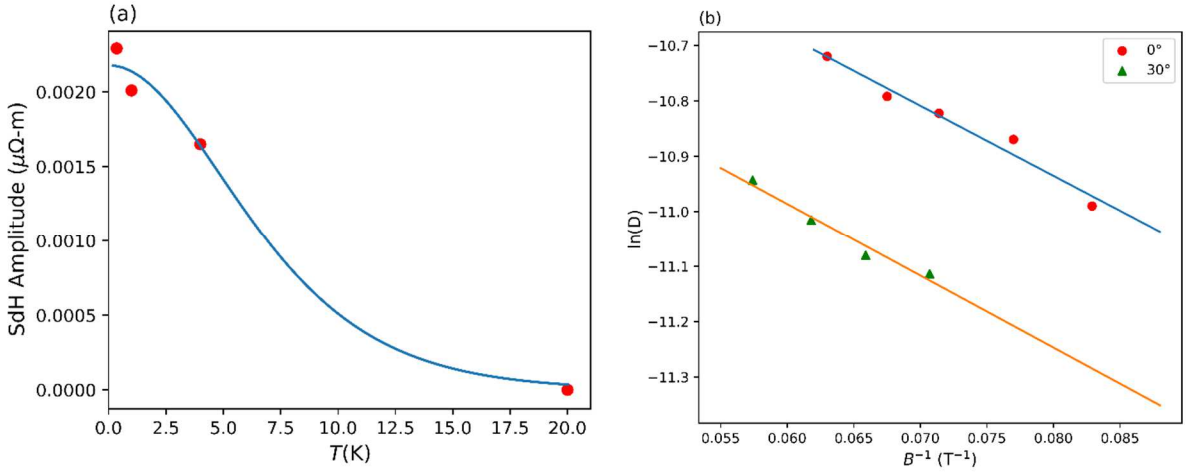

Figure 4-11. (a) Temperature dependence of the amplitude of SdH oscillations (b) ln(D) plotted as a function of 1/B.

4.3.4 Conclusions

In summary, we performed transport measurements to study the Fermi surface of SnTe crystals. The magneto-transport measurements on the (001) surface of our SnTe single crystals exhibit SdH oscillations above 6 T at temperatures below 4 K. The analysis of SdH oscillations in resistivity yields a Berry phase equal to π. The angle dependence of oscillations' frequency reveals a cylindrical Fermi surface. The frequencies that we find are higher than those found by Dybko et al, but are in closer agreement to those found by Savage et al. [93], [98] The Berry phase of π, combined with the presence of a cylindrical Fermi surface indicates the possible presence of topological surface states. Our results on the (001) surface support the presence of topological states found on other surfaces by other researchers, such as Tanaka et al, and Dybko et al. [80], [93] We also find that the Fermi velocity of electrons in the right branch is 4.9×10^5 m/s which agrees with previous authors Dybko et al. and Tanaka et al. [80], [93] Our findings support the idea

.

that (001) surface of SnTe has topological states that are protected by mirror and time-reversal symmetry.

4.4 Fermi Surface of Antimony Selenide

TIs such as Bi_2Se_3 and Bi_2Te_3 have been theoretically and experimentally shown to possess topological properties at ambient pressure and become superconducting under pressure or charge doping [100]–[104]. All these TIs have a Dirac cone at Γ point and a rhombohedral structure (*R*-3*m*). In contrast, Sb_2Se_3 is a band insulator at normal temperature and pressure. While Sb_2Se_3 has also been predicted to exhibit a topological phase transition under pressure, these predictions have all been performed using a rhombohedral crystal structure (*R*-3*m*) which has not been observed in Sb_2Se_3, even under high pressure [105], [106]. To the best of our knowledge, no theoretical evidence has been found for the existence of a topological phase in the orthorhombic (*Pnma*) crystal structure of Sb_2Se_3.

Structural, superconducting and topological phase transitions have been studied in numerous topological insulators under pressure such as Bi_2Se_3, Sb_2Te_3, Sb_2S_3, and Bi_2Te_3 [100]–[102], [107]. High pressure allows the modification of the physical properties of materials as it decreases interatomic distances. Antimony Selenide (Sb_2Se_3) is a band gap insulator with a 1 eV bandgap at ambient pressure which becomes metallic above 3 GPa and superconducting above 10 GPa [105], [108], [109]. This material is expected to exhibit strong spin-orbit coupling, but with a different crystal structure than similar A_2B_3 type compounds such as Sb_2Te_3 and Bi_2Se_3. Wei et al. predicted the topological phase transition occurring at the critical value $P_c \simeq 1.0$ GPa [106]. The bulk energy gap closes at the topological phase transition and reopens above P_c. The conduction and valence bands cross at a pressure above P_c which leads to band inversion at the time reversal invariant k point in the Brillouin Zone (BZ). In this chapter, we report studies of Shubnikov-de

.

Haas oscillations as a function of pressure and magnetic field orientation on single crystals of antimony selenide. Our single crystals are orthorhombic, unlike rhombohedral Bi_2Se_3 and Sb_2Te_3. Following up on the previous collaborative studies of Raman spectroscopy and first principles DFT in the paper by Bera et al. (a collaborative paper with members of our research group), which revealed an electronic topological transition (ETT) with pressure, we performed non-contact conductivity measurements using a tunnel diode oscillator (TDO) circuit under high pressure in a diamond anvil cell [105]. A Fermi Surface (FS) is found to appear at 6.4 GPa which indicates that Sb_2Se_3 possibly undergoes insulator to metal transition as evidenced by SdH oscillations observed at 6.4 GPa. The Fermi surface is quasi-cylindrical with axis perpendicular to the b-axis, i.e., in a-c plane of the crystal. Furthermore, a Berry phase (β) nearly equal to π has been measured independent of magnetic field rotation angle. These measurements provide evidence for a possible new category of topologically non-trivial insulators beyond Bi_2Se_3 related structures.

4.4.1 Crystal Growth

Sb_2Se_3 crystals were synthesized using self-flux growth method. Stoichiometric ratios of Sb (99.99% Alfa Aesar) and Se (99.99% Alfa Aesar) elements were mixed in the argon atmosphere inside the glove box and sealed in an evacuated quartz ampoule. The ampoule was placed inside the single zone furnace with temperature gradient, and the furnace was heated to 675°C. After 12 hours, the sample was allowed to cool to 615°C relatively fast, and then cooled to 460°C at 0.1°C/min. The furnace was then cooled to room temperature at fast rate. Figure 4-12 shows the binary phase diagram of Sb_2Se_3 [110]. Small sized crystals were obtained (Figure 4-13a). XRD pattern of the powdered sample shown in Figure 4-13b was obtained using Bruker X-Ray Diffractometer with Cu-Kα radiation. We confirmed through Rietveld analysis of X-Ray

.

diffraction data that Sb_2Se_3 has orthorhombic (*Pnma*) crystal structure with crystal axis a =11.7 Å, b = 3.97 Å, and c = 11.62 Å at ambient pressure and temperature. Sb_2Se_3 cleaves perpendicular to b axis, i.e. along a-c plane. Figure 4-13c shows the unit cell of Sb_2Se_3 and Figure 4-13d shows [001] directional view of the crystal structure showing the cleavage plane perpendicular to the b direction.

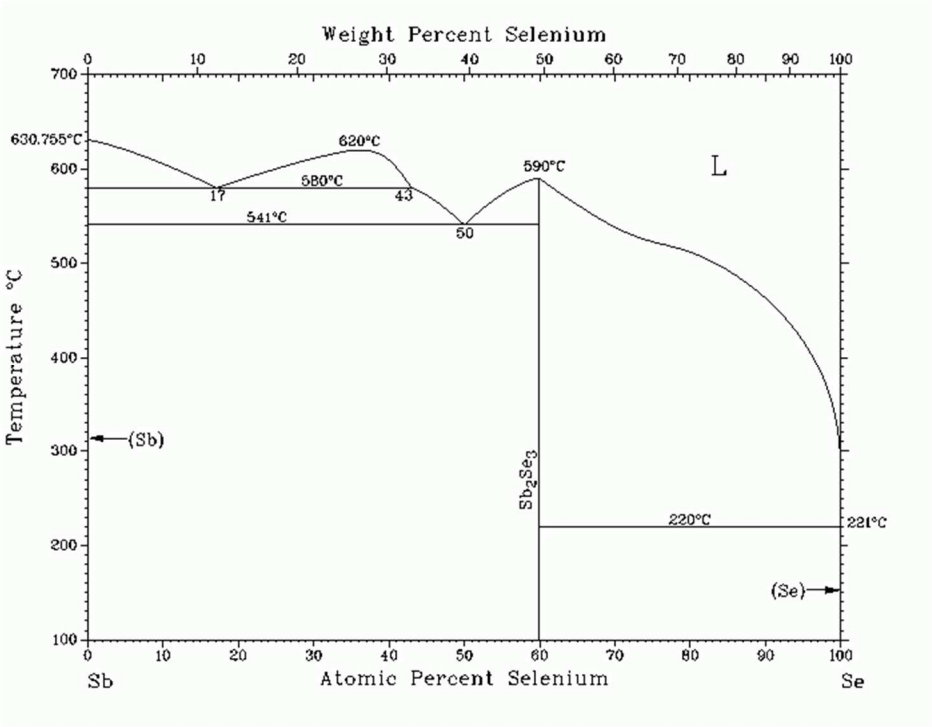

Figure 4-12. Sb-Se binary phase diagram [110]

4.4.2 Contactless Resistivity Measurements

Contactless resistivity measurements were performed inside the diamond anvil cell (DAC). A sample of typical dimensions 100 µm x 100 µm x 30 µm was cleaved and loaded inside the DAC made of plastic turnbuckle. The diameter of the diamond anvil was 600 µm. The pressure-transmitting medium used was the mixture of methanol and ethanol with ratio 4:1. Copper gasket

.

with thickness 60 μm was used to contain the medium, and the center hole of 200 μm diameter was drilled. Pressure inside the cell was measured using ruby luminescence technique. Ruby spheres placed at the top of sample served as a pressure marker. The inductance coil made of insulated copper wire surrounded the sample. The range of our pressure study was from 1 atm to 6.4 GPa. The resonance frequency of the tunnel diode oscillator, $f = 1/\sqrt{LC}$, where L is the inductance of the coil surrounding the sample and C is the capacitance of the circuit, is typically in megahertz range. The tunnel diode oscillator (TDO) frequency is sensitive to the resistivity of the sample. Interaction of the sample with the inductance of the coil causes a shift, $\Delta f/f = -G\ \Delta\delta/\delta$, in the resonant frequency, where G is a geometric factor and δ is the skin depth. δ is related to the resistivity of the sample as $\delta = \sqrt{\rho/\pi\mu_o f}$, where ρ is the resistivity of sample, and μ_o is the magnetic permeability of free space. While rotating the magnetic field, we have considered θ to be the angle between the magnetic field and the normal to the sample's plane.

4.4.3 Results

As previously mentioned, Sb_2Se_3 is a band insulator with indirect energy gap equal to 1 eV and with resistivity nearly equal to 10^6-10^8 Ω-m at ambient pressure and temperature [111]–[113]. We performed TDO measurements at atmospheric pressure and 6.4 GPa at different angles and temperatures. The crystal on which measurement was performed at atmospheric pressure was different from the one on which measurement was performed at 6.4 GPa. Figure 4-14 shows the frequency versus magnetic field measurements for different angles and temperatures at 6.4 GPa on sample 1 and atmospheric pressure on sample 2. Oscillations were not observed at ambient pressure at any angle and temperature after the subtraction of fourth order polynomial background as well as differentiation of the signal as shown in Figure 4-15. However, oscillations were

observed at 6.4 GPa after the topological transition at higher field on sample 1. We found that oscillations at higher

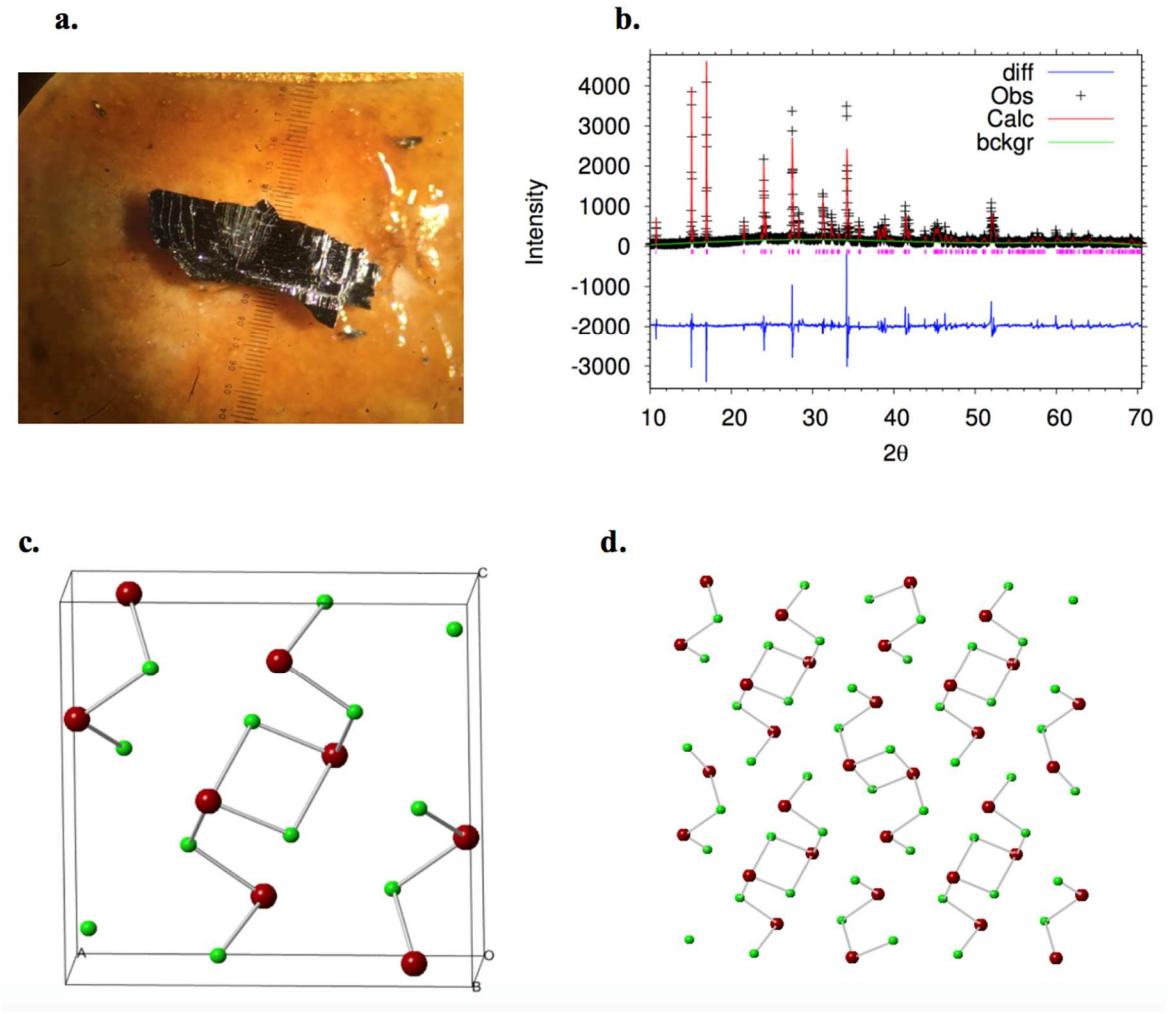

Figure 4-13. (a) Sb_2Se_3 obtained after synthesis using self-flux growth method. (b) Powder X-ray diffraction of the crystals using Bruker X-Ray diffractometer with Cu-Kα radiation. (c) Unit cell of Sb_2Se_3 (Red spheres are Sb atoms and green spheres are Se atoms. (d) [001] directional view of the crystal structure showing the cleavage plane perpendicular to the b direction

.

magnetic field are periodic in 1/*B,* indicating that these are Shubnikov–de Haas (SdH) oscillations. The oscillations were obtained after the polynomial background subtraction as well as through the differentiation of the signal at fields 12 T < B < 18 T as shown in Figure 4-16 and 4-17. SdH oscillations are observed at higher magnetic field due to the quantization of electron orbits in the presence of magnetic field.

4.4.3.1 Frequency of SdH oscillations, *F*, and the Fermi surface

The frequency of SdH oscillations was obtained by fitting SdH oscillation equation (Equation (4.19)). At higher angles (45° ≤ θ ≤ 90°), since the frequency of oscillations increases with angle and becomes constant as angle approaches 90°, we conclude that the Fermi surface is bulging outwards elliptically perpendicular to the surface of the crystal. Figure 4-18a shows the angular dependence of frequencies of oscillations at 0.7 K. The solid black curve is the ellipsoidal fit to the angular dependency of the frequency and the shaded region (0° ≤ θ ≤ 30°) is the region where oscillations are not observed. For an elliptical surface, the frequency of oscillations varies as

$$F(\theta) = F_o \left[\cos^2(\theta) + \left(\frac{k_F^x}{k_F^y}\right)^2 \sin^2(\theta)\right]^{-\frac{1}{2}}, \quad (4.21)$$

where F_o is the frequency at $\theta = 45^\circ$ and k_F^x/k_F^y is the measure of the eccentricity of the surface that is bulging out elliptically. At lower angles (0°, 15°, 30°), we did not observe oscillations at higher range of magnetic field after the subtraction of background as well as differentiation of the signal. This implies the presence of quasi-cylindrical Fermi surface whose axis is perpendicular to b-axis of the crystal, shown in Figure 4-18b. This indicates that conduction is from surface states.

.

Berry phase obtained after fitting the SDH oscillation equation (Equation (4.19)) is nearly equal to π. Berry phase obtained at different temperatures and angles is shown in Table 10. As a reminder, Berry phase is 0 for conventional metals and π for the Dirac systems [76]. The observation of quasi-cylindrical Fermi surface and π Berry phase is an indicator of the possible presence of non-trivial topology at high pressure.

4.4.3.2. Amplitude of SdH Oscillations

We observed decrease in amplitude of SdH oscillation frequency with increasing temperature. Oscillations were not resolvable at T = 6.8 K or higher. The amplitude of the oscillations is plotted at fixed magnetic field for different temperatures, and the effective cyclotron mass is obtained by fitting Equation (4.20) as shown in Figure 4-19. The effective mass was calculated as $m_{eff} \sim 1.19\ m_e \pm 0.05\ m_e$. The Dingle temperature, T_D, which is a measure of

Temperature (K)	Angle	Frequency (Tesla)	Berry Phase (Units of 2π)
0.4	45º	72	0.62
0.7	90º	110.2	0.45
0.7	75º	107.22	0.51
0.7	60º	93.7	0.4
0.7	45º	69.7	0.4
1.3	90º	114.6	0.47
1.3	75º	106.5	0.48
1.3	45º	68.71	0.5

Table 10. SDH Oscillations at T = 0.7 K, 1.3 K and P = 6.4 GPa at different angles.

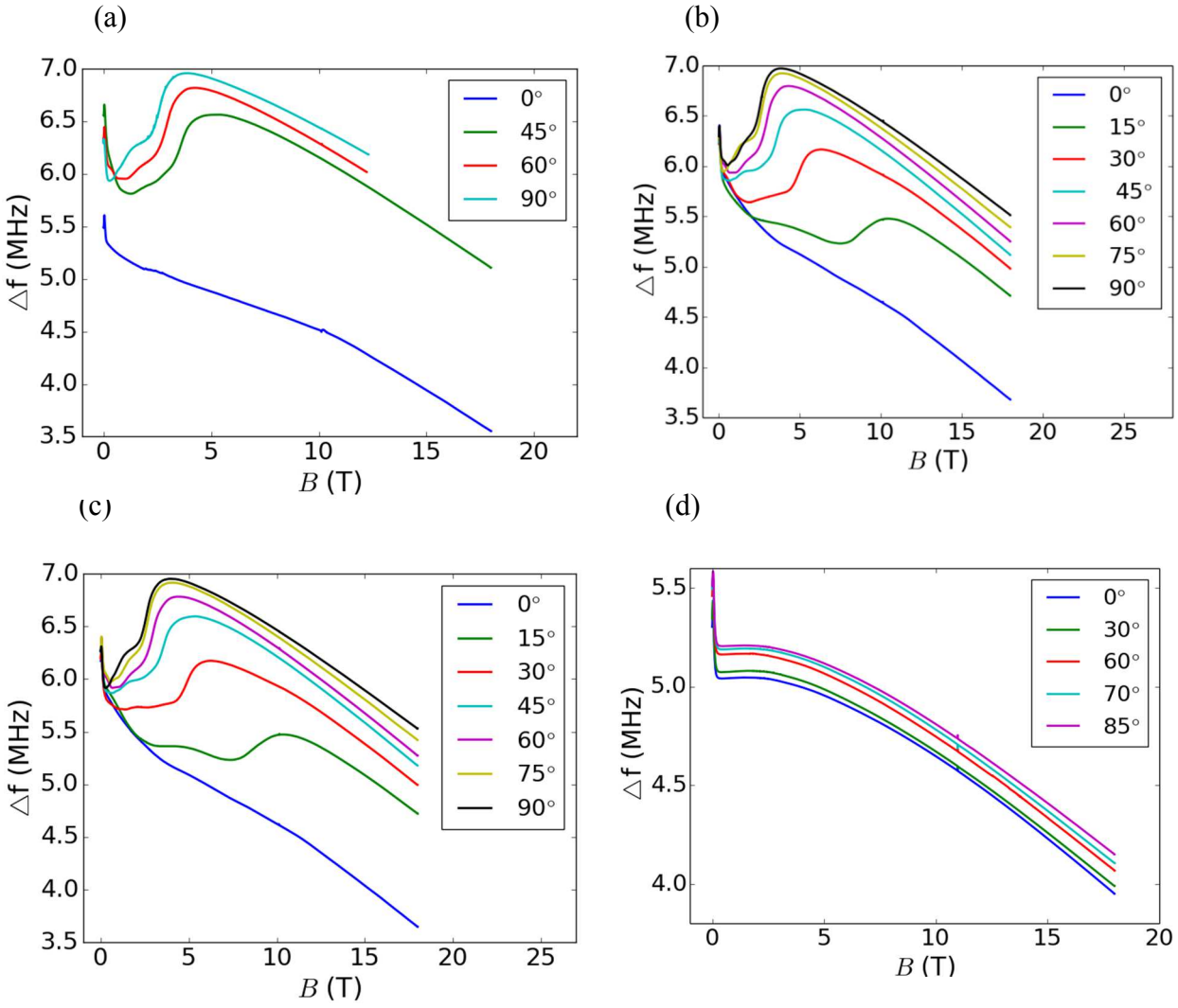

Figure 4-14. TDO frequency versus magnetic field at (a) P = 6.4 GPa, T = 0.4 K (b) P = 6.4 GPa, T = 0.7 K (c) P = 6.4 GPa, T = 1.3 K (d) P = 1 atm, T = 0.4 K at different angles.

.

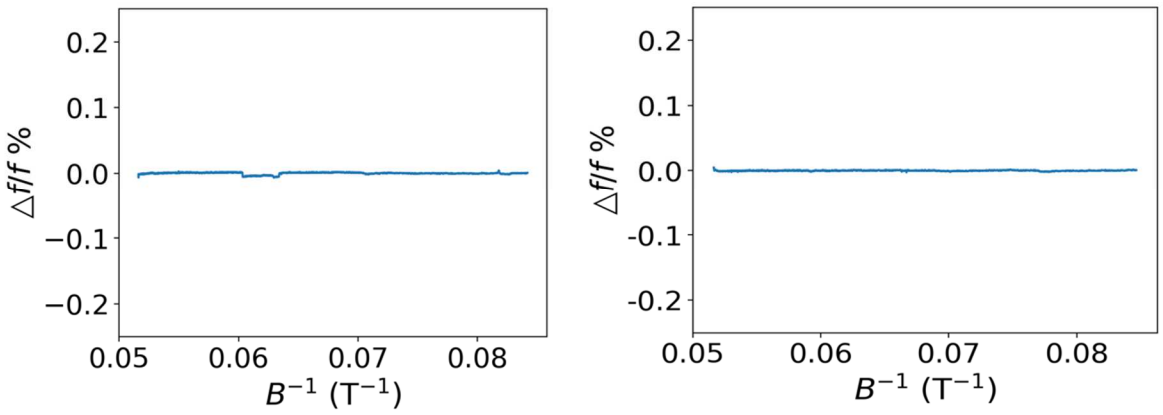

Figure 4-15. SdH oscillations are not observed at atmospheric pressure and 0.4 K at 0° (left plot) and 70° (right plot) after subtracting polynomial background from TDO signal.

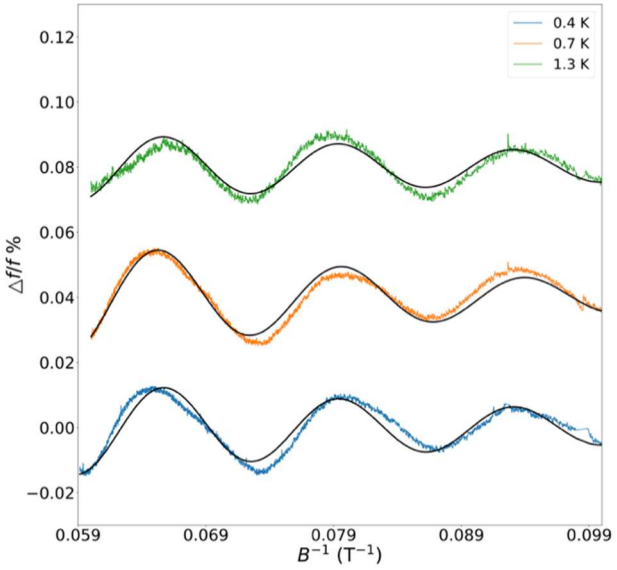

Figure 4-16. SdH oscillations at 0.4 K, 6.4 GPa, and 45° obtained after subtracting polynomial background. Black solid lines are curve fit of the SdH oscillation equation. SdH wave for 0.7 K is shifted by 0.04% and for 1.3 K is shifted by 0.08% for clarity.

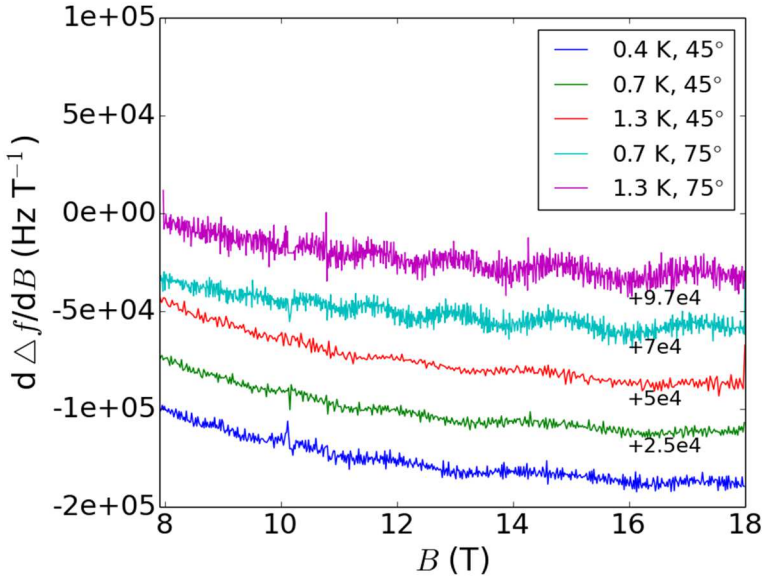

Figure 4-17. SdH oscillations obtained after taking derivative of the TDO signal at 45° and 6.4 GPa.

(a) (b)

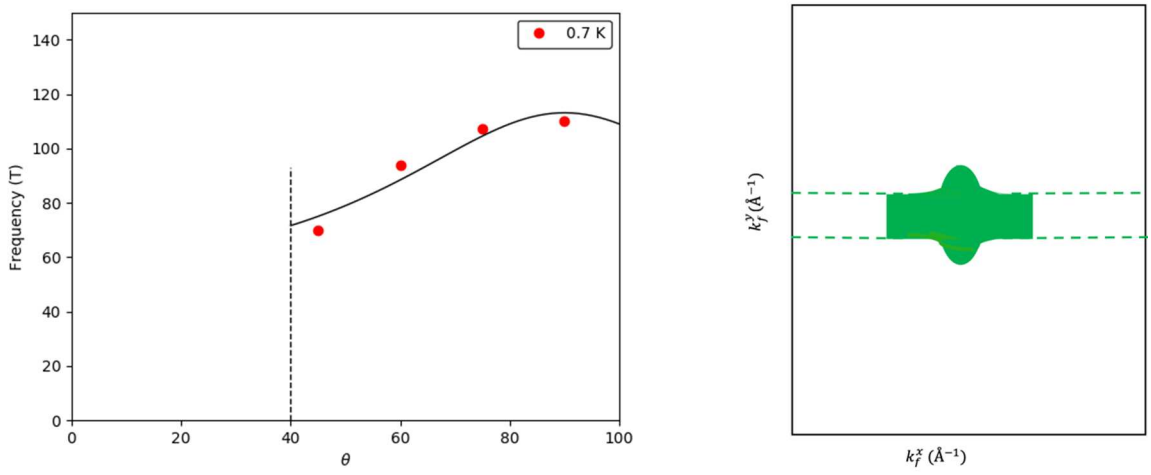

Figure 4-18. (a) Frequency of SdH oscillations at various angles at 0.7 K obtained after polynomial background subtraction. (b) Calculated Fermi surface shape from the quantum oscillation data.

.

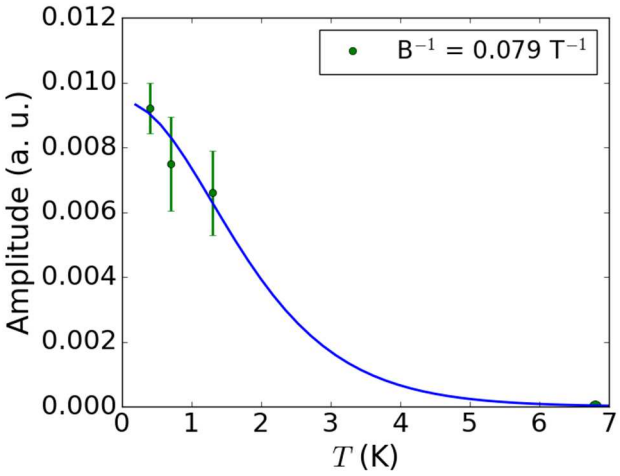

Figure 4-19. Effective mass of an electron obtained after fitting the temperature dependence of amplitude of oscillations at 45˚and fixed value of field inverse. The solid dots denote the experimental values of amplitudes and solid lines are the curve fit.

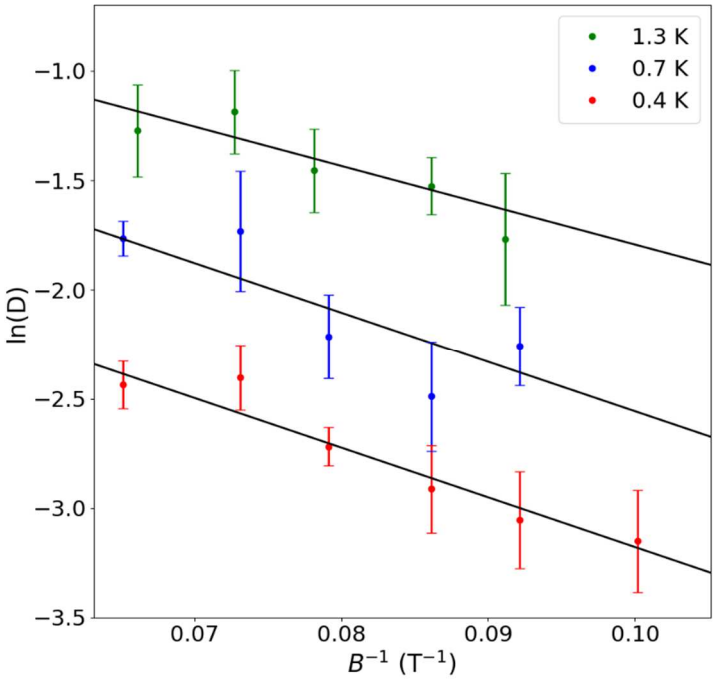

Figure 4-20. Dingle temperature plots at 45° and different temperatures. Solid black lines are the straight-line fits whose slope is equal to $T_D \sim 22$ K.

.

broadening of Landau levels due to electron scattering is equal to the slope of the straight line obtained after fitting it in the plot of $\ln[(\Delta\rho B \sinh(2\pi^2 K_B T/\hbar\omega_c)]$ versus *1/B* at different temperatures as shown in Figure 4-20. The value of $T_D \sim 21 \pm 5$ K obtained is constant irrespective of the temperature and angle. Using T_D, we extract the quantum lifetime of the carriers due to scattering, $\tau = h/4\pi^2 K_B T_D \sim 3.5 \times 10^{-13}$ s. Mobility for our sample at 6.4 GPa, $\mu \sim 0.0678$ Vm^2/s is obtained using $\mu = e\tau/m^*$ indicating a significant decrease from the mobility at atmospheric pressure $\mu = 0.8$ Vm^2/s found by Ming et. al [114].

4.4.4 Conclusions

In summary, we performed the contactless resistivity measurements on Sb_2Se_3 single crystals under high pressure and low temperature. The sample was rotated with respect to the magnetic field. At 6.4 GPa, we observed SdH oscillations periodic in *B*. However, the oscillations were not observed at the atmospheric pressure. The angular dependency of SdH oscillation reveals the presence of quasi-cylindrical Fermi surface whose axis is parallel to the sample's surface at 6.4 GPa. The SdH oscillation equation fit gives Berry phase equal to π which indicates the possible presence of topological states.

4.5 Shubnikov-de Haas Oscillations in $Cu_xBi_2Se_3$

Bi_2Se_3 is a topological insulator that has attracted lot of attention because Cu intercalation can induce superconductivity in $Cu_xBi_2Se_3$ below 3.8 K [91], [103], [115]–[117]. It is proposed theoretically that $Cu_xBi_2Se_3$ is a topological superconductor that has topologically protected gapless surface states and full pairing gap in the bulk. $Cu_xBi_2Se_3$ becomes superconducting at 2.9 K for x = 0.12. The goal of the experiment was to study the effects of quenching on electronic

properties and Fermi surface of $Cu_xBi_2Se_3$ (x = 0.12). To more directly observe properties of the superconducting phase of $Cu_xBi_2Se_3$, investigations of the Fermi surface were carried out via magnetoresistive measurements of Shubnikov-de Haas (SdH) oscillations. In particular, we explored if the origin of superconductivity in the superconducting topological insulator $Cu_xBi_2Se_3$ was from pairing of the topological surface states, or bulk states. (This work was performed in collaboration with Nathaniel Smith and others in Prof. Guptasarma's group. Some of the data presented in this section also appears in Dr. Smith's dissertation. The analysis is mine.)

High temperature quenching of $Cu_xBi_2Se_3$ is needed to induce superconductivity. Somaditya Sen and Nathaniel Smith synthesized sample 1a which became superconducting by quenching at 620□C into cold water and sample 2a which was non-superconducting as it was not quenched. Sample 1a and 2a boules were cleaved into smaller pieces for resistance testing. Four probe resistivity measurements were performed on both samples. The samples were rotated with respect to magnetic field. Small amplitude oscillations periodic in 1/B were identified as SdH oscillations in superconducting sample 1a and non-superconducting sample 2a at different angles and 0.3K temperature as shown in Figure 4-21a. Figure 4-21b shows the magnetoresistance curves of samples 1a and 2a at 0-degree rotation and 0.3K after background subtraction. The amplitude and frequency of SdH oscillations was fitted using the Lifshitz-Kosevich formula (LK) for SdH oscillations.

The SdH oscillation frequency obtained after fitting above equations for the superconducting sample 1a is 378 T while the frequency of non-superconducting sample 2a is 89.9 T at 0-degree rotation and 0.3 K temperature. The oscillation frequency is dependent on angle and independent of temperature. Table 11 and 12 show the SdH oscillation frequency and Berry phase at different angles and temperatures for samples 1a and 2a, respectively. I worked in collaboration

.

with Nathaniel in obtaining SdH oscillation frequencies from the data. The Fermi surface of sample 2a is well fitted to an elliptical Fermi surface. Very few angles yielded oscillations for the superconducting sample leaving the shape of the Fermi surface in the superconducting sample ambiguous. According to Onsager equation, the frequency of this oscillation is proportional to the cross section of the Fermi surface given as $F_s = \hbar A/2\pi e$, where A is the cross-sectional area of the Fermi surface and e is the electron charge. Calculating the Fermi energies of the surfaces using the technique by Fang et al. yields E_F = 626 meV for Sample 1a and 175 meV for Sample 2a, respectively. The ARPES data of Analytis *et.al.* show that the distance from the Dirac point to the bottom of the conduction band in Bi_2Se_3 is ~200 meV [104]. This indicates the non-superconducting samples lie near the bottom of the bulk conduction bands, while the Fermi level of the superconducting sample is well into the bulk conduction bands. If bulk states are needed for superconductivity, this suggests oscillations in superconducting samples will have a frequency f > 90.7 T. Indeed, most superconducting samples in literature have an SdH or de-Haas van Alphen (dHvA) frequency f > 300T, while non-quenched, non-superconducting samples have a much lower frequency. This indicates the Fermi level must be well into the bulk states for superconductivity to appear, suggestive of bulk electrons leading to superconductivity rather than topological ones. The superconducting sample 1a had a larger Fermi surface than non-superconducting sample 2a according to Onsager equation. A combination of Fermi energy and Fermi area calculations indicate that entering the bulk band states in $Cu_xBi_2Se_3$ is crucial to induce superconductivity.

.

Temperature (K)	Angle	Frequency of SdH oscillations (T)
0.3	45	378
0.3	60	380
0.3	75	383

Table 11. SdH oscillation frequency and Berry phase at various angles and 0.3K for Sample 1a

Temperature (K)	Angle (Degrees)	Frequency of SdH Oscillations (T)
10	0	96.25
5.0	0	96.30
1.6	0	96.06
0.3	0	96.28
0.3	-21	94.97
0.3	-6	92.00
0.3	9	89.85
0.3	24	97.00
0.3	39	105.08
0.3	54	123.66
0.3	69	144.38
0.3	79	153.20

Table 12. SdH oscillation frequency and Berry phase at various angles and temperatures for Sample 2a.

(a)

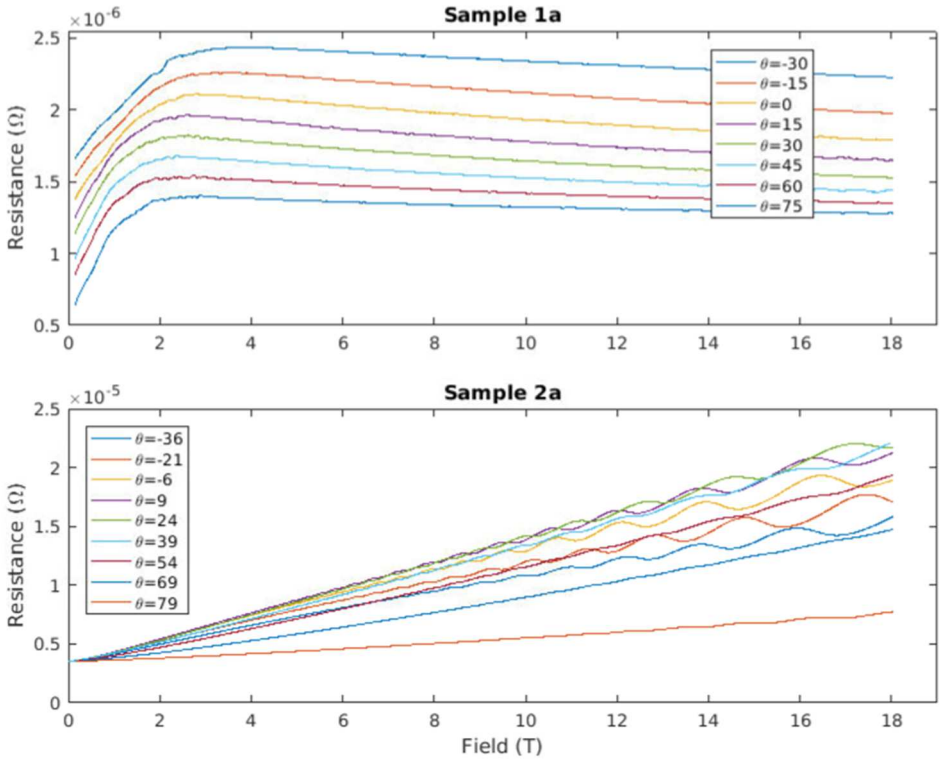

(b)

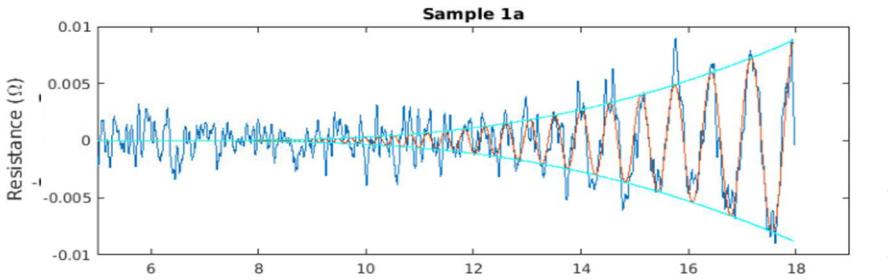

Figure 4-21. (a) Angle dependent resistance measurements at different angles and 0.3 K. (b) SdH oscillations obtained after subtracting background from the data at 0.3 K and 0°. Red curve the SdH oscillation equation fit while blue curve is data. Adapted from reference [89].

.

Chapter 5. Future Work

5.1 Sodium-ion Batteries

Sodium-ion batteries are potential candidates to replace Lithium ion batteries. This dissertation presents a study of the effect of substitution of Jahn-Teller active Fe with Ni and Co in P2-$Na_{0.67}[Mn_{0.5}Fe_{0.5}]O_2$. P2-$Na_{0.67}[Mn_{0.5}Fe_{0.5}]O_2$ is a promising candidate for positive electrode in Na-ion batteries. However, this material suffers from structural transitions at high and low voltages. Substitution of Fe with Ni and Co in $Na_{0.67}[Mn_{0.5}Fe_{0.5}]O_2$ alleviates these structural transitions in $Na_{0.67}Mn_{0.625}Fe_{0.25}Ni_{0.125}O_2$ (NMFNO) and $Na_{0.67}Mn_{0.625}Fe_{0.25}Co_{0.125}O_2$ (NMFCO). We did not observe any structural transition in NMFNO and NMFCO when they are charged to 4.3 V. We observe a mixture of two $P6_3/mmc$ phases when both NMFNO and NMFCO are discharged to 1.5 V. The total impedance of NMFNO and NMFCO after 200 cycles is less than that of NMFO. The initial discharge capacity of NMFNO and NMFCO is greater than NMFO. We observe crack formation on the surface of NMFNO and NMFCO which limits their cyclability. Given the stabilizing effect of Ni and Co in NMFO, further work to improve morphological issues, such as formation of cracks, could make NMFNO and NMFCO a highly promising cathode material with high-capacity and good cycling stability in sodium ion batteries. This may involve using different binder while synthesizing cathodes and changing concentrations of components in cathode slurry. More research on the mechanism of formation of SEI layer and how it changes with cycling may help in improve the understanding of impedance of cathodes during cycling and degradation of cyclability.

.

5.2 Topological Insulators

SnTe is a topological crystalline insulator with rocksalt crystal structure. Recently, other materials such as $Pb_{1-x}Sn_xTe$ and $Pb_{1-x}Sn_xSe$ are also found to become topological crystalline insulators with varying concentrations of Sn in them. The doping and tuning possibilities in $Pb_{1-x}Sn_xSe$ and $Pb_{1-x}Sn_xSe$ opens the door for future research to explore materials with same crystal structure. $Pb_{1-x}Sn_xTe$ system when doped with indium becomes superconducting. In future experiments, superconducting states observed in indium doped $Pb_{1-x}Sn_xTe$ will be interesting to explore. If the superconductivity arises in these materials due to surface states, it will be interesting to explore these superconducting surface states as they can be different from the ones that are observed in traditional topological superconductors.

Sb_2Se_3 becomes topological insulator above 2 GPa pressure. The tuning of energy gap with pressure makes Sb_2Se_3 go through topological transition and become a topological insulator. Application of pressure to tune energy gap may help in transforming other normal insulating materials to a topological insulator. The topological surface bands on Sb_2Se_3 has not been experimentally observed directly me technique such as ARPES. Future experimental research work needs to be performed to design experiment such that ARPES can be performed under pressure to directly observe these surface state bands.

.

BIBLIOGRAPHY

[1] C. Kittel, *Introduction to Solid State Physics*. 2010.

[2] L. Esaki, "New Phenomenon in Narrow Germanium p-n Junctions," *Phys. Rev. JOURNALS Arch.*, vol. 109, pp. 0–1, 1958.

[3] C. T. Van Degrift, "Tunnel diode oscillator for 0.001 ppm measurements at low temperatures," *Rev. Sci. Instrum.*, vol. 46, 1975.

[4] L. Drigo, F. Durantel, A. Audouard, and G. Ballon, "Tunnel diode oscillator-based measurement of quantum oscillations amplitude in pulsed high magnetic fields: a quantitative field-dependent study," *Eur. Phys. J. Appl. Phys.*, vol. 52, 2010.

[5] E. Ohmichi, E. Komatsu, and T. Osada, "Application of a tunnel diode oscillator to noncontact resistivity measurement in pulsed magnetic fields," *Rev. Sci. Instrum.*, vol. 75, 2004.

[6] H. Srikanth, J. Wiggins, and H. Rees, "Radio-frequency impedance measurements using a tunnel-diode oscillator technique," *Rev. Sci. Instrum.*, vol. 70, 1999.

[7] Y. Song, *Novel Pressure - Induced Structural Transformations of Inorganic Nanowires*. 2011.

[8] A. D. Chijioke, W. J. Nellis, A. Soldatov, and I. F. Silvera, "The ruby pressure standard to 150 GPa," *J. Appl. Phys.*, vol. 98, 2005.

[9] J. G. Florian, J. B. Habedank, R. Gilles, G. Reinhart, D. Schreiner, and T. Neuwirth, "Introduction to Electrochemical Impedance Spectroscopy as a Measurement Method for the Wetting Degree of Lithium-Ion Cells," *J. Electrochem. Soc.*, vol. 165, 2018.

[10] C. Liu, Z. G. Neale, and G. Cao, "Understanding electrochemical potentials of cathode

materials in rechargeable batteries," *Mater. Today*, vol. 19, 2016.

[11] B. J. Landi, M. J. Ganter, C. D. Cress, R. A. DiLeo, and R. P. Raffaelle, "Carbon nanotubes for lithium ion batteries," *Energy Environ. Sci.*, vol. 2, 2009.

[12] N. Yabuuchi, K. Kubota, M. Dahbi, and S. Komaba, "Research development on sodium-ion batteries," *Chem. Rev.*, vol. 114, p. 11636−11682, 2014.

[13] M. H. Han, E. Gonzalo, G. Singh, and T. Rojo, "A comprehensive review of sodium layered oxides: Powerful cathodes for Na-ion batteries," *Energy Environ. Sci.*, vol. 8, 2015.

[14] B. L. Ellis and L. F. Nazar, "Sodium and sodium-ion energy storage batteries," *Curr. Opin. Solid State Mater. Sci.*, vol. 16, pp. 168–177, 2012.

[15] S. W. Kim, D. H. Seo, X. Ma, G. Ceder, and K. Kang, "Electrode materials for rechargeable sodium-ion batteries: Potential alternatives to current lithium-ion batteries," *Adv. Energy Mater.*, vol. 2, 2012.

[16] N. Yabuuchi and S. Komaba, "Recent research progress on iron- and manganese-based positive electrode materials for rechargeable sodium batteries," *Sci. Technol. Adv. Mater.*, vol. 15, 2014.

[17] S. M., W. R., C. T., and C. P. Zavalij, "The intercalation and hydrothermal chemistry of solid electrodes," *Solid State Ionics*, vol. 94, 1997.

[18] K. Mizushima, P. C. Jones, P. J. Wiseman, and J. B. Goodenough, "Li_xCoO_2 ($0 < x < 1$): A new cathode material for batteries of high energy density," *Solid State Ionics*, vol. 3–4, 1981.

[19] T. Yamahira, H. Kato, and M. Anzai, "United States Patent 5053297," 1991.

[20] R. Yazami and P. Touzain, "A reversible graphite-lithium negative electrode for electrochemical generators," *J. Power Sources*, vol. 9, 1983.

.

[21] S. Basu, C. Zeller, P. J. Flanders, C. D. Fuerst, W. D. Johnson, and J. E. Fischer, "Synthesis and properties of lithium-graphite intercalation compounds," *Mater. Sci. Eng.*, vol. 38, 1979.

[22] M. S. Islam and C. A. J. Fisher, "Lithium and sodium battery cathode materials: computational insights into voltage, diffusion and nanostructural properties," *Chem. Soc. Rev.*, vol. 43, 2014.

[23] P. H. C. Delmas, C. Fouassier, "Structural Classification and properties of the layered oxides," *Phys. 99B*, 1980.

[24] R. Berthelot, D. Carlier, and C. Delmas, "Electrochemical investigation of the P2-Na_xCoO_2 phase diagram," *Nat. Mater.*, vol. 10, 2011.

[25] K. Kubota, N. Yabuuchi, H. Yoshida, M. Dahbi, and S. Komaba, "Layered oxides as positive electrode materials for Na-ion batteries," *MRS Bull.*, vol. 39, pp. 416–422, 2014.

[26] T. Yasuo, K. Nakahara, M. Nishijima, N. KiImanishi, O. Yamamoto, and M. Takano, "Sodium deintercalation from sodium iron oxide," *Mater. Res. Bull.*, vol. 29, 1994.

[27] N. Yabuuchi *et al.*, "P2-type $Na_x[Fe_{1/2}Mn_{1/2}]O_2$ made from earth-abundant elements for rechargeable Na batteries," *Nat. Mater.*, vol. 11, 2012.

[28] A. Caballero, L. Herna, J. Morales, L. Sanchez, J. S. Pen, and M. A. G. Aranda, "Synthesis and characterization of high-temperature hexagonal P2-$Na_{0.6}MnO_2$ and its electrochemical behaviour as cathode in sodium cells," *J. Mater. Chem.*, vol. 12, 2002.

[29] X. Li, Y. Wang, D. Wu, L. Liu, S. H. Bo, and G. Ceder, "Jahn-Teller assisted Na diffusion for high performance Na ion batteries," *Chem. Mater.*, vol. 28, 2016.

[30] X. Li, D. Wu, Y. N. Zhou, L. Liu, X. Q. Yang, and G. Ceder, "O3-type $Na(Mn_{0.25}Fe_{0.25}Co_{0.25}Ni_{0.25})O_2$: A quaternary layered cathode compound for rechargeable

Na ion batteries," *Electrochem. commun.*, vol. 49, 2014.

[31] T. Chaudhary *et al.*, "JAHN-TELLER DISTORTIONS : A NEW STRATEGY IN QUANTUM MECHANICS," *J. Drug Discov. Ther.*, vol. 3, 2015.

[32] B. M. De Boisse, D. Carlier, M. Guignard, L. Bourgeois, and C. Delmas, "P2-$Na_xMn_{1/2}Fe_{1/2}O_2$ Phase Used as Positive Electrode in Na Batteries: Structural Changes Induced by the Electrochemical (De)intercalation Process Benoit," *Inorg. Chem.*, vol. 54, 2014.

[33] N. Bucher *et al.*, "P2-$Na_xCo_yMn_{1-y}O_2$ (y = 0, 0.1) as Cathode Materials in Sodium-Ion Batteries - Effects of Doping and Morphology to Enhance Cycling Stability," *Chem. Mater.*, vol. 28, 2016.

[34] Z. G. Wei Kong Pang, Sujith Kalluri, Vanessa K. Peterson, Neeraj Sharma, Justin Kimpton, Bernt Johannessen, Hua Kun Liu, Shi Xue Dou, "Interplay between Electrochemistry and Phase Evolution of the P2- type $Na_x(Fe_{1/2}Mn_{1/2})O_2$ Cathode for Use in Sodium-Ion Batteries," *Chem. Mater.*, vol. 27, 2015.

[35] E. Talaie, V. Duffort, H. L. Smith, B. Fultz, and L. F. Nazar, "Structure of the high voltage phase of layered P2-$Na_{2/3-z}[Mn_{1/2}Fe_{1/2}]O_2$ and the positive effect of Ni substitution on its stability," *Energy Environ. Sci.*, vol. 8, 2015.

[36] D. Yuan *et al.*, "P2-type $Na_{0.67}Mn_{0.65}Fe_{0.2}Ni_{0.15}O_2$ Cathode Material with High-capacity for Sodium-ion Battery," *Electrochim. Acta*, vol. 116, 2014.

[37] D. Carlier *et al.*, "The P2-$Na_{(2/3)}Co_{(2/3)}Mn_{(1/3)}O_2$ phase: structure, physical properties and electrochemical behavior as positive electrode in sodium battery.," *Dalt. Trans.*, vol. 40, 2011.

[38] P. Adelhelm, P. Hartmann, C. L. Bender, M. Busche, C. Eufinger, and J. Janek, "From

.

lithium to sodium : cell chemistry of room temperature sodium – air and sodium – sulfur batteries," *Beilstein J. Nanotechnol.*, vol. 6, 2015.

[39] Y. S. Jang-Yeon Hwang, Seung-Taek Myung, "Sodium-ion batteries: present and future," *Chem. Soc. Rev.*, vol. 46, pp. 3529–3614, 2017.

[40] V. Agubra and J. Fergus, "Lithium Ion Battery Anode Aging Mechanisms," *Materials (Basel).*, vol. 6, 2013.

[41] C. Choe, W. Jung, and J. Byeon, "Damage Evaluation in Lithium Cobalt Oxide/Carbon Electrodes of Secondary Battery by Acoustic Emission Monitoring," *Mater. Trans.*, vol. 56, 2015.

[42] S. Tan, Z. Zhang, Y. Li, Y. Li, J. Zheng, and Z. Zhou, "Tris (hexafluoro-iso-propyl) phosphate as an SEI-Forming Additive on Improving the Electrochemical Performance of the $Li[Li_{0.2}Mn_{0.56}Ni_{0.16}Co_{0.08}]O_2$ Cathode Material," *J. Electrochem. Soc.*, vol. 160, 2013.

[43] A. Wang, S. Kadam, H. Li, S. Shi, and Y. Qi, "Review on modeling of the anode solid electrolyte interphase (SEI) for lithium-ion batteries," *npj Comput. Mater.*, vol. 4, 2018.

[44] C. Fouassier, G. Matejka, J.-M. Reau, and P. Hagenmuller, "Sur de nouveaux bronzes oxygénés de formule $Na_\chi CoO_2$ (χ1). Le système cobalt-oxygène-sodium," *J. Solid State Chem.*, vol. 6, 1973.

[45] Y. S. Meng, Y. Hinuma, and G. Ceder, "An investigation of the sodium patterning in Na_xCoO_2 (0.5 <=x<=1) by density functional theory methods," *J. Chem. Phys.*, vol. 128, 2008.

[46] P. Wang, Y. You, Y. Yin, and Y. Guo, "Layered Oxide Cathodes for Sodium-Ion Batteries : Phase Transition, Air Stability, and Performance," *Adv. Energy Mater.*, vol. 8, 2018.

[47] N. Bucher, S. Hartung, I. Gocheva, Y. L. Cheah, M. Srinivasan, and H. E. Hoster,

.

"Combustion-synthesized sodium manganese (cobalt) oxides as cathodes for sodium ion batteries," *J. Solid State Electrochem.*, vol. 17, 2013.

[48] U. Öpik and M. H. L. Pryce, "Studies of the Jahn-Teller effect. I. A survey of the static problem," *Proc. R. Soc. London*, vol. 238, 1957.

[49] U. Garg, W. Rexhausen, N. Smith, J. Harris, D. Qu, and P. Guptasarma, "Crystal structure stabilization, electrochemical properties, and morphology of $Na_{0.67}Mn_{0.625}Fe_{0.25}Ni_{0.125}O_2$ for Na-ion battery cathodes," *J. Power Sources*, vol. 431, 2019.

[50] L. Liu *et al.*, "High-Performance P2-Type $Na_{2/3}(Mn_{1/2}Fe_{1/4}Co_{1/4})O_2$ Cathode Material with Superior Rate Capability for Na-Ion Batteries," *Adv. Energy Mater.*, vol. 5, 2015.

[51] N. Sharma *et al.*, "Rate Dependent Performance Related to Crystal Structure Evolution of $Na_{0.67}Mn_{0.8}Mg_{0.2}O_2$ in a Sodium-Ion Battery," *Chem. Mater.*, vol. 27, 2015.

[52] M. Winter and R. J. Brodd, "What Are Batteries , Fuel Cells , and Supercapacitors?," *Chem. Rev.*, vol. 104, 2004.

[53] C. Parsons, W. Rexhausen, U. Garg, D. Qu, and P. Guptasarma, "Equivalent Circuit models and State of Health in Na-ion Batteries," pp. 3–28, 2020.

[54] S. Han, B. Qiu, Z. Wei, Y. Xia, and Z. Liu, "Surface structural conversion and electrochemical enhancement by heat treatment of chemical pre-delithiation processed lithium-rich layered cathode material," *J. Power Sources*, vol. 268, 2014.

[55] Z. Liu, R. Tian, M. Mushtaq, W. Guo, M. Yao, and J. Feng, "Tailoring high voltage cathode for sodium ion batteries," *J. Alloys Compd.*, vol. 791, 2019.

[56] U. Westerhoff, K. Kurbach, F. Lienesch, and M. Kurrat, "Analysis of Lithium-Ion Battery Models Based on Electrochemical Impedance Spectroscopy," *Energy Technol.*, vol. 4, 2016.

.

[57] C. H. Hsu and F. Mansfeld, “Technical Note: Concerning the Conversion of the Constant Phase Element Parameter Y0 into a Capacitance,” *NACE Int.*, vol. 57, 2001.

[58] G. J. Brug, A. L. G. va. den Eeden, M. Sluyters-Rehbach, and J. H. Sluyters, “The analysis of electrode impedances complicated by the presence of a constant phase element,” *J. Electroanal. Chem. Interfacial Electrochem.*, vol. 176, 1984.

[59] M. E. Orazem, P. Shukla, and M. A.Membrino, “Extension of the measurement model approach for deconvolution of underlying distributions for impedance measurements,” *Electrochim. Acta*, vol. 47, 2002.

[60] H. Nara, D. Mukoyama, R. Shimizu, T. Momma, and T. Osaka, “Systematic analysis of interfacial resistance between the cathode layer and the current collector in lithium-ion batteries by electrochemical impedance spectroscopy,” *J. Power Sources*, vol. 409, 2019.

[61] Z. Deng *et al.*, “Electrochemical Impedance Spectroscopy Study of a Lithium / Sulfur Battery : Modeling and Analysis of Capacity Fading Electrochemical Impedance Spectroscopy Study of a Lithium/Sulfur Battery : Modeling and Analysis of Capacity Fading,” *J. Electrochem. Soc.*, vol. 160, 2013.

[62] B.-A. Mei, O. Munteshari, J. Lau, B. Dunn, and L. Pilon, “Physical Interpretations of Nyquist Plots for EDLC Electrodes and Devices,” *J. Phys. Chem.*, vol. 122, 2018.

[63] G. Nagasubramanian, “Two and Three-Electrode Impedance Studies on 18650 Li-ion Cells,” *J. Power Sources*, vol. 87, pp. 226–229, 2000.

[64] M. Z. Hasan and C. L. Kane, “Colloquium: Topological insulators,” *Rev. Mod. Phys.*, vol. 82, 2010.

[65] M. Sato and Y. Ando, “Topological superconductors: a review,” *Reports Prog. Phys.*, vol. 80, 2016.

.

[66] L. Fu and C. L. Kane, "Topological insulators with inversion symmetry," *Phys. Rev. B*, vol. 76, 2007.

[67] X. Qi and S. Zhang, "Topological insulators and superconductors," *Rev. Mod. Phys.*, vol. 83, 2011.

[68] J. E. Moore, "The birth of topological insulators," *Nature*, vol. 464, 2010.

[69] D. Hsieh *et al.*, "Observation of Time-Reversal-Protected Single-Dirac-Cone Topological-Insulator States in Bi_2Te_3 and Sb_2Te_3," *Phys. Rev. Lett.*, vol. 103, 2009.

[70] F. Nakamura *et al.*, "Topological transition in $Bi_{1-x}Sb_x$ studied as a function of Sb doping," *Phys. Rev. B*, vol. 84, 2011.

[71] X. Zhu, M. Stensgaard, and L. Barreto, "Three Dirac points on the (110) surface of the topological insulator $Bi_{1-x}Sb_x$ Three Dirac points on the (110) surface of the topological insulator $Bi_{1-x}Sb_x$," *New J. Phys.*, vol. 15, 2013.

[72] A. Soumyanarayanan and J. E. Hoffman, "Momentum-resolved STM studies of Rashba-split surface states on the topological semimetal Sb," *J. Electron Spectros. Relat. Phenomena*, vol. 201, 2015.

[73] C. L. Kane and E. J. Mele, "Quantum Spin Hall Effect in Graphene," *Phys. Rev. Lett.*, vol. 95, 2005.

[74] M. Sato and Y. Ando, "Topological superconductors : a review Topological superconductors : a review," *Reports Prog. Phys.*, vol. 80, 2017.

[75] B. A. Bernevig, *Topological Insulators and Topological Superconductors*. .

[76] G. P. Mikitik and Y. V Sharlai, "Manifestation of Berry's Phase in Metal Physics," *Phys. Rev. Lett.*, vol. 82, 1999.

[77] L. Fu, "Topological Crystalline Insulators," *Phys. Rev. Lett.*, vol. 106, 2011.

.

[78] Y. Ando and L. Fu, “Topological Crystalline Insulators and Topological Superconductors: From Concepts to Materials,” *Annu. Rev. Condens. Matter Phys.*, vol. 6, pp. 1–27, 2015.

[79] T. H. Hsieh, H. Lin, J. Liu, W. Duan, A. Bansil, and L. Fu, “Topological crystalline insulators in the SnTe material class,” *Nat. Commun.*, vol. 3, 2012.

[80] Y. Tanaka *et al.*, “Experimental realization of a topological crystalline insulator in SnTe,” *Nat. Phys.*, vol. 8, 2012.

[81] P. Dziawa *et al.*, “Topological crystalline insulator states in $Pb_{1-x}Sn_xSe$,” *Nat. Mater.*, vol. 11, 2012.

[82] S. Xu *et al.*, “Observation of a topological crystalline insulator phase and topological phase transition in $Pb_{1-x}Sn_xTe$,” *Nat. Commun.*, vol. 3, 2012.

[83] T. Phuphachong *et al.*, “Dirac Landau Level Spectroscopy in $Pb_{1-x}Sn_xSe$ and $Pb_{1-x}Sn_xTe$ across the Topological Phase Transition : A Review,” *Crystals*, vol. 7, 2017.

[84] B. A. Assaf, T. Phuphachong, V. V Volobuev, A. Inhofer, G. Bauer, and G. Springholz, “Massive and massless Dirac fermions in $Pb_{1-x}Sn_xTe$ topological crystalline insulator probed by magneto-optical absorption,” *Sci. Rep.*, vol. 6, 2016.

[85] Y. Shimura *et al.*, “Related content Shubnikov-de Haas Measurements in N-Type $Pb_{1-x}Sn_x$ Te,” *Jpn. J. Appl. Phys.*, vol. 21, 1982.

[86] C. Yan *et al.*, “Experimental Observation of Dirac-like Surface States and Topological Phase Transition in $Pb_{1-x}Sn_xTe$ (111) Films,” *Phys. Rev. Lett.*, vol. 112, 2014.

[87] B. M. Wojek *et al.*, “Spin-polarized (001) surface states of the topological crystalline insulator $Pb_{0.73}Sn_{0.27}Se$,” *Phys. Rev. B*, vol. 87, 2013.

[88] D. Shoenberg, *Magnetic oscillations in metals*. Cambridge: Cambridge University Press, 1984.

.

[89] N. Smith, “Crystal Growth and Manipulation of Intercalated Chalcogenides as Superconductors and Topological Insulators,” 2018.

[90] D. Kumar and A. Lakhani, “Observation of π Berry phase in quantum oscillations of three-dimensional Fermi surface in topological insulator Bi_2Se_3,” *Phys. Status Solidi - Rapid Res. Lett.*, vol. 9, 2015.

[91] B. J. Lawson, Y. S. Hor, and L. Li, “Quantum oscillations in the topological superconductor candidate $Cu_{0.25}Bi_2Se_3$,” *Phys. Rev. Lett.*, vol. 109, 2012.

[92] B. J. Lawson *et al.*, “Quantum oscillations in $Cu_xBi_2Se_3$ in high magnetic fields,” *Phys. Rev. B*, vol. 90, p. 195141, 2014.

[93] K. Dybko, M. Szot, A. Szczerbakow, and M. U. Gutowska, “Experimental evidence for topological surface states wrapping around a bulk SnTe crystal K,” *Phys. Rev. B - Condens. Matter Mater. Phys.*, vol. 96, 2017.

[94] A. A. Taskin, F. Yang, S. Sasaki, K. Segawa, and Y. Ando, “Topological surface transport in epitaxial SnTe thin films grown on Bi_2Te_3,” *Phys. Rev. B*, vol. 89, 2014.

[95] Y. Tanaka *et al.*, “Two types of Dirac-cone surface states on the (111) surface of the topological crystalline insulator SnTe,” *Phys. Rev. B*, vol. 88, 2013.

[96] J. Wang, J. Liu, Y. Xu, J. Wu, B. Gu, and W. Duan, “Structural stability and topological surface states of the SnTe (111) surface,” *Phys. Rev. B - Condens. Matter Mater. Phys.*, vol. 89, 2014.

[97] R. C. Sharma and Y. A. Chang, “The Sn-Te (Tin-Tellurium) System,” *Bull. Alloy Phase Diagrams*, vol. 7, 1986.

[98] H. Savage, B. Houston, and J. Burke, “Fermi Surface studies in SnTe,” *Phys. Rev. B*, vol. 6, 1972.

.

[99] J. R. Burke, R. S. Allgaier, and B. B. Houston, "Shubnikov-de Hass Effect in SnTe," *Phys. Rev. Lett.*, vol. 14, 1965.

[100] P. P. Kong *et al.*, "Superconductivity of the topological insulator Bi_2Se_3 at high pressure," *J. Phys. Condens. Matter*, vol. 25, 2013.

[101] J. Zhu *et al.*, "Superconductivity in topological insulator Sb_2Te_3 induced by pressure.," *Sci. Rep.*, vol. 3, 2013.

[102] A. Ohmura and K. Fujimaki, "New superconducting phase of Bi_2Te_3 under pressure above 11 GPa New superconducting phase of Bi_2Te_3 under pressure above 11 GPa," *J. Phys. Conf. Ser.*, vol. 215, 2010.

[103] Y. S. Hor *et al.*, "Superconductivity in $Cu_xBi_2Se_3$ and its Implications for Pairing in the Undoped Topological Insulator," *Phys. Rev. Lett.*, vol. 104, 2010.

[104] J. G. Analytis *et al.*, "Bulk Fermi surface coexistence with Dirac surface state in Bi_2Se_3: A comparison of photoemission and Shubnikov-de Haas measurements," *Phys. Rev. B - Condens. Matter Mater. Phys.*, vol. 81, 2010.

[105] A. Bera *et al.*, "Sharp Raman anomalies and broken adiabaticity at a pressure induced transition from band to topological insulator in Sb_2Se_3," *Phys. Rev. Lett.*, vol. 110, 2013.

[106] W. Li, X.-Y. Wei, J.-X. Zhu, C. S. Ting, and Y. Chen, "Pressure-induced topological quantum phase transition in Sb_2Se_3," *Phys. Rev. B*, vol. 89, 2014.

[107] Y. A. Sorb *et al.*, "Pressure-induced electronic topological transition in Sb_2S_3," *J. Phys. Condens. Matter*, vol. 28, 2016.

[108] P. P. Kong *et al.*, "Superconductivity in strong spin orbital coupling compound Sb□Se□.," *Sci. Rep.*, vol. 4, 2014.

[109] J. Anversa, S. Chakraborty, P. Piquini, and R. Ahuja, "topological insulator High pressure

driven superconducting critical temperature tuning in Sb_2Se_3 topological insulator," *Appl. Phys. Lett.*, vol. 108, 2016.

[110] G. Ghosh, "The Sb-Se (Antimony-Selenium) System," *J. Phase Equilibria*, vol. 14, 1993.

[111] R. Vadapoo, S. Krishnan, H. Yilmaz, and C. Marin, "Electronic structure of antimony selenide (Sb_2Se_3) from GW calculations," *Phys. Status Solidi Basic Res.*, vol. 248, 2011.

[112] I. Efthimiopoulos, J. Zhang, M. Kucway, C. Park, R. C. Ewing, and Y. Wang, "Sb_2Se_3 under pressure," *Sci. Rep.*, vol. 3, 2013.

[113] H. Zhang, C.-X. Liu, X.-L. Qi, X. Dai, Z. Fang, and S.-C. Zhang, "Topological insulators in Bi_2Se_3, Bi_2Te_3 and Sb_2Te_3 with a single Dirac cone on the surface," *Nat. Phys.*, vol. 5, 2009.

[114] S. Ming, S. H. Yu, and M. Chou, "Two-carrier transport-induced extremely large magnetoresistance in high mobility Sb_2Se_3," *J. Appl. Phys.*, vol. 121, 2017.

[115] Z. Pan *et al.*, "Electronic Structure of the Topological Insulator Bi_2Se_3 Using Angle-Resolved Photoemission Spectroscopy : Evidence for a Nearly Full Surface Spin Polarization," *Phys. Rev. Lett.*, vol. 106, 2011.

[116] S. I. Vedeneev, D. A. Knyazev, V. A. Prudkoglyad, T. A. Romanova, and A. V. Sadakov, "Quantum oscillations in strong magnetic fields, berry phase, and superconductivity in three-dimensional topological $Bi_{2-x}Cu_xSe_3$ insulators," *J. Exp. Theor. Phys.*, vol. 121, 2015.

[117] S. Sasaki *et al.*, "Topological Superconductivity in $Cu_xBi_2Se_3$," *Phys. Rev. Lett.*, vol. 107, 2011.

CURRICULUM VITAE

Uma Garg

EDUCATION:

2013 - 2020	PhD, Physics, University of Wisconsin-Milwaukee **Dissertation Title:** "Effects of Intercalation and Deintercalation in Layered Materials: From Topological Insulators to Battery Cathodes" (Advisor Name: Professor Prasenjit Guptasarma)
2011	M.Sc. in Physics, University of Delhi, India
2006	B.Sc. in Physics, University of Delhi, India

SAMPLE PREPATION, MEASUREMENT AND ANALYSIS SKILLS:

Surface analysis tools:
Hands-on experience with the following analytical systems in materials analysis:
X-Ray Diffraction (XRD)
Scanning electron microscopy (SEM)
Energy-dispersive X-ray spectroscopy (EDX)
Raman Spectroscopy
Atomic Force Microscope (AFM)
X-Ray Photoelectron Spectroscopy (XPS) Analysis

Measurement skills:
Hands-on experience with the following measurement techniques:

Resistivity (AC and DC) in Quantum Design PPMS
Extensive experience with clean room protocols.

SPECIALIZED COMPUTER SKILLS:

Data acquisition and Data analysis: LabView, Python, C++, Mathematica, Rietveld refinement of X-ray diffraction data: GSAS, CrystalMaker

RESEARCH PUBLICATIONS:

- **Garg** & Chang, A Semi-Analytic Criterion for the Spontaneous Initiation of Carbon Detonations in White Dwarfs, ApJ, 2017

- **Garg et al.**, Improved cyclability and specific energy of the P2-type $Na_{2/3}Mn_{5/8}Fe_{1/4}Ni_{1/8}O_2$ cathode material for sodium batteries, Journal of Power Sources, 2019

POSTER PRESENTATION:

- Das Gupta & **Garg**; Periodic Gravitational and Electromagnetic Radiation from a highly magnetized, spinning White Dwarf star, contributed paper at Gravitational Wave Physics and Astronomy Workshop IUCAA, Pune, India, Dec 2013

- Structural Transitions, Jahn-Teller Distortion, Cyclability and Specific Energy in *P2*-Type Na_xMO_2 (M=Transition Metals) Materials as Candidates for Sodium-Ion Battery Cathode Applications, **Garg** et al., MRS Symposium 2018

RESEARCH EXPERIENCE:

Activities at National Facilities:

- National High Magnetic Field Laboratory (NHMFL) Tallahassee, FL:
  Activities: Magnetoresistance studies of magnetic field dependent Shubnikov-de Haas (SDH) oscillations at Millikelvin Laboratory.

University Laboratories:

5/2016-5/2020: Graduate Researcher, with Prof. P. Guptasarma (Material Research group):
Laboratory work: Phase pure material synthesis, single crystal growth and study of structure, magnetic and electronic properties of topological insulators, Synthesis of battery cathode and anode materials, slurry synthesis, Coin cell fabrication, Battery cycling

7/2015-4/2016: Research Assistant: Prof. Lian Li (condensed matter lab):
Laboratory work: Chemical vapor deposition of thin films, dry etching of substrates using hydrogen, spin coating of thin films on substrates, characterization of thin films using atomic force microscopy

TEACHING EXPERIENCE:

8/2015-12/2015: Teaching Assistant (Dept. of Physics), teaching PHY 214: Laboratory for Physics for Scientists and Engineers (Calculus Based). Helped develop this lab, incorporated PASCO Scientific computerized data acquisition system.

1/2014-5/2014: Teaching Assistant (Dept. of Physics)
Discussion sessions for General Physics II (Non-Calculus Treatment)

2012- 2013: The Pearl Academy, India

.

Taught science and mathematics to 9th and 10th grade student

AWARDS and HONORS:

2018	David Lichtman Research Fellowship
2018-2019	Distinguished Dissertation Fellowship
2018	Physics Foundation Award
2019-2020	Distinguished Dissertation Fellowship Travel Award
2017	Lichtman Prize for the best experimentalist graduate student
2013 -2017	Chancellor's Fellowship Award, UW–Milwaukee
2014	David Lichtman Memorial Award
2014	Research Excellence Award
2014	Summer Research Scholarship, UW–Milwaukee